Multiphysic modeling and numerical simulation of injection pultrusion processes: impregnation flow, heat-transfer and stress-strain analysis

Fausto Tucci

UNIVERSITY OF SALERNO

DEPARTMENT OF INDUSTRIAL ENGINEERING

Ph.D. Course in Industrial Engineering
Curriculum in Mechanical Engineering - XXXII Cycle

Multiphysic modeling and numerical simulation of injection pultrusion processes: impregnation flow, heat-transfer and stress-strain analysis

Supervisor
Prof. Pierpaolo Carlone

Ph.D. student
Fausto Tucci

Scientific Referees
Prof. Alexander Safonov
Prof. Antonello Astarita

Ph.D. Course Coordinator
Prof. Francesco Donsì

Acknowledgments

This thesis represents the final step of my path as a Ph.D. student. This has been a highly enriching period under both the personal and the scientific points of view. In my opinion, the most important concept I have learned is that relations are the key-factor, in science as well as in life. I consider myself very lucky for all the people I had the pleasure to meet and learn from during the last three years and a half.

I want to address my acknowledgments to the Department of Industrial Engineering of the University of Salerno, which founded my research, and to the Ph.D. course council of the Department, coordinated by Professor Francesco Donsì.

The first special thanks go to my supervisor, Professor Pierpaolo Carlone. He started teaching me how to work when he supervised my bachelor thesis, in 2012, and, after so many years, he is still patiently providing me precious support in everyday activities as well as in long time decisions. He has been always available to guide me when I was facing the problems naturally arising during the Ph.D. path.

During these years, I had the unique opportunity to cooperate with Professor Raimondo Pasquino, and I have the huge fortune to still support his didactic activities. I will take his wise words and his behaviors as a model to follow throughout my entire career.

I want to address a thought to Professor Gaetano Salvatore Palazzo. His wide competences and his huge experience have supported me very often during my first year of Ph.D. Moreover, he has the unique skill to bring good mood to any person he meets.

This Ph.D. started after a fruitful period spent at the Department of Mechanical Engineering of the University of Aveiro to develop my M.Sc. thesis under the supervision of Professor Robertt Valente. His approach to science and research will always inspire my behaviors.

I had the chance to spend a fruitful traineeship at the Fraunhofer IGCV institute of Augsburg, in Germany. I want to thank the Doctor Renato Bezerra for his supervision and support.

In the last three months of my Ph.D. studies, I have been hosted by the Center for Design, Manufacturing and Materials of the Skolkovo Institute of Science and Technology of Moscow. This visit has been very precious for my personal growth and I am sure that this cooperation will last for a long time with highly relevant scientific results. I want to thank Professor Iskander

Akhatov and Professor Alexander Safonov for their supervision. I want to acknowledge Professor Safonov, who covers the role of scientific referee for my thesis. I want also to address special thanks to Aleksander Vedernikov, for his precious collaboration and support.

I acknowledge the Doctor Antonello Astarita, who acted as scientific referee for this thesis. He has played a key role in my Ph.D., and his sincere and direct suggestions have been and will be dramatically important for my personal growth. I will always appreciate his cleverness and his approach to research.

I am grateful to the Doctor Sudarshan, for sharing, in the last months, his precious experience and wisdom with me. His cure in the interactions and relations is an invaluable example.

Finally, I want to express my gratitude toward the persons with which I have interacted most actively in these years. The Doctor Felice Rubino, the Engineer Vitantonio Esperto and Hetal Parmar. Together with Professor Carlone, they represent the working team to which I am proud to belong.

List of publications

- Tucci F., Bezerra R., Rubino F., Carlone P., Multiphase flow simulation in injection pultrusion with variable properties, Materials and Manufacturing Processes 35(2), (2020), pp. 152-162; doi:10.1080/10426914.2020.1711928.
- Tucci F., Esperto V., Rubino F., Carlone P., Experimental Measurement of the Resistant Load in Injection Pultrusion Processes, Procedia Manufacturing 47, (2020), pp. 148–153. doi:10.1016/j.promfg.2020.04.157.
- Tucci F., Rubino F., Esperto V., Carlone P., Integrated modeling of injection pultrusion. AIP Conference Proceedings 2113, (2019), article number 060006. doi:10.1063/1.5112601.
- Tucci F., Rubino F., Carlone P., Strain and temperature measurement in pultrusion processes by fiber Bragg grating sensors. AIP Conference Proceedings 1960, (2018), article number 020036. doi:10.1063/1.5034837.
- Tucci F., Rubino F., Paradiso V., Carlone P., Valente R., Modelling and simulation of cure in pultrusion processes. AIP Conference Proceedings 1896, (2017), article number 070003. doi:10.1063/1.5008078.

Table of contents

List of the figures

List of the tables

Abstract

The present thesis focuses on the study and the modeling of the behaviors occurring in injection pultrusion processes to produce fiber reinforced thermoset polymers. The high market appeal of pultruded profiles and the cost-effectiveness of the process led the pultrusion production to a constant growth in the last twenty years. The key factors determining the success of this technique are the continuity nature of the process the flexibility in material choice and the high customizability of the fibrous reinforcing architecture.

The injection pultrusion technique is the evolution of the conventional pultrusion process. The main difference between the two techniques stands in the way to impregnate the fibrous reinforcement with the resin. Indeed, in injection pultrusion, the pressurized resin is forced through the fibers within a closed injection chamber. The main advantage of this technique with respect to the conventional one consists in a better controllable filling of the reinforcement. Moreover, this version of the process remarkably reduces the direct contact between the resin and working environment, benefiting the operators.

Despite the wide spreading of the pultrusion technique, in many cases the set of the operative parameters is defined by trial and error approach, on the base of the experience of the process designer. The main reason of this are the high number of process parameters and the presence of variables not easily definable and controllable, e.g. the degree of cure of the resin system or the exothermal heat released.

The present thesis proposes a modeling approach to predict the main material behaviors in pultrusion. The modeling methodology has been structured in four steps, namely the matrix-reinforcement system characterization, the modeling of the impregnating flow, the modeling of the thermochemical evolution along the pultrusion die and the mechanical modeling of the stress-strain fields and the pulling force. The numerical models are validated by experimental results.

Chapter I
Introduction

I.1 Advanced fiber reinforced polymers

The modern industry evolves at tremendous velocity toward unpredictable directions. The traditional materials unlikely fit all the specific physical and mechanical requirements needed for demanding application. This necessity leads the researchers to explore new evolved materials characterized by enhanced properties. Actually, the idea to combine a continuous phase with several dispersed phases to produce an improved composite material is not a novelty. Human history reports examples of composite materials since the origins of the civilization. For instance, the ancient Egyptians made bricks of straw dispersed in the clay, and the ancient romans developed the cement mortar. Nevertheless, the industrial acceleration of last years required a further effort to develop elements characterized by an extreme degree of customization.

Advanced fiber reinforced polymers (AFRP) are designed to combine low weight with high mechanical properties in one or more desired directions (Hull and Clyne, 1996). They are composed of a polymeric continuum phase, called matrix, in which a structure of long fiber is properly disposed to fulfil the specific needs (Gutowski, 1997). The typical reinforcement architectures, usually employed in composite industry, are rovings, braids and unidirectional or multidirectional fabrics. In many cases, the different kinds of reinforcements are combined to produce high-performing architectures or multilayer elements (Folkes and Hardwick, 1990).

The continuous phase consists in polymeric resin, either thermoset or thermoplastic (Gutowski, 1997). The resin confers to the AFRP the aesthetical aspect and the geometrical features. At the same time, the main task of the resin is to embed the reinforcement and to transmit the external loads to the fibers (Dvorak, 2012). Moreover, the continuous phase protects the reinforcement from aggressive environments or corrosion (Hollaway, 2010).

In some cases, further dispersed ingredients, namely fillers, are mixed in the resin. These additives are used to fulfil various necessities, such as provide enhanced surface properties (Chang and Friedrich, 2010), provide thermal or electrical conductivity (Ahmad et al., 1992) or control the resin reaction (Harsch, Karger-Kocsis and Holst, 2007).

The thermoset AFRP manufacturing is based on three fundamental steps: the reinforcement impregnation, the shaping of the material and the resin curing. Each of these steps is critical for the quality of the final product. Deficiencies in reinforcement impregnation gives place to voids or dry spots; an inadequate shaping of the material generates geometric discrepancies, fiber displacement and weak spots; incompletions in cure reactions determines the weakness of the composite. Whatever the manufacturing technique used, the process parameters calibration is the key factor to achieve the fulfilment of the three aforementioned tasks, minimizing the process costs and/or times.

I.2 Injection pultrusion process

The injection pultrusion process is a manufacturing technique to produce advanced fiber reinforced profiles characterized by constant cross-section (Shaw-Stewart and Sumerak, 2000). This process is an evolution of the conventional pultrusion process. Pultruded profiles are employed in structural application in which high longitudinal stiffness and strength are required along a peculiar direction. Indeed, as a direct consequence of the used manufacturing process, these products exhibit significant anisotropy, due to the disposition and the direction of the fibrous reinforcement (Meyer, 1985).

Fig. I.1 depicts a schematic view of an injection pultrusion manufacturing line.

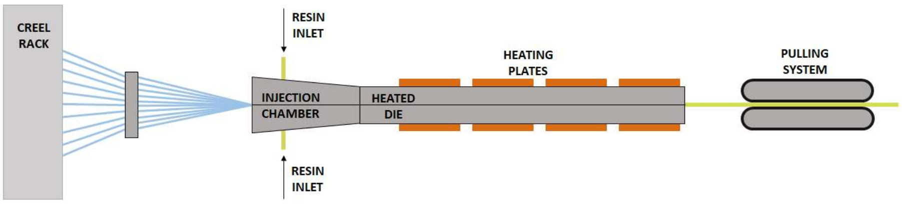

Figure I.1 *Schematic representation of the injection pultrusion line.*

In injection pultrusion lines, the fibrous reinforcement, stored as roving bobbins or fibers fabrics, is driven through a preforming system toward the curing-forming tools. This equipment is composed by a tapered injection chamber and a straight heated die. Impregnation occurs within a closed chamber, in which resin is injected through the fibrous reinforcement by means of nozzles, avoiding any exposure of the liquid polymer with the external working environment (Starr, 2000). The fibers drag the resin through the straight cavity of a steel die. The die is heated by electrical platens, controlled in temperature, to provide the resin with the thermal energy necessary to activate the polymerization reaction. The continuous process is moved by a pulling system located at the end of the line (Baran, 2015).

The choice of the process parameters affects directly the curing cycle of the resin, and, therefore, the quality of the final product (Bank, 2007). Typical defects occurring in pultruded profiles are related to air embedding (Bakis *et al.*, 2002), geometrical distortions (Fairuz *et al.*, 2014), delamination or interlayer cracks (A.A. Safonov, Carlone and Akhatov, 2018). The pulling speed, the imposed temperature and the pulling force are the key factors to achieve a high quality in pultrusion (*GRP bridge across UK M6 motorway*, 2019).

I.3 Market and applications

The particular attention to the pultrusion process is related to the continuous growth in the pultruded profile market (Witten and Mathes, 2019). In particular, the pultruded AFRPs exhibit interesting performances in construction and infrastructure sectors, reinforcement systems for bridges and buildings, window, stair and ladder profiles, as well as antenna systems. In these sectors, other material properties play a key role alongside their lightweight. For example, the fatigue resistance (Ferreira *et al.*, 2001), the transparency to radio waves (European Pultrusion Technology Association, 2019), the resistance in aggressive/corrosive environments (Sakr, El Naggar and Nehdi, 2005), the electrical and thermal insulation (Mahroug, Ashour and Lam, 2014) and the low maintenance required (Zyka and Mohajerani, 2016).

Bridge and bridge decks construction are the largest sectors demanding pultruded profiles. The increasing maintenance costs of traditional bridge decks is an escalating global issue. For instance, steel elements (concrete reinforcement, structural members) is subject to corrosion (*A grasshopper with fibre glass*, 2019), and concrete is susceptible to such degradation mechanisms as sulfate attack, freeze–thaw cycles, and other detrimental processes causing cracking. Therefore, a breakthrough allowing overcoming these disadvantages of conventional materials in bridge construction is needed. In this regard, FRP bridge decks are rapidly emerging as a possible solution in both new construction and rehabilitation projects. FRP bridge decks are mainly made of E-glass fibers and thermosetting resins such as polyester (owing to their low cost) and vinylester (preferable material used in moist environments (*Marley 400 - 800MD - Unilite*, 2019)). This solution has proved its efficiency owing to the advantages of lightweight high strength and improved durability.

Bridges made of composite materials exceed their conventional counterparts for various reasons: light-weight characteristics (*Flexible and durable pool bottom for Danish waterpark*, 2019), (*Engineered for the automotive industry*, 2019), rapid and easy installation or replacement of deteriorated existing structures, noncorrosive properties, longer service life. Moreover, AFRP bridges exhibit enhanced durability in extreme temperature environments (Ghadimi, Russo and Rosano, 2017). This enables dramatic reductions in the bridges' maintenance costs and inspection regularity (CIRIA, 2018).

In the last decades, pultruded AFRPs have been widely used for constructing entire civil engineering structures and their elements (profiles, columns, floor, concrete structure reinforcement, wall systems, modular panels, different types of staging, stairways and walkways, applications related to fencing, railings and personal safety barriers). Pultruded elements are attracting considerable attention due to the possibility of being used for rehabilitation or retrofitting of existing concrete structures or steel beams (*Performance 700 Times Better Than Aluminum*, 2019). The pultruded plates are often used to repair or to strengthen structural beams, columns and slabs or to provide enhanced seismic resistance to the structural building elements. The FRPs are adhesively fixed on the concrete surfaces, oriented in such a way to provide enhanced resistance to the external loads. The blast resistance of concrete slabs can be significantly improved by the application of pultruded reinforcement. In case of beams with web openings, the installation of pultruded supports improves the structural behavior and extends the service life. The defected steel beams retrofitted with pultruded plates demonstrate remarkably better fatigue behavior in terms of crack propagation and number of loading cycles, compared to those repaired by conventional methods.

Pultruded AFRPs find large applications as a substitution for conventional materials in marine structures. In this field, the primary aim is to overcome the corrosion issues due to the harsh marine conditions (harbors, ocean and floating constructions, energy systems, container wharfs, tidal power structure, handrails, gratings). One of the most widespread applications of the pultrusion products in this field is the production of marine piles. Indeed, traditional piles have a shorter life cycle in comparison to composite piles, mainly because of the lower corrosion resistance and the higher susceptibility to the degradation mechanisms initiated by the harsh marine environment (Zhang *et al.*, 2014). FRP based on glass reinforcement is the most common type (mostly owing to their competitive cost (Turvey, 2016)) of composites applied within sheet piling construction. Pultruded AFRPs are widely employed, particularly in shipbuilding (Boyd, Dulieu-Barton and Rumsey, 2006) as well as the naval industry (Tonatto *et al.*, 2016).

In transportations and automotive industries, pultruded profiles with improved impact energy absorption can be successfully used in vehicle designs to ensure the safety of passengers in accidents. Automobile bumpers (Belingardi *et al.*, 2017), bus components (Colombo and Vergani, 2010), truck/trailer elements (Verhaeghe, 2001), bus luggage racks, and subway contact rail support brackets (Fedulov *et al.*, 2016) are just some examples of current pultruded component applications within the transportation industry. Owing to the vast range of various available shapes and cross-section elements, pultrusion has attracted much attention from transportation manufacturers (Park, 2018).

Particularly interesting are the pultruded applications in aeronautic and aerospace (Lau, Said and Yaakob, 2012; Hardesty, 2017). Alongside with the already described properties, the injection pultrusion process allows one to achieve enhanced performance in terms of void presence (Green and Shikhmanter, 1999), which is a key factor in this kind of applications, in which the tolerance of defects and discontinuities is almost null.

It is worth to mention the applications of pultruded elements in renewable energy sectors. Pultrusion is employed to produce long constant-chord blades, wind and marine turbine blade roots (Paulsen *et al.*, 2013, 2014; Baran *et al.*, 2018; Yuksel *et al.*, 2019).

I.4 Motivations and goals

Pultrusion is a highly productive manufacturing technique, due to the continuity and automatability features. At the same time, it exhibit a remarkable flexibility, allowing to pultrude profiles having complex shapes, different reinforcement or matrix materials or various fibrous structures. Nevertheless, as stated earlier, the choice of the process parameters is dramatically influent on the final quality of the product. The reinforcement impregnation, the shaping and the resin cure occurs within a time as shorter as the pulling speed is faster (and therefore the productivity is higher). In many cases, the pursuit of the optimum setting of the process parameters pass through a trial and error strategy, which is related to the unavailability of a complete predictive model of the process.

The aim of the present thesis is the analysis and the modeling of the injection pultrusion to study and predict the performances of the process in different operative conditions. The main objects of the study are the resin flow, the cure and the process related residual stress-strain field. The precise knowledge of the resin properties evolution during cure is fundamental to satisfactory model the material evolution during cure. Fig. 1.2 schematically represents the map of the different models needed to exhaustively describe the injection pultrusion process. The numerous and non-straightforward interconnections among the different physical behavior are partially represented by the connector arcs in fig. I.2.

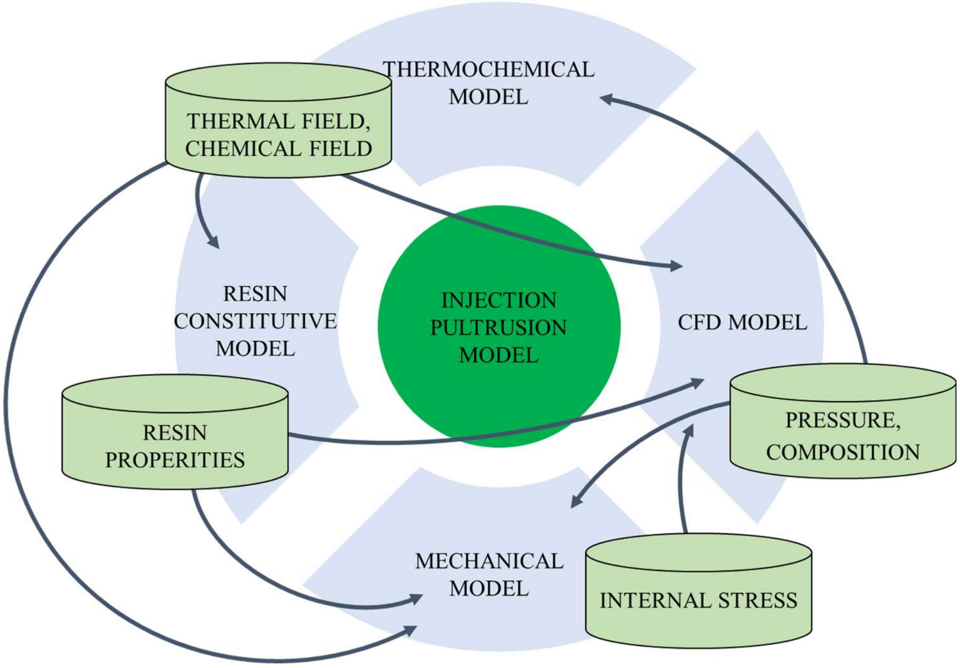

Figure I.2 *Map of the injection pultrusion model.*

The most challenging aspects are related to the physical interconnection between all the different behaviors aforementioned. Indeed, while material travels along the pultrusion line, the chemical, thermal, rheological and mechanical properties evolve affecting, at the same time, internal energy, degree of polymerization, elastic constants and viscosity of the processing material. A multi-physic approach is necessary to account for all the different behaviors occurring at the same time.

Resin constitutive model is based on the analysis of differential scanning calorimetry, dynamo-mechanic analysis, and rheological tests. The outcomes collected by these experimental tests are used to predict the resin properties at different temperature and cure conditions.

The thermo-chemical model solves a set of governing equations consisting in the well-known internal energy equation, including a heat generation term based on the resin reaction rate, coupled with a species equation describing the evolution of the chemical reaction. The internal energy and degree of cure distribution are derived, according to well-defined boundary conditions and loads, solving the aforementioned model using a finite element scheme. The thermochemical submodel is solved implementing and compiling in the Abaqus suite a number of in-house developed subroutines, based on the Fortran language.

The resin flow model predicts the filling of the dry reinforcement within the injection chamber. The model is solved using the finite volume scheme as implemented in Ansys-CFX commercial package, providing the pressure field established in the injection chamber and the volume fractions of fiber, matrix and void.

Finally, the mechanical model, accounting for the outcomes of all the other models, computes the distortions and the transient and residual stresses induced by the process.

Chapter II
Resin characterization

II.1 Constitutive models for advanced composite material

The mechanical behavior of composite materials is significantly different from conventional structural materials. The difference is attributable, first of all, to the inhomogeneity given by the presence of different immiscible components interacting each other. Researchers have developed case specific constitutive models, accounting for combined materials, volume fraction, shape and arrangement of the dispersed phases. In the typical case, the mechanical properties of advanced fiber reinforced materials are mostly determined by the fiber arrangement.

The focus of the present chapter is the estimation of the mechanical properties of the advancing material during pultrusion processes. The mechanical constants of a composite material are computed as functions of the mechanical properties of its components (Bogetti and Gillespie, 1992). It should be considered that, within the same profile, there could be local variations of fiber architecture and volume fraction. Consequently, the cross-section could present zones characterized by different material properties (I Baran, Akkerman and Hattel, 2014). The most common reinforcement structures employed in pultrusion are fibrous rovings (untwisted assemblage of compact bundle of filaments), fabrics (plain patterns of filament yarns) and mat (sheets of long swirled fiber randomly oriented). One of the most widespread model comes from the application of the self-consistent field micromechanics (SCFM) on the composite profiles (Park and Zureick, 2005; Baran, Hattel and Akkerman, 2015). In case of unidirectional roving reinforced polymers, the SCFM approach for the calculation of the longitudinal and transversal elastic moduli and the shear moduli is expressed as follows (Bogetti and Gillespie, 1992):

$$E_L = E_{L,f}V_f + E_{L,m}V_m + \left[\frac{4\left(\nu_m-\nu_{LT,f}^2\right)C_f C_m G_m\left(1-V_f\right)V_f}{\left(C_f+G_m\right)C_m+\left(C_f-C_m\right)G_m V_f}\right], \tag{II.1}$$

$$E_T = \frac{1}{(4C_T)^{-1}+(4G_{LT})^{-1}+\left(\nu_{LT}^2/E_L\right)} \ , \tag{II.2}$$

$$G_{LT} = G_m\left[\frac{\left(G_{LT,f}+G_m\right)+\left(G_{LT,f}-G_m\right)V_f}{\left(G_{LT,f}+G_m\right)-\left(G_{LT,f}-G_m\right)V_f}\right] \ , \tag{II.3}$$

$$G_{TT} = \frac{G_m\left[C_m\left(G_m+G_{TT,f}\right)+2G_{TT,f}G_m+C_m\left(G_{TT,f}+G_m\right)V_f\right]}{C_m\left(G_m+G_{TT,f}\right)+2G_{TT,f}G_m-\left(C_m+2G_m\right)\left(G_{LT,f}-G_m\right)V_f} \ , \tag{II.4}$$

$$\nu_{LT} = \nu_{LT,f}V_f + \nu_m V_m + \left[\frac{\left(\nu_m-\nu_{LT,f}\right)\left(C_m-C_f\right)G_m\left(1-V_f\right)V_f}{\left(C_f+G_m\right)C_m+\left(C_f+C_m\right)G_mV_f}\right] \ , \tag{II.5}$$

$$\nu_{TT} = \frac{2E_Lk_T-E_LE_T-4\nu_{LT}^2C_TE_T}{2E_LC_T} \ . \tag{II.6}$$

In Eqs. (II.1) to (II.6), E, G and ν are the elastic and the shear moduli and the Poisson ratio. The subscripts L and T refer to the longitudinal and the transversal direction respectively, while the subscripts f and m refer to fiber and matrix. The mechanical properties without f or m subscripts refer to the composite material. V_f and V_m are respectively the fiber and the matrix volume fractions. The symbols C_f and C_m are the isotropic plane strain bulk modulus for fiber and resin, while C_T is the plane strain bulk modulus. The plane strain moduli are expressed as follows (Bogetti and Gillespie, 1992):

$$C_f = \frac{E_{L,f}}{2\left(1-\nu_{LT,f}-2\nu_{LT,f}^2\right)} \ , \tag{II.7}$$

$$C_m = \frac{E_m}{2\left(1-\nu_m-2\nu_m^2\right)} \ , \tag{II.8}$$

$$C_m = \frac{\left(C_f+G_m\right)C_m+\left(C_f+C_m\right)G_mV_f}{\left(C_f+G_m\right)-\left(C_f-C_m\right)V_f} \ . \tag{II.9}$$

In the SCFM model described by Eqs. (II.1) to (II.9) the only components considered are the fibers and the polymeric matrix. Therefore, the eventual presence of air embedded in the composite has been neglected. Typically, in pultrusion the presence of air is limited, depending on the process parameters setting (Tucci *et al.*, 2020). It is worth to note that in the present model the resin is considered isotropic, while the fibers are considered transversally isotropic.

When mat sheets are used as reinforcement the mechanical behavior of the composite can be assumed quasi-isotropic, due to the random orientation of the fibers (Bank, 2006). Mat tissues are generally used only in external layers of pultruded profiles. Due to their configuration, mat sheets are characterized by in-plane isotropic properties, in longitudinal and tangential to the external surface directions, and out-of-plane properties, toward the profile core. The SCFM approach evaluates the properties of quasi-isotropic mat reinforced composites as functions of the properties of a fictitious layer reinforced by unidirectional roving (eqs. (II.1) to (II.9)) having the same fiber volume fraction (Akkerman, 2002). The in-plane constants, E_{IP}, G_{IP} and ν_{IP}, are expressed as follows (Tsai and Hahn, 2000):

$$E_{IP} = 2(1+\nu_{IP})G_{IP} \ , \tag{II.10}$$

$$\nu_{IP} = \left[\frac{-4(E_L-\nu_{LT}^2E_T)G_{LT}+E_L(E_L+E_T+6\nu_{LT}E_T)}{-4(E_L-\nu_{LT}^2E_T)G_{LT}+E_L(3E_L+3E_T+2\nu_{LT}E_T)}\right] \ , \tag{II.11}$$

$$G_{IP} = \frac{G_{LT}}{2}+\frac{E_L(E_L+E_T-2\nu_{LT}E_T)}{E_L-2\nu_{LT}^2E_T} \ . \tag{II.12}$$

The out-of-plane properties, namely E_{OP}, G_{OP} and ν_{OP}, are defined using the averaging method (Goetschel and Radford, 1997):

$$E_{OP} = \frac{E_L+(1+2\nu_{LT})E_T}{(1-\nu_{TT}^2)(E_L/E_T)+(1+2\nu_{LT}+2\nu_{LT}\nu_{TT})-\nu_{LT}^2(E_L/E_T)} \ , \tag{II.13}$$

$$\nu_{OP} = \frac{E_{IP}}{E_L}\left[\frac{(\nu_{LT}+\nu_{TT}+\nu_{LT}\nu_{TT})+\nu_{LT}^2(E_T/E_L)}{1+(1+2\nu_{LT})(E_T/E_L)}\right] \ , \tag{II.14}$$

$$G_{OP} = 2\left(\frac{G_{LT}G_{TT}}{G_{LT}+G_{TT}}\right) \ . \tag{II.15}$$

As can be noted by Eqs. (II.1) to (II.9), the constitutive equations of roving and mat reinforced pultruded profiles are expressed as functions of the properties of resin and fibers. The mechanical properties of the reinforced are assumed to be constant during the process. However, the resin system experiences a dramatic variation of its status and properties due to the cure reaction (Bogetti and Gillespie, 1992). Indeed, during the crosslinking reaction, the polymeric chains join each other forming reticular macromolecules. Direct consequences of this are the increase in molecular weight and in polymer mechanical properties.

The curing reaction is activated providing energy to the catalyzed resin. The energy input can be in form of heat (Yousefi, Lafleur and Gauvin, 1997), plasma (Friedrich, 2011; Saboohi *et al.*, 2019), UV radiations (Saenz-Dominguez *et al.*, 2019), or chemical catalysts action (Bochmann, 2010). The complete knowledge of the evolution of the resin properties during cure reaction is fundamental to define the composite constitutive model. In all the manufacturing processes of FRPs, the impregnation phase is constrained by the resin gelation time, which, in turn, is ruled by the curing process. The accurate definition of resin properties evolution during cure is critical in the implementation of the process monitoring strategies and apparatus (Frauendorfer, Wolf and Hergeth, 2010; Marin *et al.*, 2012).

In order to calibrate the composite constitutive law, it is necessary to define the resin properties evolution. The cure hardening instantaneous linear elastic (CHILE) approach describes the evolution of the resin modulus E_m as a function of the temperature and of the degree of cure (eq. (II.16)) (Johnston, Vaziri and Poursartip, 2001):

$$E_m(T,\alpha) = \begin{cases} E_0 \,, & T^* \leq T_{C1} \,; \\ A_e \, exp(B_e \, T^*) \,, & T_{C1} < T^* \leq T_{C2} \,; \\ E_1 + \frac{T^* - T_{C2}}{T_{C3} - T_{C2}} (E_\infty - E_1) \,, & T_{C2} < T^* \leq T_{C3} \,; \\ E_\infty \,, & T_{C3} < T^* . \end{cases} \qquad \text{(II.16)}$$

In Eq. (II.16) E_0, E_1 and E_∞ represent, respectively, the elastic modulus of the liquid resin and of the fully cured resin, A_e and B_e are characteristic parameters, T_{C1}, T_{C2} and T_{C3} are the critical temperatures at the activation and completion of the glass transition and T^* is the difference between the glass transition temperature T_g and the actual temperature (Eq. (II.17)), i.e.:

$$T^* = T_g - T \,. \qquad \text{(II.17)}$$

The glass transition temperature is generally expressed as a linear function of the degree of cure, accounting for the glass transition temperature of the fully uncured resin ${T_g}^0$ and of the variation coefficient of the glass transition temperature α_{Tg} as described by the following relation. Analytically it writes:

$$T_g = {T_g}^0 + \alpha_{Tg} \, \alpha \,. \qquad \text{(II.18)}$$

The scientific literature reports several different techniques employed to characterize the thermoset resin systems, e.g. the differential scanning calorimetry (Sourour and Kamal, 1976), the thermo-gravimetric analysis (Wu *et al.*, 2002), the thermo-mechanical analysis (Olivier, 2006), the dynamo-mechanical analysis (Goertzen and Kessler, 2007), the rheology analysis (Mao *et al.*, 2009) or the dielectric analysis (Hardis *et al.*, 2013).

The present chapter describes the characterization of the polymeric matrices employed in pultrusion experiments, namely an ortophtalic polyester (ESI resin GP med OT- Euroresins ltd.) based system and two epoxy based systems (EC 114- Elan-Tech® and CR141-Sika Biresin®). Differential scanning calorimetry, rheological analysis and dynamo-mechanical analysis are the techniques selected to define the resin behaviors.

II.2 Differential scanning calorimetry tests

II.2.1 Generalities

The differential scanning calorimetry (DSC) is based on the measurement of the heat flow, absorbed or generated, between the analyzed sample and an inert reference element of similar mass and geometry. This inspective technique is based on the exothermal nature of the cure reaction: The DSC equipment provides thermal energy to the resin sample, following a preset temperature law. The provided energy activates the resin polymerization, which produces further heat due to the exothermal reaction. The heat produced is measured by means of a system of thermal sensors and it is correlated to the evolution of the cure reaction (Schick, 2009). The DSC characterization is based on the comparison between the analyzed resin sample and an unreactive reference element. The samples are contained inside a metallic crucible of known mass and material. Typically, the reference consists in an empty crucible. Both the sample and the reference are subject to a thermal cycle within a furnace at controlled temperature and pressure.

The DSC analysis can be performed using two different modalities, and, therefore, two different equipment. The two modes are the heat flow DSC (Drebushchak, 2004) and the power-compensated DSC (Höhne and Schawe, 1993). In the former case, the crucibles containing the sample and the reference are placed in the same furnace. The temperature of the furnace is controlled according to a predefined thermal cycle. The temperature of each crucible is measured by several thermal sensors. The primary collected signal is related to the temperature difference between the sample and the reference. This, in turn, is intimately related to the heat flow between the sample and the environment (Mraw, 1982). In the latter case, the sample and the reference are located in two independent furnaces. The furnace is controlled in temperature in order to force the sample and the reference to follow the same predefined cycle. In this case, the heat flow is evaluated measuring the thermal energy provided by the equipment to each crucible in order to respect the aforementioned condition (Höhne and Schawe, 1993).

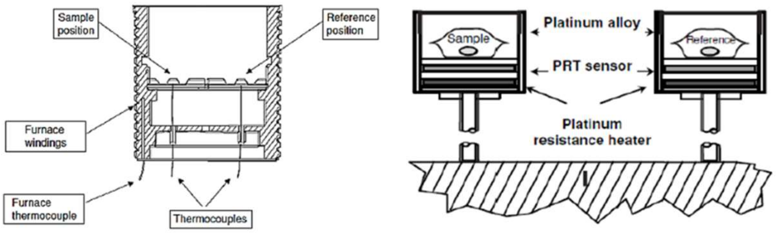

a) b)

Figure II.1 *a) Heat flow differential scanning calorimetry; b) power-compensation differential scanning calorimetry.*

In the DSC analysis of polymeric systems, the thermal effects, namely heat generation and absorption, are evidenced by peaks or valleys in the heat flow curve.

Beyond the cure kinetic, several other properties can be evaluated by DSC inspection, namely heat capacity (Boller, Jin and Wunderlich, 1994), glass transition temperature (Papon *et al.*, 2012), material contamination (Bruni *et al.*, 2011; Zanqui *et al.*, 2015).

In general, the cure evolution is described by the expression of the cure rate. It is defined as the variation of the degree of cure in time. Eq. (II.19) describes the cure rate evolution as the product of three terms (Eq. (II.19)), respectively functions of the temperature, the degree of cure and the pressure (Vyazovkin *et al.*, 2011):

$$\frac{d\alpha}{dt} = k(T) f(\alpha) h(P) \,. \tag{II.19}$$

The pressure dependence is neglected in the most of the cases (Vyazovkin *et al.*, 2011). The term $k(T)$ is typically expressed as an Arrhenius function (Eq. (2.20)), which accounts for a frequency factor A_0 and the activation energy E_a:

$$k(T) = A_0 exp\left(-\frac{E_a}{R\,T}\right) . \tag{II.20}$$

The dependence on the degree of cure can be described by using a wide variety of functions, accordingly to the specific kinetic evolution (Brown, 2004).

The definition of the kinetic parameters is based on the analysis of the heat generation/absorption measured in DSC heat flow experiments. In particular, the heat $H(T)$ generated from the reaction onset instant t_i up to the generic instant t can be computed accounting for the generated heat flow $Q(T)$, as described by Eq. (II.21) (Vyazovkin *et al.*, 2011):

$$H(T) = \int_{t_i}^{t} Q(T)\, dt \,. \tag{II.21}$$

Since cure reaction is measured observing the generated heat, the degree of cure α can be expressed accounting for the heat generated and the total reaction heat H_T:

$$\alpha(T) = \frac{H(T)}{H_T} . \tag{II.22}$$

Therefore, once known the total reaction heat, it is possible to achieve the experimental cure profile by a DSC analysis. The experimental cure rate is computed as the numerical derivative of the degree of cure. The DSC test must be repeated using several different heating rates, since the polymerization reaction depends on the thermal history of the resin (Hardis *et al.*, 2013). Finally, the kinetic parameters are achieved by regression of the experimentally evaluated cure rates.

DSC dynamic tests have been performed to define the cure kinetics of two polymeric matrices, namely the ortophtalic polyester (ESI resin GP med OT, Euroresins ltd.) based system and an epoxy (EC 114, Elan-Tech®) based system.

II.2.1 Experimental tests: DSC analysis of the epoxy based system

The epoxy-based system used in this study was prepared mixing the epoxy resin Elan-Tech EC 114 with the hardener Elan-Tech W 132. The thermal analysis has been carried out using the differential scanning calorimeter Netzsch DSC 204 (Fig. II.2) in heat flow mode.

Figure II.2 *Differential scanning calorimetry Netzsch DSC 204 equipment.*

Mixed resin samples, having mass between 7 and 10 mg, were put in aluminum crucibles. The mass of each crucible was 30 ∓ 0.5 mg. One crucible was filled using a dropper and then mechanically closed. Before each test, the crucible has been weighted before the resin filling and after the mechanical closing, in order to exactly know the mass of the tested resin. An empty crucible was used as reference inert element. The two crucibles were placed within the furnace in their apposite housings. Fig II.3 (a) shows the two housings the DSC furnace, while Fig. II.3 (b) depicts the sample and the reference crucibles placed in the furnace.

a) b)

Figure II.3 *a) housing for crucibles; b) placement of sample and reference crucibles.*

The experiments were performed using temperature ramps of 20, 30, 40 and 50°C/min to heat up the furnace from 20°C to 250°C. Two repetitions per each of the heating rates were performed. The choice of the heating rates is based on the typical thermal variations experienced by the material in pultrusion process. In pultrusion the temperature derivatives can be even twice higher, nevertheless, using ramps faster than 50°C/min would have been detrimental to measuring accuracy (Ismet Baran, Akkerman and Hattel, 2014).

Fig II.4 shows the raw data collected in one representative case of the heat flow DSC experiments performed.

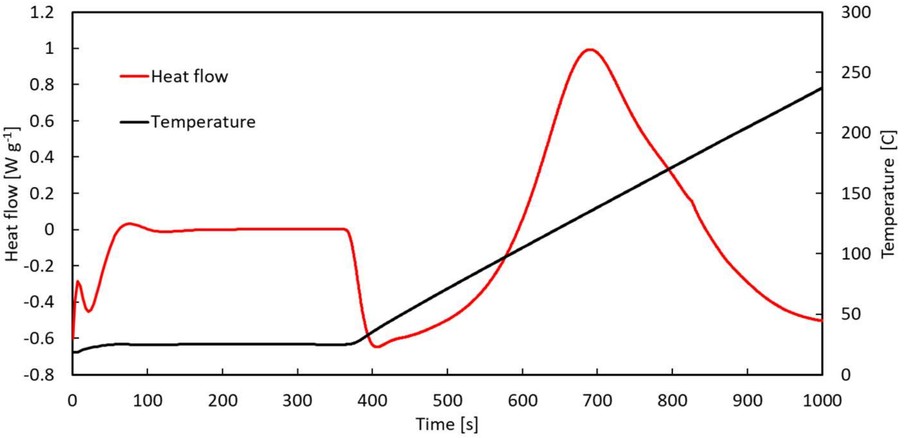

Figure II.4 *Representative heat flow outcomes in DSC analysis.*

During the first 350 s, in order to stabilize the furnace environment, the temperature has been kept at the constant value of 20 °C. Afterward, the heating system started to provide thermal energy to heat up the furnace according to the programmed thermal ramp. The heat flow sharply decreases when the temperature increase starts. In facts, the resin initially absorbs energy pursuing the thermal equilibrium with the furnace environment. At the reaction activation, the heat flow curve evidence a minimum. Starting from the activation, the sample generates a heat flow, which reaches a peak and then decreases. When the negative slope of the heat flow curve approaches to null value, the reaction can be assumed completed. The thermal generation during heating is proportional to the reaction rate. The heat flow profile, from the activation to the end of the reaction is numerically corrected in order to select the generation and eliminate the influence of absorption and thermal inertia of the sample. The numerically treated data are depicted in fig II.5 and fig. II.6 as function of temperature and time.

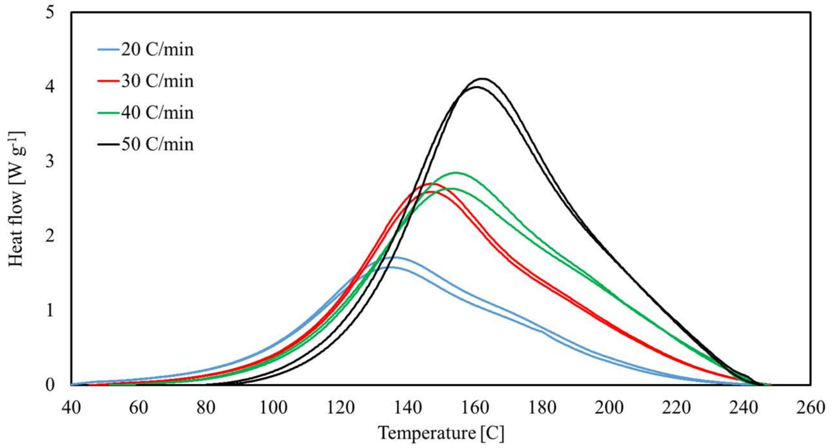

Figure II.5 *Resin sample heat release with respect to the temperature.*

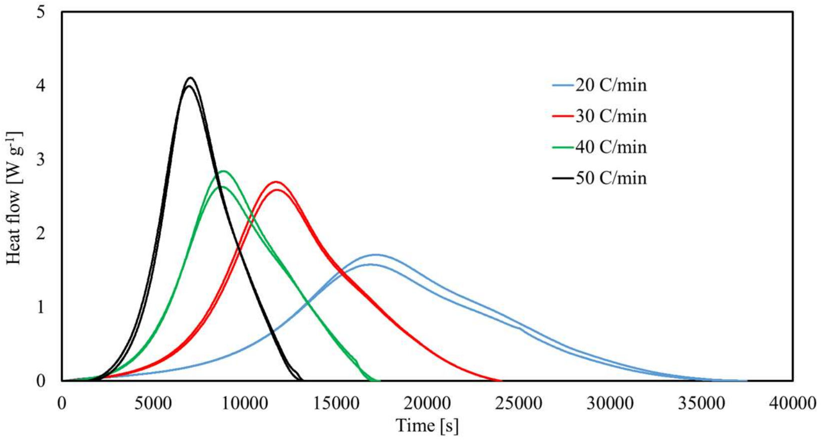

Figure II.6 *Resin sample heat release with respect to the time.*

The reaction rate is proportional to the emitted heat flow, according to Eq. (II.2). In the dynamic DSC tests, the reaction starts with null heat flow. It is worth to note that the reaction is activated at different temperature. In particular, the slowest is the heating rate the lowest is the activation temperature. Indeed, initially the resin absorbs the thermal energy. When the reaction starts, the sample starts to release thermal energy. The plotted data refers only to the generated heat flow. The heat flow peak results higher in faster cases, in agreement with the scientific literature (Hardis *et al.*, 2013). Using heating rates of 20°C/min, at the end of the tests the cure reaction can be considered completed, since the heat flow is stably null, while with higher heating rates the reaction is not complete at the end of the experiment. These discrepancies are related to the thermochemical inertia of the resin sample. Indeed, heating with slower rates, the resin molecules have a longer time to reticulate and complete the reaction. Due to this reason, the total reaction energy can be evaluated integrating the heat flow Q_{20} measured at 20°C/min with respect to the time, as described in Eq. (II.23) (Hardis *et al.*, 2013):

$$H_T = \int_{t_i}^{t_f} Q_{20}\, dt\,. \qquad \text{(II.23)}$$

In Eq. (II.23), t_i and t_f are the activation and the final time. The degree of cure in all the heating rates is computed accounting for this total energy. Fig. II.6 to II.10 show the cure rate and the degree of cure evolutions in all the investigated cases with respect to the temperature and the time.

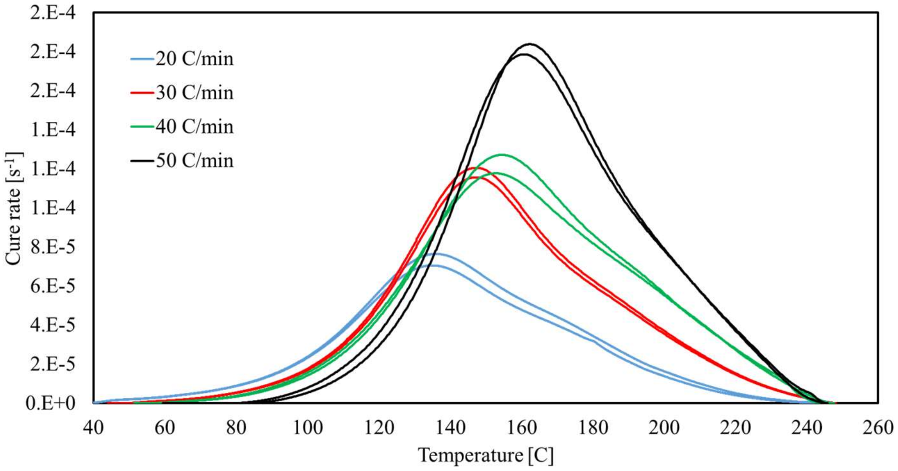

Figure II.7 *Cure rate evolution with respect to the temperature.*

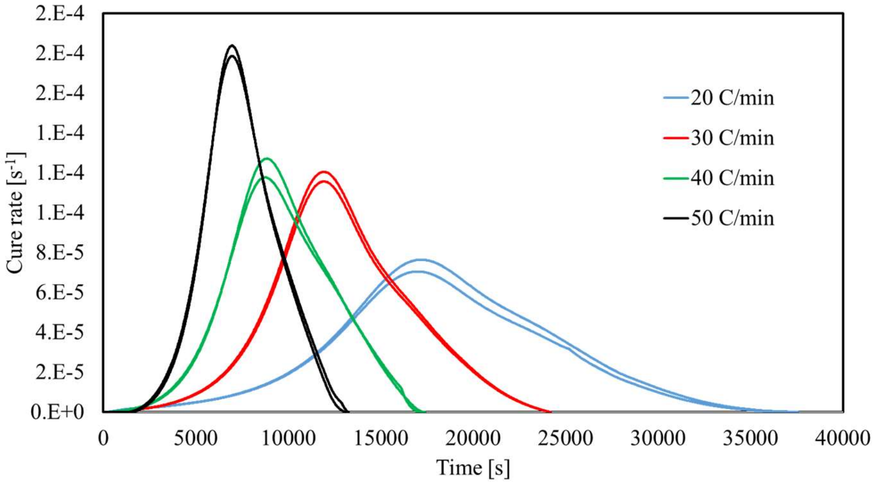

Figure II.8 *Cure rate evolution with respect to the time.*

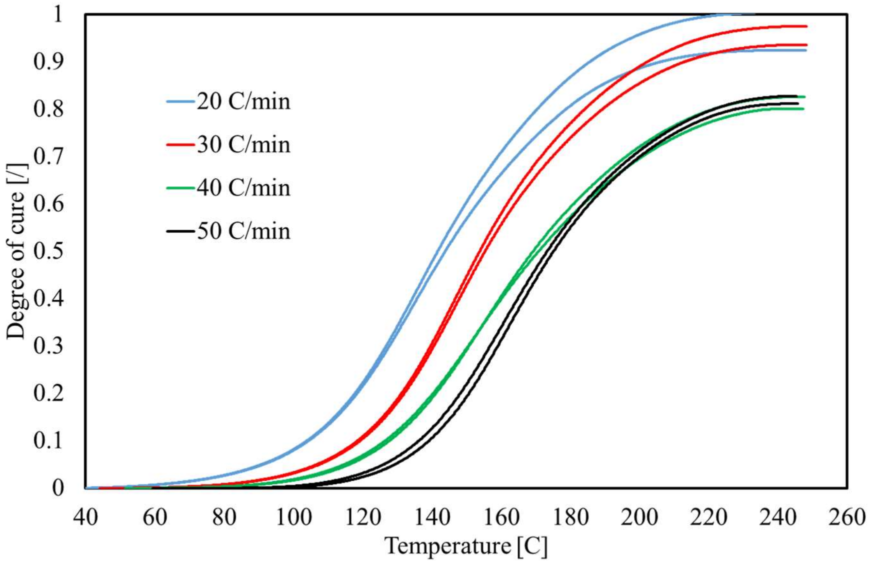

Figure II.9 *Degree of cure evolution with respect to the temperature.*

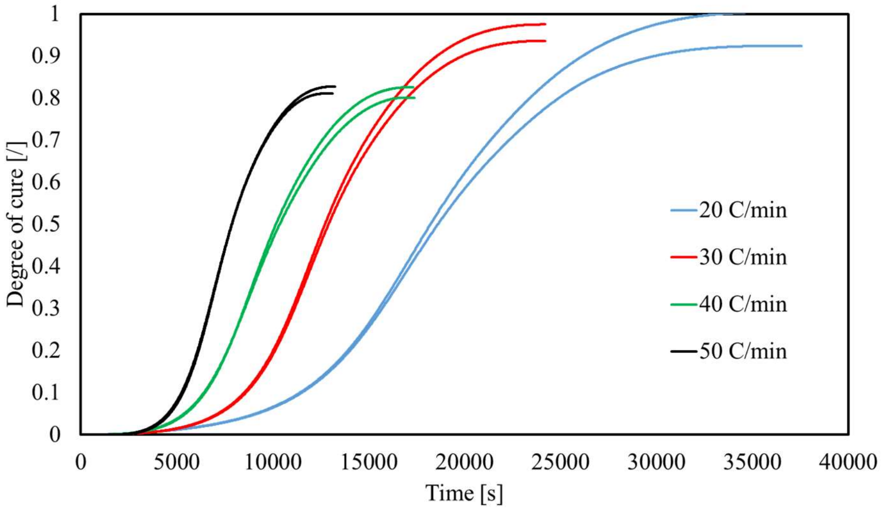

Figure II.10 *Degree of cure evolution with respect to the time.*

In the present study, the collected cure rate profiles were used to evaluate the polymerization kinetic, using an error minimization routine developed in Matlab language. In particular, the autocatalytic Prout-Tompkins model was assumed to describe the kinetic of the reaction (Šesták and Berggren, 1971). The used model writes as follows:

$$R(T,\alpha) = A_0 exp\left(-\frac{E_a}{R_{gas}\,T}\right)\alpha^m(1-\alpha)^n\,. \tag{II.24}$$

In Eq. (II.24) A_0 is the frequency factor, E_a is the activation energy, R_{gas} is the universal gas constant, m and n are the characteristic exponents. The values of the kinetic parameter are reported in tab. II.1.

Table II.1 *Kinetic parameters of the epoxy based system*

Symbol	Value	Unit
A_0	4.17e+5	[s^{-1}]
E_a	5.90e+5	[kJ mol^{-1}]
m	0.15	[/]
n	1.65	[/]

II.2.2 Experimental tests: DSC analysis of the orthophtalic polyester based system

The orthophtalic polyester based system was prepared mixing the ESI resin GP with Trigonox C-C75, Trigonx 29-C50 and Perkadox 60 (Akzo Nobel).

The thermal analysis has been performed using the differential scanning calorimeter Mettler Toledo 822 (Fig. II.11).

Figure II.11 *Differential Scanning Calorimeter Mettler Toledo.*

A dynamic investigation was conducted in heat flow mode. The temperature ramps start from room temperature to 200°C, with heating rates of 10, 15 and 20°C/min. The cure rate and the degree of cure evolutions with respect to the temperature are depicted in Figs. II.12 and II.13.

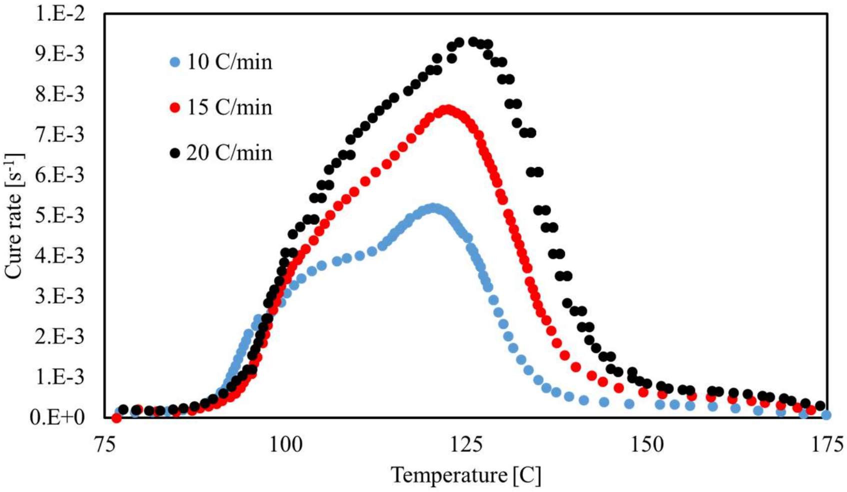

Figure II.12 *Polyester system cure rate evolution with respect to the temperature.*

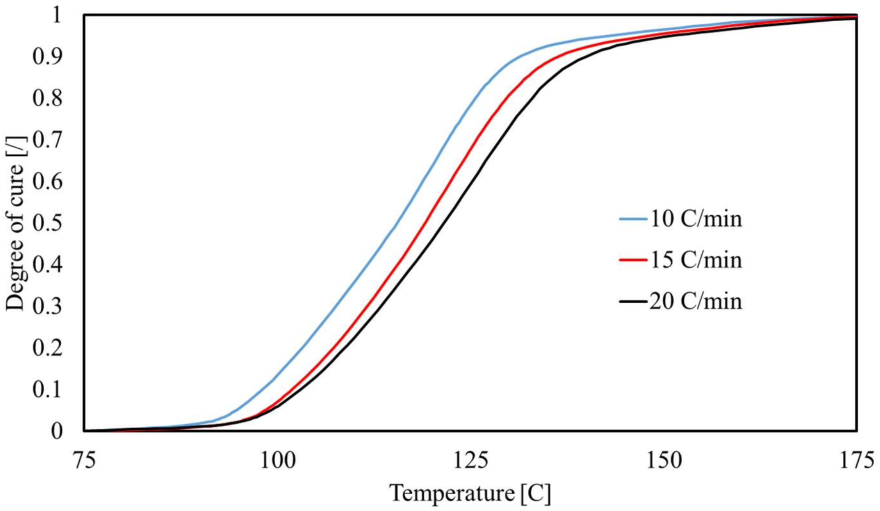

Figure II.13 *Polyester system degree of cure evolution with respect to the temperature.*

The reaction kinetic has been analyzed following the same procedure previously described. The cure rate evolution is well described by the expression reported in eq. (II.25), whose parameter are reported in tab. II.2.

$$R(T,\alpha) = A_0 exp\left(-\frac{E_a}{R_{gas}\,T}\right)\alpha^m(1-\alpha)^n \,. \qquad \text{(II.25)}$$

Table II.2 *Kinetic parameters of the ortophtalic polyester based system*

Symbol	Value	Unit
A_0	7.59e+9	[s^{-1}]
E_a	8.27e+5	[kJ mol^{-1}]
m	0.63	[/]
n	1.85	[/]

II.3 Rheological tests

The rheological experiments on thermoset resin have the purpose to evaluate the resin viscosity evolution during cure (Shanku, Vaughan and Roux, 1997). In the present thesis, rheology tests have been performed to characterize two different epoxy based resin systems, namely the EC 114-Elan-Tech® and CR141-Sika Biresin®.

II.2.1 Rheological test on EC 114 resin system

The rheology tests have been performed using the rheometer AR2000 (Fig. II.14).

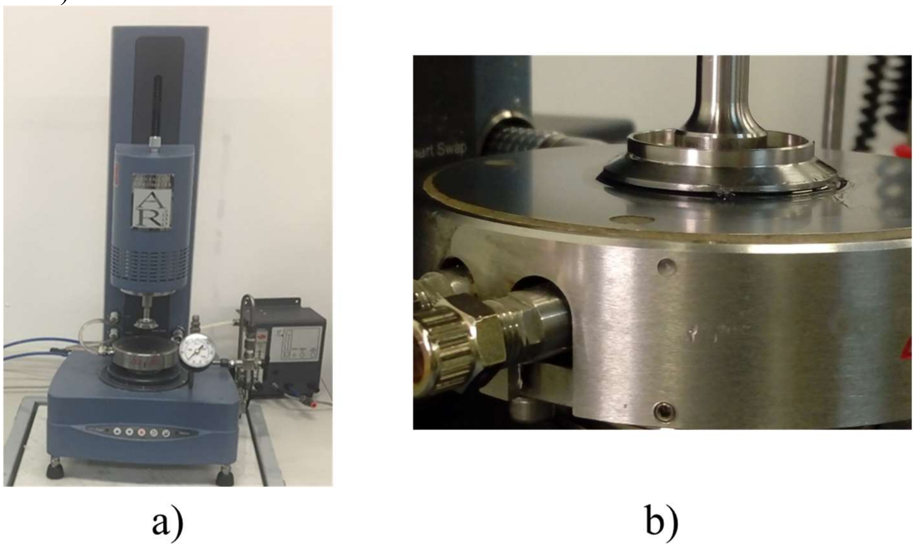

Figure II.14 *a) Rheometer AR2000; b) detail of the test execution.*

In order to define the value of the shear rate to be used during the experiments, a preliminary rheology test was performed at constant room temperature. In this test, the viscosity was evaluated using different shear rates $\dot{\gamma}$, ranging from 10^{-3} to 100 s^{-1}. The results are plotted in fig II.15.

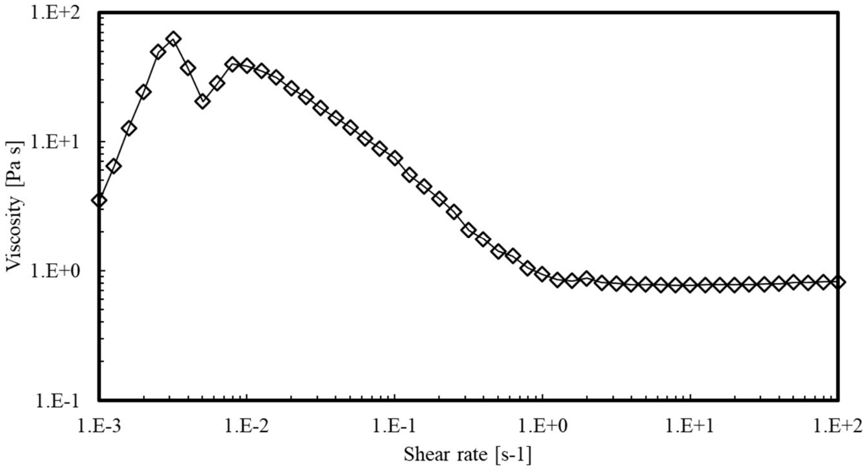

Figure II.15 *Rheological behavior of the epoxy system with respect to the shear rate.*

It can be noted that the viscosities measured using shear rates $\dot{\gamma}$ lower than 1 s^{-1} present variable values. For shear rates higher than 1 s^{-1}, the measured values reaches a stable plateau. Indeed, using low shear rates, the measured viscosities are not reliable due to the too slow movement of the rotational tool. The test is reliable using shear rates higher than 1 s^{-1}. Therefore, in the rheology tests, the value of shear rate was set equal to 10 s^{-1}.

The test were performed using preset heating ramps of 5, 10 and 15 °C/min. In Fig. II.16 the acquired viscosity profiles, measured with different heating rates, are plotted as function of the temperature. The tests have been interrupted at resin activation for the sake of the testing equipment security. In the same figure, the degree of cure of the resin, predicted using the reaction kinetic described by Eq. (II.24) and the parameters reported in tab II.1, is also shown for each of the test case.

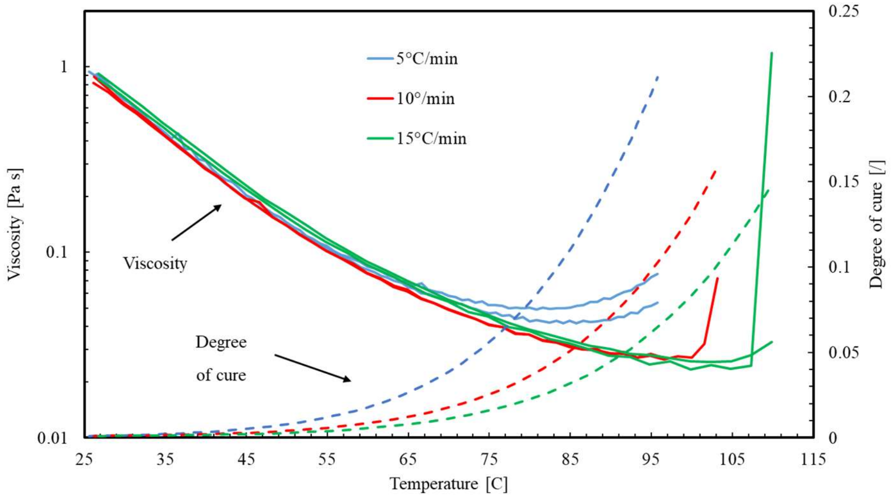

Figure II.16 *Rheological behavior of the epoxy system using different heating ramps.*

The viscosity presents an initial value of about 0.88 Pa s. It remarkably decreases while temperature rises from room condition. The minimum viscosity value is highlighted before the activation of the resin reaction. Afterward it sharply increases. Minimum viscosities result more than one order of magnitude lower, if compared to the room conditions. At low temperature, no remarkable differences between the viscosity profiles can be noted. The change in the slope of the viscosity profile is related to the cure reaction activation.

The profiles relative to the low heating rate present a controlled viscosity variation, while the fastest profiles exhibit a remarkably sharp activation. It is worth to note that in the faster heating rate cases, the minimum viscosity is lower and the activation occurs at higher temperature. The rheology behavior of the resin has been modeled accordingly to Eq. (II.26).

$$\eta = A_\eta \, exp\left(\frac{B_\eta}{R\,T} + C_\eta \alpha + D_\eta \alpha^2\right). \tag{II.26}$$

In Eq. (II.26) A_η, B_η, C_η and D_η are characteristic parameters of the reaction, R is the gas universal constant and α is the variable representing the degree of cure. The goodness of the model with respect to the experimental data has been evaluated by the correlation coefficient, which results equal to 0.9522. The values of the rheological parameters are reported in Tab. II.3. In Fig. II.17 the acquired data are compared to the developed model.

Table II.3 *Rheology parameters of the EC114 epoxy system.*

Symbol	Value	Unit
A_η	1.222E-11	[Pa s]
B_η	6.219E4	[J mol^{-1}]
C_η	9.750	[/]
D_η	1.264E1	[/]

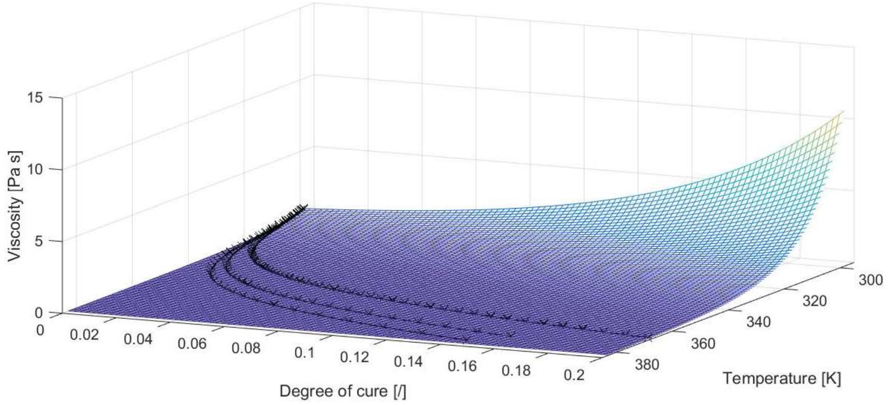

Figure II.17 *Model of the rheology behavior with respect to temperature and degree of cure.*

II.2.1 Rheological test on CR 141 resin system

The rheological behavior of the resin, i.e. the viscosity dependence on temperature, was inferred using a dynamic rheometer (MCR 301, Anton Paar GmbH), by imposing to the catalyzed resin temperature ramp from 25°C to 150°C and a heating rate of 5°C/min. The profile of viscosity in temperature is represented in Fig. II.18.

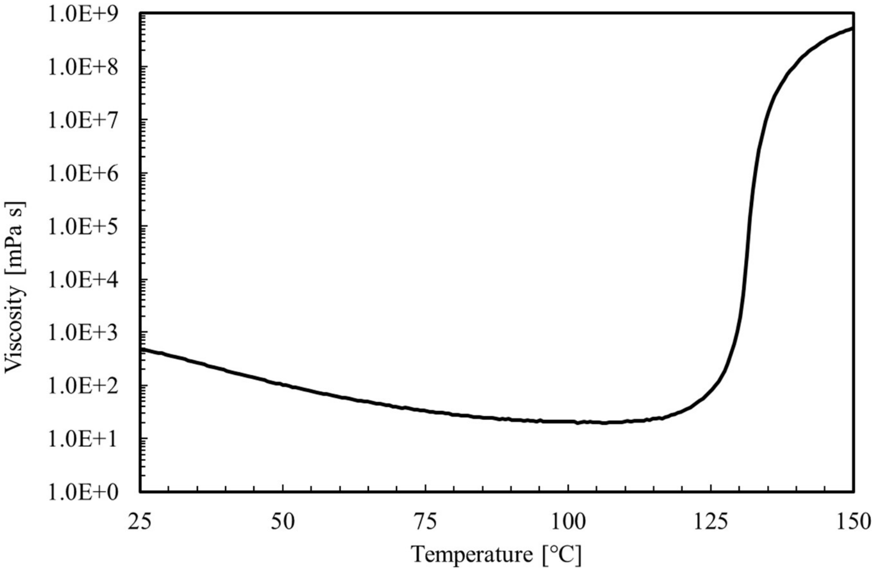

Figure II.18 *Rheology behavior of CR141 epoxy system with respect to temperature.*

The equation describing the resin viscosity η was extrapolated by regression from the obtained data, assuming the general rheological model, reported in Eq. (II.27) (Tucci *et al.*, 2020):

$$\eta = A_\eta \, exp\left(\frac{B_\eta}{R\,T} + C_\eta \alpha + D_\eta \alpha^2\right). \qquad \text{(II.27)}$$

Table II.4 *Rheology parameters of the CR 141 epoxy system.*

Symbol	Value	Unit
A_η	17.54	[Pa s]
B_η	732.2	[J mol^{-1}]
C_η	7.63	[/]
D_η	9.86	[/]

II.3 Dynamo-mechanical analysis

II.3.1 Generalities

The Dynamo-mechanical analysis (DMA) is a technique used to characterize the mechanical and the viscoelastic properties of materials at different temperature conditions. The DMA technique is based on the contemporaneous action of mechanical periodic load and heating ramps on material samples (Menczel and Prime, 2009). Several different load configurations, namely three-points bending, axial tensile, compressive or shear, are typically used (Menard, 2006).

The system evaluates the phase delay of the sample deformation with respect to the applied sinusoidal loads. Polymers typically exhibit a phase delay δ between the application of the stress σ_0 and the material deformation ε_0. The conservative (in phase) response is related to the elastic behavior. The elastic property related to the conservative behavior is the storage modulus E', while the property related to the dissipative aspects is the loss modulus E'' (Menard, 2006):

$$E' = \frac{\sigma_0}{\varepsilon_0} \cos\delta \, , \tag{II.28}$$

$$E'' = \frac{\sigma_0}{\varepsilon_0} \sin\delta \, . \tag{II.29}$$

Therefore, the output of DMA analysis are the evolution of the storage modulus, of the loss modulus and of the phase angle with respect to the time. The peak of the profile of $\tan\delta$ occurs at the resin glass transition (Menard, 2006). Assuming that the value of the glass transition temperature of the fully uncured resin ${T_g}^0$ is equal to 0°C (Ismet Baran, Akkerman and Hattel, 2014), the temperature relative to the peak of $\tan\delta$ corresponds to the variation coefficient of the glass transition temperature α_{Tg}.

II.3.2 Experimental tests

The CHILE model parameters of the ortophtalic polyester system (ESI resin GP med OT- Euroresins ltd.) have been defined using the dynamic mechanical analysis. The equipment used for this experimental activity is the DMA Q800 (TA instruments) (Fig. II.19).

a) b)

Figure II.19 *a) DMA Q800 equipment; b) tooling for three-points bending test.*

The resin samples prepared for DMA test had prismatic geometry and dimensions of 10.5 mm in length, 7.5 mm in width and 1.5 mm in thickness. The analyzed samples were preliminary cured in a laboratory oven for 15 minutes at isothermal temperature of 90°C, 100°C, 110°C and 130°C. The tests were performed using heating rates of 5°C/min, from 20°C to 200°C. The tests were performed in three-points-bending configuration, setting a loading frequency equal to 1 Hz. The data of storage modulus, loss modulus and tan δ are depicted in Figs. 2.20 to 2.23.

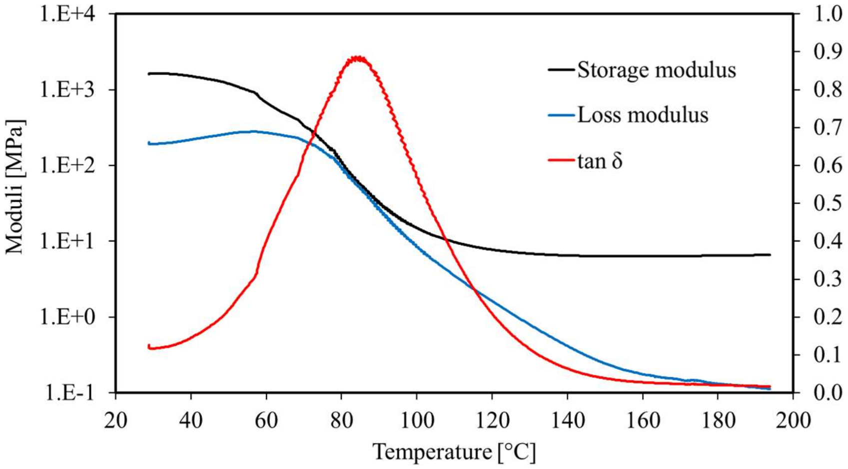

Figure II.20 *Moduli evolution (preliminary cure temperature=90°C).*

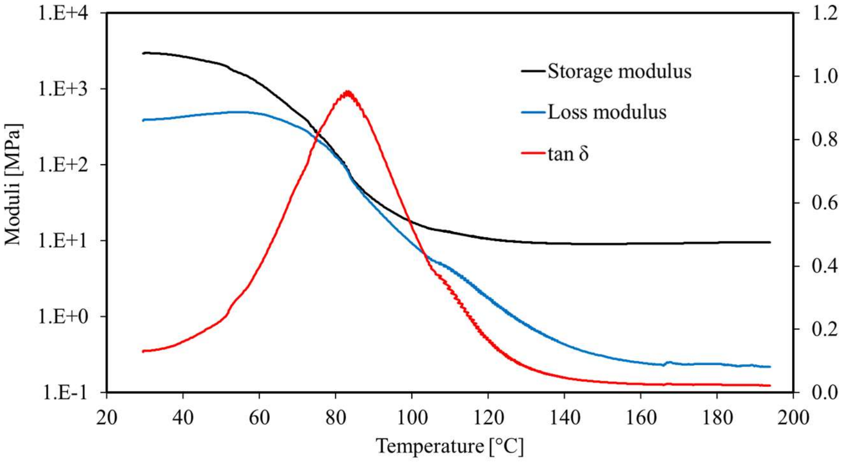

Figure II.21 *Moduli evolution (preliminary cure temperature=100°C).*

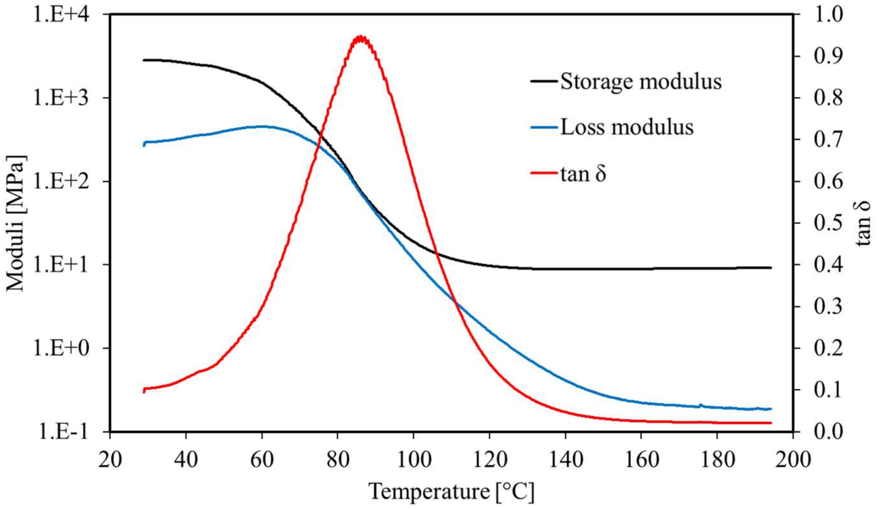

Figure II.22 *Moduli evolution (preliminary cure temperature=110°C).*

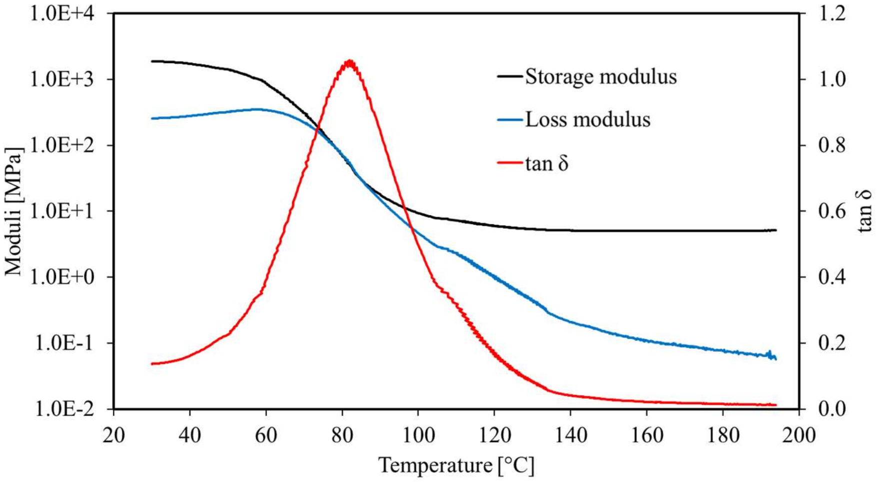

Figure II.23 *Moduli evolution (preliminary cure temperature=130°C).*

The peak of $\tan\delta$ profiles is equal to $83.8°C \pm 2\,°C$. Therefore, the variation coefficient of the glass transition temperature can be expressed as follows:

$$\alpha_{Tg} = 84°C\,. \tag{II.30}$$

The CHILE model parameters can be defined by regression using as input the storage modulus evolution. The computed parameters are reported in Tab. II.5. Fig. II.24 compare experimental data with the computed CHILE model.

Table II.5 *CHILE model parameter for ortophtalic polyester system.*

Symbol	Value	Unit
T_{C1}	-60	[C]
T_{C2}	30	[C]
T_{C3}	110	[C]
E_0	0.0195	[GPa]
E_1	0.73	[GPa]
E_∞	3.76	[GPa]
A_e	0.20	[GPa]
B_e	0.043	[C^{-1}]

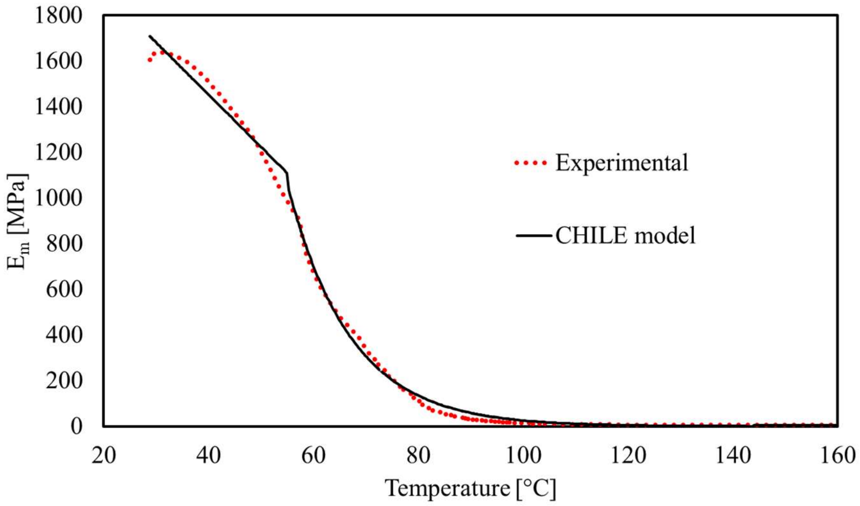

Figure II.24 *Resin modulus evolution with respect to the temperature.*

Chapter III
Resin flow model

III.1 Resin flow modeling in pultrusion

One of the fundamental steps in fiber reinforced composites manufacturing is the combining of the liquid resin and the fibrous reinforcement. This operative step is also referred as impregnation. In pultrusion processes of thermoset composites, the fiber impregnation can occur in two different modalities: by fiber immersion or by resin injection (Correia, 2013). According to the fiber wetting modality, the process is classified in open bath (conventional) pultrusion (Baran, Tutum and Hattel, 2013) or in injection pultrusion (Ranga *et al.*, 2011). In open bath process, the fiber reinforcement is driven through a resin pool upstream the heating-forming die (Starr, 2000). In injection pultrusion process, the resin is injected through the advancing fibers within an injection chamber (Ding *et al.*, 2000).

The open bath process is a well-established technique, which guarantees robust performances and requires remarkably simple equipment (Baran, 2015). On the other hand, injection pultrusion provides interesting advantages, mainly related to the reduced volatile compounds emission, the possibility of processing resin formulations of shorter pot life and the quality control (Voorakaranam, Joseph and Kardos, 1999).

The injection chamber is, in the most of the cases, bolted to the curing die in order to provide continuity to the chamber and the die cavities (Masuram, Roux and Jeswani, 2016). In some cases, die-detached injection chambers have been experimented (Palikhel, Roux and Jeswani, 2013). The injection chamber described in scientific papers and applied in industry are classified according to the geometry of their cavity: straight (Jeswani and Roux, 2006; Spangenberg *et al.*, 2017), tapered, teardrop, siphon, high-pressure (Strauß, Senz and Ellinger, 2019).

In last two decades, many authors developed numerical models to study the resin flow in injection pultrusion (Liu, 2003; Masuram, Roux and Jeswani, 2017), aiming at the prediction of the resin flow using different operative parameters. Particular interest was devoted to the sensitivity of the process to the variations in operative parameters (Jeswani and Roux, 2007a; Shakya, Roux and Jeswani, 2013) or in cavity geometry (Jeswani and Roux, 2008; Ranga *et al.*, 2011).

It is worth to mention that, although the remarkable effort and the massive production of studies, resin flow modeling in pultrusion is an open topic, which still presents several challenges to deal with. The numerical models published assume non-reactive resin, isothermal conditions, monophasic fluid (without air or additives) or homogeneous fibrous medium.

The fibrous reinforcement is commonly modeled as a bulk porous body (Alexander A. Safonov, Carlone and Akhatov, 2018).

The three-dimensional resin flow continuity is described by Eq. (III.1) (R. Gorthala, Roux and Vaughan, 1994):

$$\frac{\partial \rho\, \varphi}{\partial t} + \sum_i \frac{\partial (v_i\, \rho\, \varphi)}{\partial x_i} = 0\,. \tag{III.1}$$

In Eq. (III.1), x_i is the i-th direction of the space, v_i is the flow velocity in the i-th direction and φ is the medium porosity and ρ is the fluid density. The momentum equation of the resin flow in a porous medium is modelled by the Darcy law (Sharma *et al.*, 1998), as reported in Eq. (III.2):

$$v_i = V_i - \frac{K_{ii}}{\eta\, \varphi} \frac{\partial P}{\partial x_i}\,. \tag{III.2}$$

In Eq. (III.2) V_i is the fiber velocity in i-th direction; K_{ii} is the bundle permeability; η represents the viscosity and P is the pressure. In straight cavities the fibers velocity is assumed equal to the pulling speed. The velocity components in transversal directions are hypothesized null. Nevertheless, in the tapered chamber, the fiber compacting implies a movement of the fibers in the transversal directions (Gadam *et al.*, 2000).

The model described in Eqs. (III.1) and (III.2) accounts for one unique fluid phase. Nevertheless, as earlier stated, air phase is also present. Air bubbles can be embedded and drag, accordingly to the pressure and viscosity conditions. Neglecting mass transfer between the two fluids or mass generations, the governing equations (Eqs. (III.1) and (III.2)) for the j-th fluid phase can be expressed as follows (Tucci *et al.*, 2020):

$$\frac{\partial \rho_j\, \varphi}{\partial t} + \sum_i \frac{\partial (v_i\, \varphi)}{\partial x_i} = 0\,, \tag{III.3}$$

$$v_{i,j} = V_i - \frac{K_{ii}}{\eta_j\, \varphi} \frac{\partial P}{\partial x_i} + D_{j,k}\,. \tag{III.4}$$

In Eq. (III.4) the term $D_{j,k}$ represents the velocity contribution given by the viscous drag of the k-th phase on the j-th phase (Gascón *et al.*, 2016). As described in the previous chapter, resin properties are sensitive to the temperature and the thermochemical condition. Therefore, the thermal expansion and the viscosity evolution should be properly considered. The rheology dependence on temperature and degree of cure has been already discussed in the previous chapter. The thermal expansion is expressed as a variation in resin density ρ_m, as described by the following relations (Eq. (III.5)):

$$\rho_m = \frac{\rho_{m,0}}{(1+CTE_m\,T)}\,. \tag{III.5}$$

In Eq. (III.5) CTE_m represents the matrix coefficient of thermal expansion and $\rho_{m,0}$ is the density of the resin at room temperature (25°C).

The approach described has been used in the flow modeling described afterword.

III.2 Reinforcement permeability models

According to the Darcy model (Eq. (III.2)), the permeability K_{ii}, is a key parameter affecting the velocity of the resin flow. It is a property of the porous medium, which measures the ability to transmit fluids. Permeability of a fibrous depends on its porosity, on the mean diameter of the fibers and on the fiber compactions. The porosity of the fibrous reinforcement φ is the volume between the fibers. It can be evaluated as the complement to unit of the reinforcement volume fraction (Eq. (III.6)):

$$\varphi = 1 - V_f\,. \tag{III.6}$$

Several models have been proposed to evaluate the permeability of fibrous bundle. The Kozeny-Carman model (Eq. (III.7)) is one of the most commonly used to calculate the permeability of fiber bundles (Carman, 1997):

$$K = \frac{R_f^2}{4\,k}\frac{\left(1-V_f\right)^3}{V_f^2}\,. \tag{III.7}$$

In Eq. (III.7) R_f is the fiber mean radius, k is a constant parameter and V_f is the reinforcement volume fraction. The permeability term K does not present any directional subscript, since the Kozeny-Carman theory assume the porous material as isotropic in nature. Nevertheless, this assumption is not valid in the pultrusion, due to the fibrous architecture, mainly constituted by unidirectional rovings (Gutowski, Morigaki and Cai, 1987). The Kozeny-Carman model has been later extended by Gutowski et al. to evaluate the longitudinal permeability K_{LL} (Eq (III.8)) and the transversal permeability K_{TT} (Eq. (III.9)) of a transversally isotropic porous medium (Gutowski, Morigaki and Cai, 1987), leading to the following equations:

$$K_{LL} = \frac{R_f^2}{4\,k}\frac{\left(1-V_f\right)^3}{V_f^2}\,, \tag{III.8}$$

$$K_{TT} = \frac{R_f^2}{4\,k\prime}\frac{\left(\sqrt{V_a\prime/V_f}-1\right)^3}{V_a\prime/V_f+1}\,. \qquad \text{(III.9)}$$

In Eq. (III.9) k' and V_a' are empirical parameters.

Gebart (Gebart, 1992) proposed a permeability model of unidirectional reinforcement based on geometrical consideration. The model was developed for two fiber arrangement cases, namely the quadratic and the hexagonal fiber packing (Fig. III.1). In Gebart model, fibers disposition is accounted using the calibration parameters c and C_1:

$$K_{LL} = \frac{8\,R_f^2}{c}\frac{\left(1-V_f^2\right)}{V_f^2}\,, \qquad \text{(III.10)}$$

$$K_{TT} = C_1\left(\sqrt{\frac{V_{f,max}}{V_f}}-1\right)^{2.5} R_f^2\,. \qquad \text{(III.11)}$$

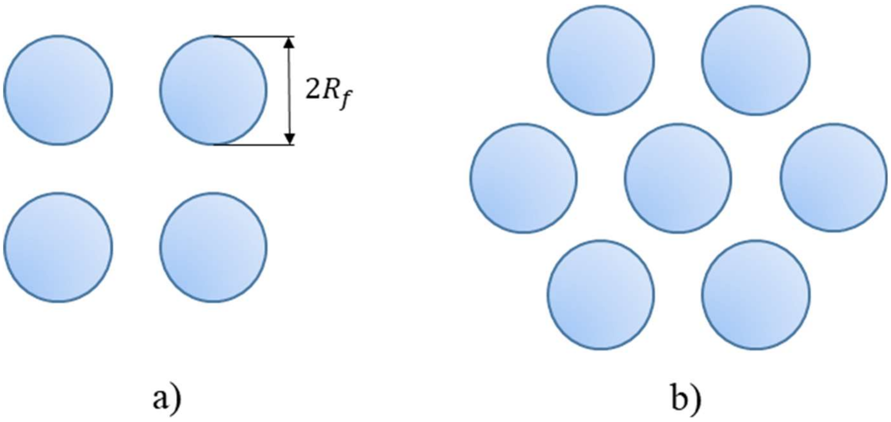

Figure III.1 *Fiber packing schemes: a) quadratic; b) hexagonal.*

III.3 Experimental tests

In this work, the IP process was performed on a pultrusion line equipped with sensors for temperature, pressure and pulling force and speed acquisition available at Fraunhofer IGCV (Augsburg, Germany). Epoxy resin (Sika Biresin® CR141) was used as matrix and E-glass fibers rovings (3B Advantex® 399) as reinforcement. Rectangular 60 mm wide and 5 mm thick profiles were pultruded. Fig. III.2 shows the injection chamber employed in this experiment. Fig III.3 reports the schematic representation of the tapered cavity.

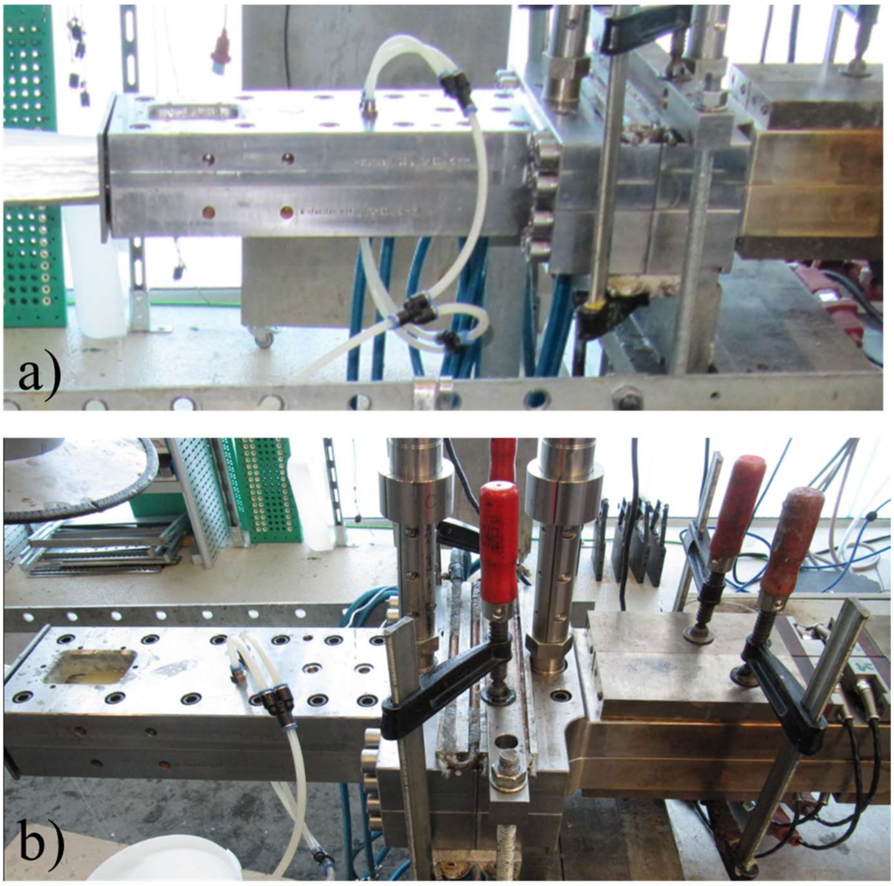

Figure III.2 *Lateral (a) and obliquus (b) view of the injection chamber.*

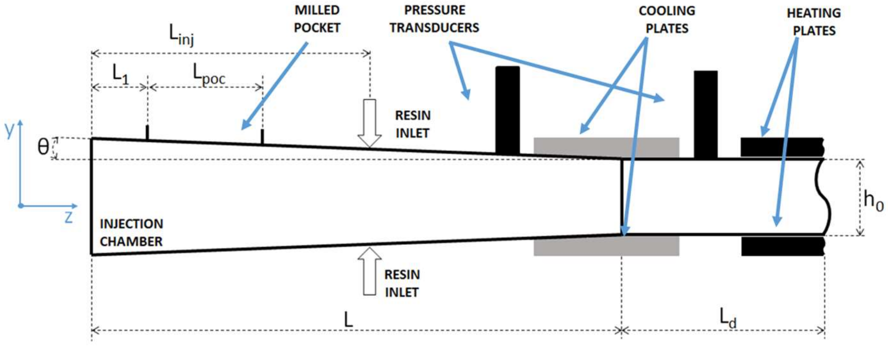

Figure III.3 *Schematic representation of the injection chamber geometry.*

The injection chamber, schematically represented in fig. III.3, consists of in a 500 mm (L) long tapered cavity, which gradually converges to the cavity inlet. The tapering angle (θ) is 1.6° wide. The resin flows into the chamber through four injection nozzles, located at a distance of 250 mm (L_{inj}) from the chamber inlet. Two of them on the top surface and two on the bottom surface of the tapered cavity. On the top surface the chamber presents a 90 mm (L_{poc}) wide milled pocket, allowing the operator to observe the material in the chamber and tune the process. The milled pocket starts at a distance of 15 mm (L_1) from the inlet.

Two pressure transducers (Dynisco SPX2292, measurement range 0-70 bar), mounted in such a way that the sensitive surfaces are aligned to the cavity walls, were used to measure the pressure during the trials. The first pressure transducer is located in the tapered chamber at 435 mm from the inlet, while the second one is located in the straight portion of the die at 70 mm from the junction between die and chamber. The 1000 mm long die has been heated by electrical platens fixed on the top and the bottom external surface of the steel die. Their temperature has been regulated by a control system at 180°C.

The pultrusion tests have been performed setting the resin injection pressure equal to 2.5 bar. Two pulling speeds, namely 300 mm/min and 500 mm/min, have been used in the pultrusion experiment. The temperature development of the material being processed was measured by means of J type (iron-constantan) traveling thermocouples, i.e. fixed to the fiber reinforcement being pulled. More specifically, the thermocouples were adhesively bonded to the reinforcement with the sensitive bulb placed in opportunely selected rovings, i.e. at the barycenter point of the composite cross-section and at the center of the top surface of the workpiece, close to the die cavity.

The results sampled during the run along the injection chamber and the die were referred to the distance from the injection chamber inlet, taking into account the speed imposed by the pulling system.

III.4 Numerical modeling of resin flow in pultrusion

The numerical model presented in this chapter simulates the injection pultrusion of a rectangular cross-section profile, made of E-glass fiber reinforced epoxy (Sika Biresin® CR141). During the process, the catalyzed resin is pumped into the injection chamber, where it flows through the moving reinforcing fibers. The unidirectional fiber reinforcement was modeled as a moving porous medium, with variable, volume fraction, porosity, and permeability, depending on the chamber geometry.

In more detail, since the tapered shape of the cavity compresses the reinforcement, less free volume is progressively left to the resin flow along the injection chamber. For the considered geometry, such behavior can be described as follows:

$$V_f = \frac{h_0 V_{f,0}}{2\, tan\theta(L-z)+h_0}. \qquad \text{(III.12)}$$

In Eq. (III.12) $V_{f,0}$ is the pultruded volume fraction of fiber and z is the longitudinal coordinate, with origin at the barycenter of the inlet of the injection chamber. Eq. (III.12) indicates that the fiber volume fraction, and consequently the porosity, is a function only of the longitudinal position, while it is constant in the transversal cross-section. Reinforcement porosity was inferred as the complement to unit of the volume ratio of fiber (Eq. (III.6)). It should be noted that the porosity of the reinforcement was assumed as a function of the longitudinal coordinate z, thus modeled as constant in transversal directions x and y. This means that the reinforcing material is assumed homogeneously distributed in each cross-section, even where the fibers are not uniformly spread and completely fill the available volume. The permeability of the fibrous reinforcement was derived using the Gebart model (Gebart, 1992) (Eqs. (III.10) and (III.11)). In particular, the behavior of a hexagonal fibers' arrangement was assumed, congruently with microstructure observations reported in section III.5.

The advancement of the porous medium within the injection chamber was imposed assuming a linear movement of each fiber/roving. This movement was defined according to the shape of the cavity and neglecting fiber displacements due to the pressure of incoming fluid (fluid-solid interaction) as well as the mutual contact between fibers (solid-solid interaction). Consequently, the velocity of the porous medium is constant in magnitude, given by the pulling speed, but the components of the velocity vector depend on the position. Taking into account that the width of the injection chamber and of the die cavity are equal, it follows:

$$\begin{cases} V_x = 0\,; \\ V_{\mathrm{y}} = -\mathrm{V}\sin\gamma\,; \\ V_{\mathrm{z}} = \mathrm{V}\cos\gamma\,. \end{cases} \tag{III.13}$$

In Eq. (III.13) V_x, V_y and V_z are respectively the components of the pulling velocity V in transversal and longitudinal direction, and γ is the angle formed, in the $y - z$ plane, between the fiber velocity vector and pulling speed. The dependence of γ on the coordinates can be written as follow:

$$\gamma = \tan^{-1}\left(\frac{y-y\prime}{L-z}\right), \tag{III.14}$$

being y' given by:

$$\mathrm{y}' = \left(y - \frac{h}{2}\right)\left(\frac{h_0}{h}\right) + \frac{h_0}{2}\,. \tag{III.15}$$

In eq. (III.15) h is the height of the chamber at the coordinate z and h_0 is the height of the straight portion of the cavity, which is equal to 5 mm in the present case.

The fluid phases flow through the advancing fibrous reinforcement is governed by Eqs. (III.3) and (III.4). The epoxy system viscosity was evaluated and modelled in section II.3 (Eq. (II.27)). The air was considered in the model as an ideal gas. Air inclusions have been modeled as a dispersed fluid. The term $D_{i,j}$ in Eq. (III.4) has been defined according to the Schiller-Naumann model and account for the density and viscosity of the continuous fluid phase as well as for the velocity difference between the two fluids. The resin flow modeling included the thermal expansion described by Eq. (III.5).

The described model has been implemented in ANSYS-CFX computational software. The employed simulation parameters are reported in Tab. III.1.

Table III.1 *Simulation parameters.*

Symbol	Parameter	Value
R_f	Fiber radius (Eq. (III.10)-(III.11))	12.08 [µm]
V	Pulling speed (Eq. III.13)	300-500 [mm/min]
φ	Final porosity	0.30
$\rho_{r,0}$	Resin density at room temperature (Eq. III.5)	1260 [kg m^{-3}]
CTE_r	Epoxy coefficient of thermal expansion (Eq. III.5)	1.35E-4 [C^{-1}]

The computational domain was defined by the tapered cavity of the injection chamber and the early portion of the straight region of the curing die, in order to exclude the activation of the reaction. The length of the constant cross-section domain was defined as 150 mm and 200 mm for pulling speed equal to 300 mm/min and 500 mm/min, respectively.

A solid model of the experimental setup described in section 3.3 was discretized using hexahedral elements, whose dimensions are averagely equal to 1 mm. In the earliest steps of the simulation, resin flow is expected to be remarkably faster than in the rest of the simulated time domain. In order to avoid numerical instability due to sharp variations in resin volume fraction, the earliest 10 s of the simulation were discretized with 0.1 s time steps, while all the remaining intervals have been discretized with 0.5 s time steps.

The balance equations were solved by imposing the following boundary conditions (Fig. III.4) (Rahatekar and Roux, 2003; Jeswani and Roux, 2007b, 2008; Ranjit, Roux and Jeswani, 2013):

- The entrance of the chamber and the milled pocket section are modeled as opening sections, through which air and resin flows are allowed in both the directions, the pressure value is set at 1 bar (environmental pressure) and a zero-gradient condition was imposed on the fluid flow pressures;
- The injection slots were modeled as inlet surfaces through which only resin entrance is allowed. In these sections the resin injection pressure is set as boundary condition;
- A controlled velocity condition was imposed on the exit section of the domain, where fluids velocity converges to fiber velocity, and therefore to pulling speed;
- A free slip condition was applied on all the remaining surfaces.

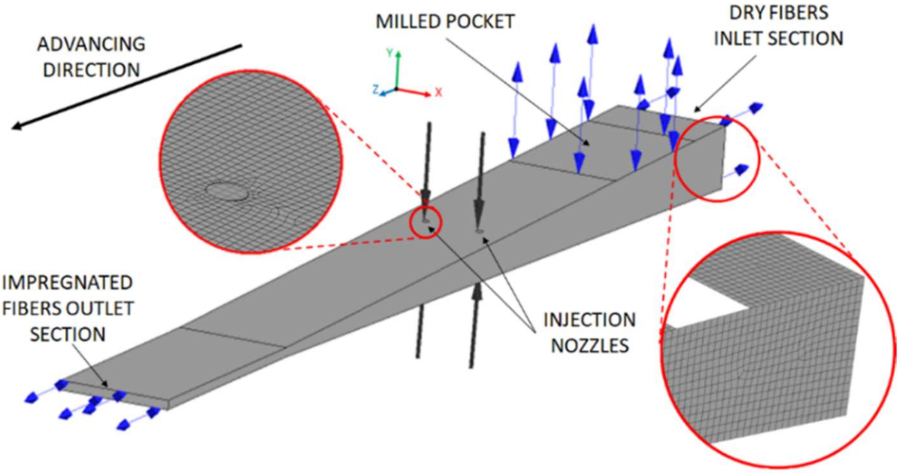

Figure III.4 *Applied boundary conditions and domain the discretization.*

III.5 Validation

Fig. III.5 shows two representative samples of the produced pultruded profiles, as well as a schematic view of the points, randomly chosen in the profile section, for microstructure analysis. In the same figure are reported some representative microstructural images captured by optical microscope. The microscopic images were observed to infer the actual fiber diameter, arrangement, and the volume fractions.

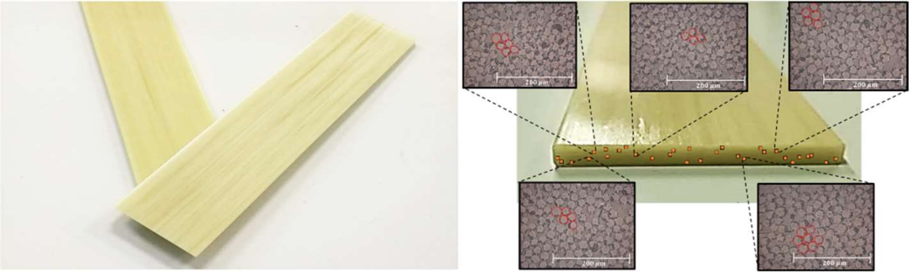

Figure III.5 *a) Pultruded profile samples; b) Schematic view of the observed randomly selected points.*

Overall, 30 images were acquired from different locations in the cross-section of samples manufactured in the indicated conditions and then analyzed. The fiber volume ratio was found to range from 65.7% to 73.4%, with an average value and a standard deviation equal to 70.1% and 2.2%, respectively. As can be deduced from the indicated values, the reinforcement distribution within the pultruded profile is not strictly uniform, with some zones characterized by an excess of resin. On the other hand, the fiber packing seems to reasonably approximate a hexagonal arrangement, consistent with the adopted permeability model (Eqs. (III.10) and (III.11)) (Gebart, 1992). The same analysis was carried out for voids. The microstructural analysis highlighted the opportune setting of processing parameters in both cases, providing a very low average void fraction, equal to 0.025% working at 300 mm/min and 0.016% working at 500 mm/min, computed averaging the observations performed on all the images, whereas, in most cases, no voids were found. Finally, the micrographic analysis highlighted that the average fiber diameter was equal to 24.16 μm with a standard deviation of 1.03 μm.

Fig. III.6 shows two typical temperature profiles acquired by the thermocouples, at the center and at the top of the cross-section of the pultruded composite respectively, for both the investigated pulling speeds. The curves are plotted in the space domain as a function of the distance from the inlet of the injection chamber.

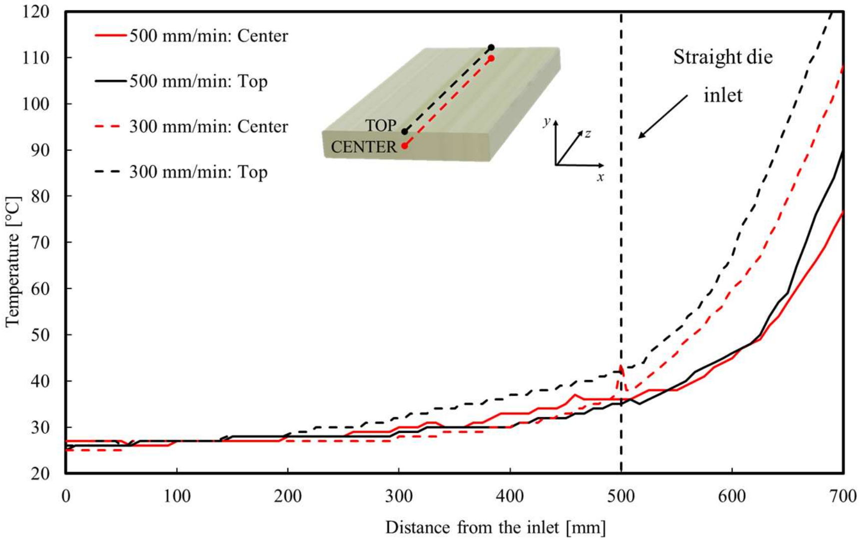

Figure III.6 *Acquired temperature profiles in the injection chamber along central and top paths.*

In the injection chamber the increase of temperature was obviously smoother, being approximatively equal to 10°C and 20°C for pulling speed of 500 mm/min and 300 mm/min. In fact, in the former zone, the heat generated by the plates is thwarted by the effect of the cooling plates fixed to the external surfaces of the steel die at the junction between die and chamber. Nevertheless, the viscosity variation associated to this temperature increase is still significant, ranging from about 0.5 Pa s at room condition to 0.02 Pa s at 100 °C.

As far as pressure measurement is regarded, the average pressure under the sensor was measured to be 10.2 ± 0.5 bar in the injection chamber, rising up to 27.1 ± 0.5 bar within the straight portion of the die for the pulling speed of

300 mm/min. In the case of 500 mm/min pulling speed, the pressure was measured as 13.2 ± 0.5 bar in the tapered chamber and 50.0 ± 0.5 bar in the straight cavity.

The pressure profiles at the centerline of the processing composite are reported and compared with experimental measurements from sensors in Fig. III.7.

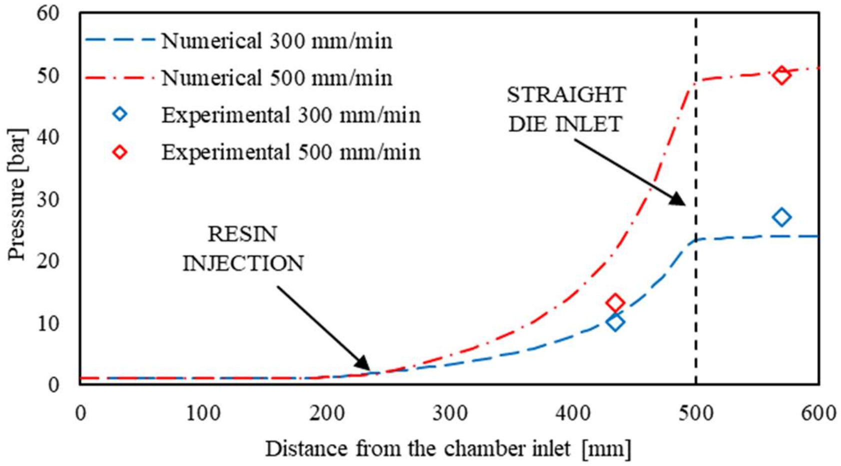

Figure III.7 *Comparison of numerical and experimental pressure outcomes.*

The computed pressure curves for both the pulling velocities exhibit a similar trend. In the earliest segment of the tapered chamber, the pressure of the fluids reflects the atmospheric value of one bar, set as boundary condition at the entrance and at the milled pocket. At a distance of 200 mm from the inlet, an increase in pressure is estimated, as an expected consequence of the resin injection. More precisely, this increase was detected 50 mm upstream of the injection nozzles, located at 250 mm from the inlet and is clearly attributable to the backflow of liquid resin, which, before being dragged by the advancing fibers, naturally moves toward lower pressure regions.

Pressure sharply increases in the second half of the tapered chamber, due to the compression of the bundles and the consequent reduction in porosity. In fact, the fiber package drags the resin towards the narrower cross-section, where the free space available for the fluid flow decreases. Moreover, the reduction of the porosity implies a decrease of permeability in all the directions, according to Eq. (III.12).

Lower permeability, according to Darcy law, obstructs resin mobility and, therefore, promotes the drag. The liquid incompressible resin, forced in narrower spaces, generates the increase in pressure. The pressure gradient sharply reduces at the junction between the injection chamber and forming die, corresponding to the black dashed line coordinate in Fig. III.7. This is attributable to the fact that at the beginning of the straight portion of the cavity the material is not furthermore compressed.

Fig. III.7 highlights that the imposed pulling speed strongly influences the pressure increase. Indeed, the porous medium advances faster, the drag action is more significant and, therefore, a greater amount of resin is displaced forward generating a higher pressure level, as also confirmed by some articles in literature (Jeswani and Roux, 2008; Palikhel, Roux and Jeswani, 2013; Ranjit, Roux and Jeswani, 2013). The calculated profiles, as well as the effect of the pulling speed on the maximum achieved pressure qualitatively, agree with the outcomes of the research discussed in (Jeswani and Roux, 2008; Palikhel, Roux and Jeswani, 2013; Ranjit, Roux and Jeswani, 2013).

It is worth noting, however, that, differently from the present work they explored very higher pulling speeds in a shorter tapered cavity. Consequently, from a quantitative point of view, some discrepancies in the reported values are well understood. It should be also considered that temperature-related effects, namely viscosity variation and thermal expansion of materials, were not taken into account in the cited works (Jeswani and Roux, 2008; Palikhel, Roux and Jeswani, 2013; Ranjit, Roux and Jeswani, 2013).

Fig. III.7 also points out that the numerical outcomes fairly capture the physics of the process. The difference between the experimental acquisition and the numerical results at the chamber pressure transducer (435 mm) has been attributed to the hypothesis of homogeneous distribution of porosity and permeability in the cross-section, assuming their variability only as a function of the longitudinal coordinate.

It means that each single fiber tow, while advancing, rigidly converges toward the symmetry plane of the transversal section, without any displacement effects induced by the injected resin. In a real process, however, fibers reasonably follow stochastic arrangements and exhibit a compliant behavior (Bodaghi *et al.*, 2018). This condition, which is correct from a macroscopic point of view, generates local divergences whereas the fibrous reinforcement is still not totally compacted.

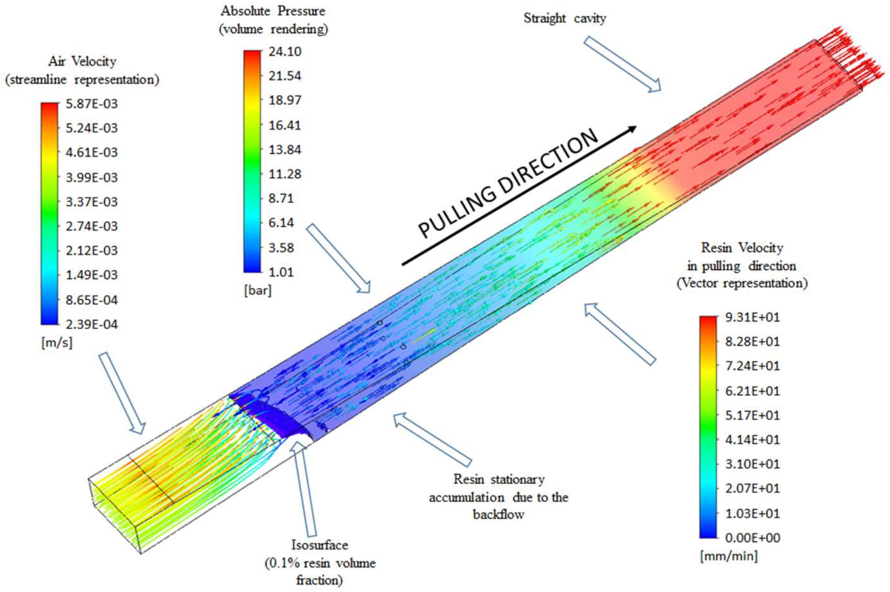

Figure III.8 *Predicted fluid flows and pressure field in the computational domain.*

Fig. III.8 reports a typical simulation result of the resin and air movement inside the injection chamber and at die inlet, as well as the pressure distribution in the same region for the simulation launched assuming the pulling speed as 300 mm/min. More precisely, the streamlines at the opening of the chamber for the fiber inlet represents the air flow and chromatically reflects the air real velocity. The resin flow is represented in the same figure by means of colored vectors, whereas colors indicate the velocity along the pulling direction, which ranges from an absolute value of 0 m/s to a maximum value equal to the pulling velocity.

The volume rendering depicts the absolute pressure distribution, shared by both the fluid phases and highlighted, in the interest of clarity, only in the region characterized by the presence of resin ($V_f \geq 0.001$). Please notice that different color scales are used for different plots, as indicated in the figure.

The numerical results evidenced that the advancing reinforcement is poor of resin in the earliest region of the tapered chamber. About 50 mm upstream of the inlet nozzles the resin volume fraction increases very sharply.

The presence of resin upstream the nozzles is related to the backflow, shown also by the vectors, many of which are directed backward in this zone and leading to the establishment of a region of pseudo-stationary accumulation of resin. The backflow front position is coherent with the pressure curves depicted in Fig. III.7, in which the pressure rise starts at a distance of 200 mm from the inlet because of the presence of resin in that position. In practice, the resin penetrates into the porous region and is “captured” and transported by the advancing reinforcement.

The intersection of the flows coming from the different slots in the tapered chamber promotes a homogeneous impregnation and a low presence of entrapped air (Rahatekar and Roux, 2003; Masuram, Roux and Jeswani, 2016).

Fig. III.8 also highlights that the resin velocity is almost null in the backflow region, where the porosity of the reinforcement is highest, while it increases whereas the fiber volume ratio is higher and therefore, the advection effect is stronger. Indeed, the pressure field pushes the resin backward and does not allow it to flow freely in the advancing direction.

As reasonably expected, at the end of the tapered region, the transverse flow of the resin vanishes and the velocity experienced by the resin approaches the highest value that is imposed by the pulling speed. Congruently with the Darcy model, the pressure distribution significantly affects the movement of the air phase, preventing it to freely enter into the die cavity.

As can be seen in Fig. III.8, the increase in pressure induced by the simultaneous movement of the fiber along the pulling direction and the opposite flow of the excess resin (backflow) forces the air to escape from the domain through the opening window, where the pressure is at the atmospheric level. This is undoubtedly one of the most significant advantages of the tapered shape of the injection chamber, since it guarantees a minimum amount of void fraction if processing parameters are opportunely set.

The implemented model predicts an average volume fraction of air equal to 0.021% in case of advancing velocity of 300 mm/min, whereas it resulted as 0.018% at pulling speed of 500 mm/min. The void fraction, at distinct processing conditions, is ruled by different factors, namely the established pressure distribution, the temperature field (affecting the resin viscosity), and the drag action played by the fibers.

It should be noted that the aforementioned effects are generally characterized by mutual interaction, as mathematically summarized also in the adopted modification of the Darcy model reported in Eq. (III.2).

In concept, if the fiber movement is assumed as a stand-alone factor without fiber compaction and transversal velocity component (linear movement of the fibers along the pulling direction in a straight cavity), the same drag effect is applied on both fluid phases, being the pressure increase attributable only to the resin injection. Consequently, the air fraction entrapped by the incoming resin flow fronts is naturally pulled through the die and embedded in the pultruded product. Assuming the same injection pressure, in this hypothetical case, it obviously comes that the higher the pulling speed, the higher the void content.

However, in any real IP process, the convergent shape of the injection cavity is designed on purpose to compact the advancing material and increase the fluid pressure. The pressure rise, as evident also looking at the numerical and experimental data in Fig. III.7, is directly related to the pulling speed for the above reported reasons. It follows that, at higher pulling speeds, the influence of the pressure gradient on the fluid flow is more significant and this is particularly valid for the low viscosity phase (air) which tends to flow back toward the entrance of the chamber and the opening window. At the same time, this removal mechanism of the entrapped air is also facilitated by the fact that increasing the pulling speed the region of pseudo-stationary accumulated resin naturally reduces.

Finally, it should be also considered that different pulling speeds imply different temperatures and, consequently, different viscosity profiles for the processing resin. This aspect amplifies the difference in the relative motion between the fluid phases, providing faster air backflow pulling the material at 500 mm/s with respect to 300 mm/s.

The predicted value of air volume fraction at the end of the simulation domain was found to be fairly close to the experimental case. In this regard, it should be also considered that the implemented model does not take into account void collapse and growth attributable to thermal, chemical, and other effects established in the curing die, therefore the slight difference between prediction and measurement is still acceptable.

III.6 Effect of properties variation

In order to evidence the impact attributable to temperature and viscosity variation on the prediction of pressure distribution and void volume fraction, some additional simulations were launched at constant resin viscosity and without thermal expansion. In particular, per each pulling speed two extreme viscosities, namely the minimum reached in the injection chamber, equal to 0.02 Pa s, and the room temperature viscosity, equal to 0.5 Pa s, have been set, with the same boundary conditions, and the computed pressure profiles were compared.

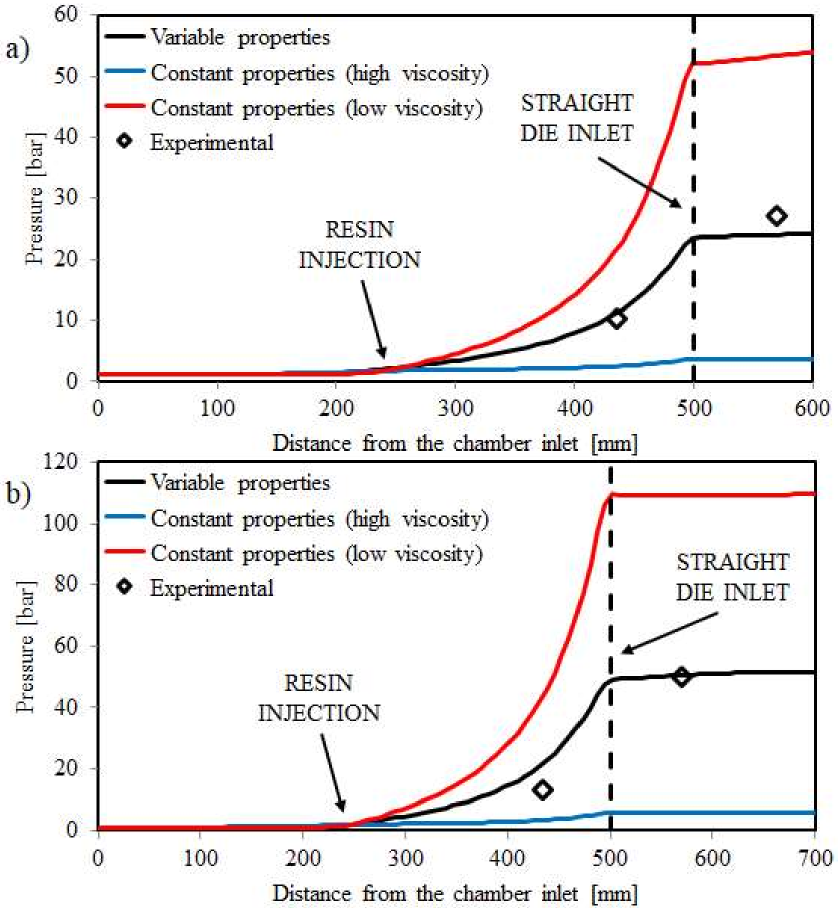

Figure III.9 *Effect of viscosity on pressure for pulling speeds of (a) 300 mm/min and (b) 500 mm/min.*

As can be seen looking at the pressure profiles along the centerline (Fig. III.9), unacceptable discrepancies with experimental evidences are evident if thermally induced variations are not considered in the calculation. A similar behavior was found in both the considered processing conditions. Assuming the resin viscosity as constant at 0.5 Pa s, the fluid pressure, represented by the red lines in Fig. III.9 (a) and (b), approaches values about 95% and 120% higher than the experimental one collected respectively at 300 and 500 mm/min.

The following explanation is provided. At higher viscosity value, the resin flow through the fibers is slowed down, as dictated by the Darcy law. Consequently, a major amount of resin is forced to move toward the reduced cross section of the injection chamber, experiencing a stronger compaction, which numerically corresponds to an excessive increase in pressure. In the low viscosity cases, depicted by the blue curves, the opposite scenario is materialized and the fluid pressure was computed, for both the pulling speed, as approximately the 10% of experimental acquisition. It should be also considered that, at low viscosity, the liquid resin flows relatively easier also in backward direction, resulting in a more consistent backflow. This behavior is confirmed by the pressure profiles, showing, for both pulling speeds, a slight but premature increase in pressure in the earlier zone of the chamber.

Similarly, the prediction of void fraction appears strongly affected by the used assumptions concerning the thermally induced variations of properties. Indeed, at lower speed the void fraction was computed as 2.59% and 0.77% respectively for the cases of high and low viscosity, while in case of higher pulling velocity it was estimated as to 0.51% and 0.40%, respectively. The discrepancy of these results from what obtained using the full model and confirmed by the experiments can be explained taking into account what aforementioned concerning the pressure distribution as well as considering the effect of viscous drag applied by the resin on the air. Indeed, assuming a low viscosity value in the entire domain, the lower pressure induced by the faster resin flow through the porous medium is not able to completely prevent the air to enter in the straight die region. In other words, the term $D_{j,k}$ of Eq. (III.4) (solved for the air) prevails on the second one and a relatively major amount of air is pulled in the die. Clearly, being the pressure higher at higher pulling speed, it is reasonable also to have a minor amount of void simulating the case at 500 mm/s without thermal effects. On the other hand, assuming higher viscosity the mutual interaction between the fluid phases given by the viscous drag is not negligible. Thus, even if the higher pressure tends to promote a stronger backflow of the air, at the same time the advancing resin “captures” the dispersed air forcing it to enter into the die.

III.7 Pulling speed influence

The influence of the injection pressure, as highlighted by the numerical simulations is discussed in this section. For both the pulling speeds, different injection pressures (P_{inj}), selected in a realistic range, were simulated. Some outcomes, i.e. the pressure profiles along the longitudinal midline in three representative injection cases, are compared in Fig. III.10.

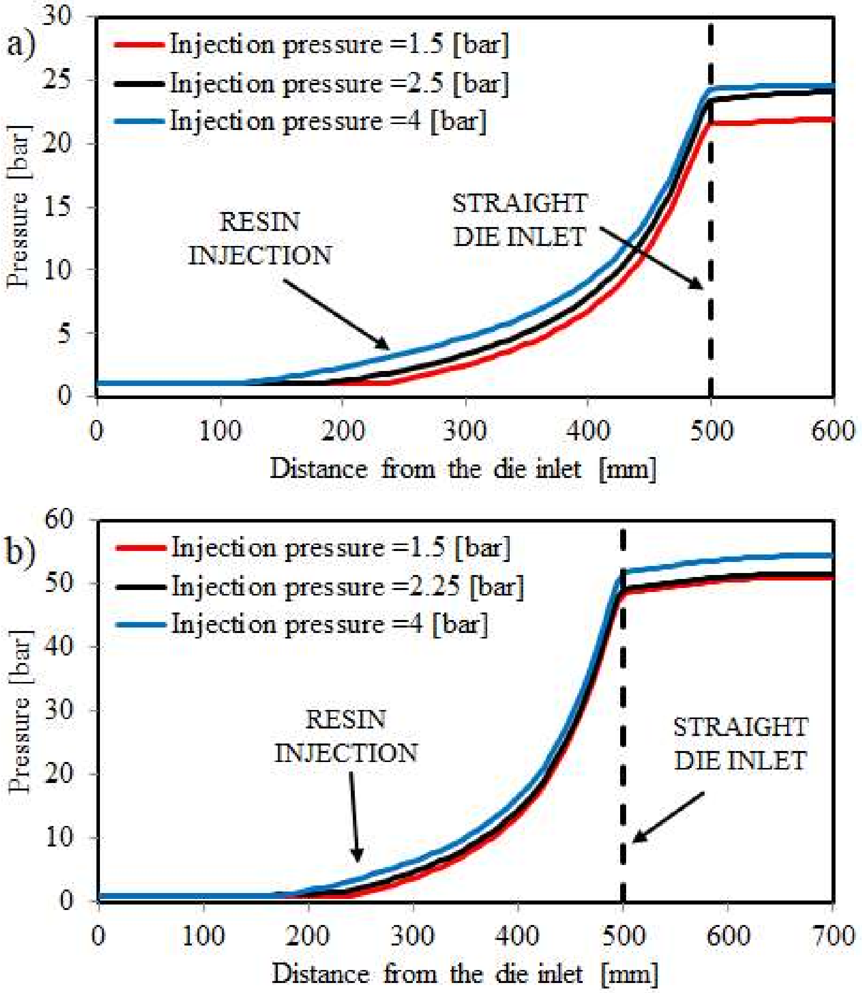

Figure III.10 *Pressure profiles in different injection conditions for pulling speeds of (c) 300 mm/min and (d) 500 mm/min.*

As can be seen, the curves exhibit the same trend in all the simulated scenarios, whereas, in steady state conditions, the fluid pressure increases adopting higher injection pressure. This is easily understandable since higher injection pressure implies higher pressure gradient at the nozzles and therefore a higher amount of resin entering into the domain. Being the resin viscosity major than the air viscosity, higher pressure are required to displace the fluid in the chamber, congruently with the Darcy model. As a result, a more pronounced compression is established into the chamber.

Fig. III.10 shows also that increasing the injection pressure, the pressure curve anticipates its rising, as a direct consequence of the more significant resin backflow. This can be explained again taking into account the Darcy model and the variation of the reinforcement permeability within the chamber. At higher injection pressure implies that more resin enters into the chamber, however, being the amount of resin dragged by the advancing fibers and entering into the die limited by the porosity of the reinforcement, it follows that the pseudo-stationary resin accumulation zone expands toward the chamber inlet. The void fraction was found to decrease when injection pressure increase, as summarized in tab. III.2, congruently with the higher pressure values established in the chamber.

Table III.2 *Void fraction at different injection pressure.*

Injection Pressure [bar]	Pulling speed 300 [mm/s]	Pulling speed 500 [mm/s]
1.50	1.087%	0.245%
2.25	-	0.018%
2.50	0.021%	-
4.00	0.013%	0.005%

Chapter IV
Thermochemical model

IV.1 Thermochemical modeling of cure in pultrusion

The thermochemical evolution of the resin is the core aspect of pultrusion. Indeed the process is based on the "hardening" of the resin while it is crossing the curing-forming die. The energy, necessary to activate the cure reaction is provided by electric resistances, hot oil or steam (Starr, 2000). As described in chapter 2, the cure reaction of thermoset resins is an exothermal process. Therefore, the thermal modeling of the process must account for a heat source term related to the cure reaction. The link between thermal and chemical aspects imposes to adapt a coupled approach to solve this problem (Carlone *et al.*, 2013a; Tucci *et al.*, 2017). Considering a general pultrusion process, in which several different layers i, characterized by different reinforcement materials and/or architectures, the thermal evolution is described by the following energy balance (Eq. (IV.1)) (I Baran, Akkerman and Hattel, 2014):

$$\left(\rho_i c_{p,i}\right)\left(\frac{\partial T}{\partial t}+V_L\frac{\partial T}{\partial x_L}\right)=\sum_j\left(k_{i,j}\frac{\partial^2 T}{\partial x_j^2}\right)+q\ . \tag{IV.1}$$

The subscript j refers to the spatial direction, ρ is the density, c_p is the specific heat, V_L represents the material advancing speed, which is assumed to be equal to the pulling speed. The term $k_{i,j}$is the thermal conductivity of the i-th material layer in the j-th direction. Finally, the term q represents the heat generation rate due to the exothermal cure reaction. The writing of the energy balance within the die material reduces to Eq. (IV.2):

$$\left(\rho_d c_{p,d}\right)\frac{\partial T}{\partial t}=\sum_j\left(k_{d,j}\frac{\partial^2 T}{\partial x_j^2}\right), \tag{IV.2}$$

being the die material unreactive and immobile. In Eq. (IV.2) the subscript d refers to the die. The source term q is expressed by Eq. (IV.3) (Lin Liu, Crouch and Lam, 2000):

$$q=\left(1-V_f\right)\rho_m\,H_T\,\frac{\partial\alpha}{\partial t}\,. \tag{IV.3}$$

The subscript m refers to the polymeric matrix, H_T is the total heat generated in the fully cured resin (Eq. (II.21)). Many authors dealt with the thermochemical problem in pultrusion, proposing different approaches to solve Eq. (IV.2). Early works were based on one-dimensional modeling of the heat equation in the pultrusion of profiles characterized by simple reinforcement architecture (Batch and Macosko, 1987b). Along with the evolution of electronic computational capacity, two-dimensional (R Gorthala, Roux and Vaughan, 1994) and three-dimensional approaches have been presented (Carlone, Palazzo and Pasquino, 2006). Transient and steady-state simulations (Baran, Hattel and Tutum, 2013) have been applied by using numerical techniques such as the finite difference method (Gorthala *et al.*, 1994) and the finite element method (Carlone, Palazzo and Pasquino, 2006).

IV.2 Experimental evaluation of thermochemical behavior in pultrusion

In the present section, two experimental activities of temperature measurement in pultrusion are commented.

IV.2.1 Thermochemical evolution in pultrusion of glass reinforced polyester

E-glass reinforced orthophtalic polyester resin, whose characterization is described in section II.2, has been pultruded using a laboratory-scale pultrusion line (Fig. IV.1).

Figure IV.1 *Laboratory-scale injection pultrusion line.*

The 1090 mm long die is composed of a tapered injection chamber 190 mm long and of a straight cavity 900 mm long. The cavity has a circular cross-section of 6 mm diameter. Three couples of electric platens are fixed on the top and the bottom surfaces of the die. The scope of the platens is to provide to the advancing material the thermal energy necessary to achieve a satisfactory final degree of cure.

Each of the platens covers an area of 280 mm in length and 90 mm in width. The platens are installed on the surface of the die corresponding to the straight cavity. The temperature set point of the plates is defined accounting for the final degree of cure predicted using the kinetic model discussed in section II.2.

The platens power is monitored by J-type thermocouples installed on each of the upper platens, and it is ruled in feedback by an electronic controller (Fig. IV.2). A cooling circuit is milled in the steel die, over and below the die cavity, at a distance of 50 mm in the longitudinal direction from the straight cavity inlet. The cooling system is designed to avoid premature polymerization of the resin, which leads to pultruded defects or system stacking.

The thermal cycle depends also on the pulling speed. The system is moved by a caterpillar pulling system. The pulling speed and the setpoints of the three couples of heating platens are defined, in this experiment, respectively equal to 100 mm/min, 80°C, 110°C and 130°C. Sixteen bundles of E-glass fiber rovings, having a tex number of 2100, have been used in the present experiment, achieving a predicted fiber volume fraction of 53%.

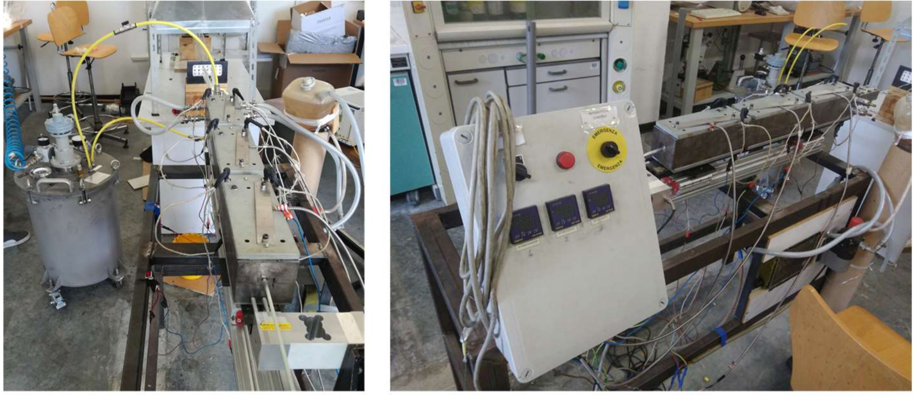

a) b)

Figure IV.2 *a) Thermal platens installed on the die; b) control panel.*

The heat produced by the resistances of the platens diffuses through the die. The temperature cannot physically exhibit discontinuity or punctual drops in all the die volume. Due to this reason, the actual temperature has been evaluated using a k-type wire thermocouple, inserted between heating platens and die surface. The actual temperature profile along the die, compared to the platens set point is reported in Fig. IV.3.

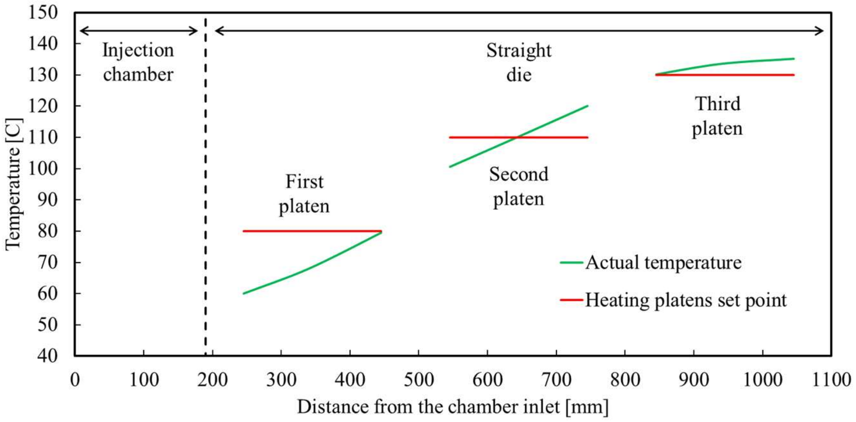

Figure IV.3 *Measured temperature profile between the platens and the die surface.*

It is possible to note that the temperature between the first platen and steel die is initially below the set point. It is worth considering that at 240 mm of distance from the chamber inlet, the cooling fluid flows through the channel milled in the die. The fluid temperature has been evaluated by a k-type wire thermocouple to be averagely equal to 27°C while passing through the milled channel. The measured temperature at the second and the third plates overcomes the set point. The difference is mainly due to the position of the sensitive bulb. Indeed, the thermocouples connected to the controller as a feedback sensor are installed over the platens, in contact with the environment. The k-type thermocouple, used to measure the actual temperature, was set between the die and the platens.

The internal temperature of the material was measured to assess the thermochemical evolution of the resin during pultrusion. Once reached the steady-state condition, a k-type wire thermocouple has been fixed to the advancing fibers, as shown in fig IV.4, to measure the thermal evolution. In order to not alter the test with the presence of the thermocouple wire, and therefore with a lower fraction of resin, the amount of fiber bundles have been reduced, cutting two bundles, which fill the same volume of the thermocouple wire, once compressed.

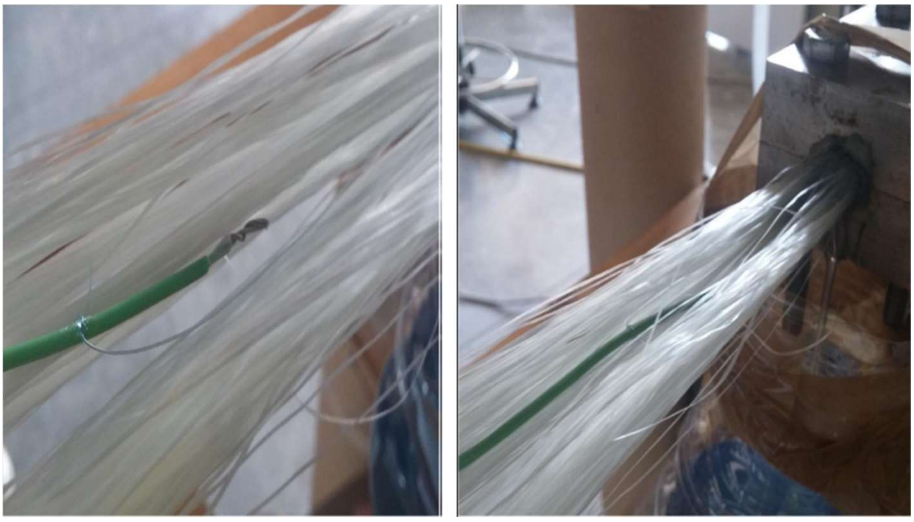

Figure IV.4 *Thermocouple fixing on the advancing fibers.*

IV.2.2 Thermochemical evolution in pultrusion of glass reinforced epoxy

E-glass reinforced epoxy resin (CR141-Sika Biresin®) has been employed to manufacture 60 mm wide and 5 mm tick profiles using the injection pultrusion line equipped at Fraunhofer IGCV of Augsburg (Fig. IV.5). A total of 140 rovings, having tex number of 4900, have been employed to achieve a fiber volume fraction of about 0.70.

Figure IV.5 *Curing-forming injection pultrusion die at Fraunhofer IGCV.*

The 1500 mm long die was composed of a 500 mm long injection chamber, whose geometry is detailed in Fig. III.3, and a 1000 mm long straight cavity. Three pairs of heating platens symmetrically fixed to the top and bottom surfaces of the die and covering the distance from 200 mm to 800 mm from the die inlet imposed the heating energy to the material. The platens have been set at the temperature of 180°C. Two water-cooling plates were fixed to the external surfaces of the steel die at the junction between die and chamber with a contact length of approximately 100 mm. Two pulling speeds, namely 300 mm/min and 500 mm/min, have been investigated. In both cases, the temperature has been measured at the barycenter and on the top surface. The acquired temperature has been referred to the longitudinal coordinate taking into account the pulling speed.

IV.3 Numerical modeling of thermochemical evolution of resin in pultrusion

The numerical model, developed to predict the thermochemical evolution of the advancing material in pultrusion, is based on the experimental test performed using fiber reinforced ortophtalic polyester. For the sake of the reduction of computational effort and time, one-quarter of the system has been modeled, applying symmetry conditions on the cut-sections. The modeled geometry has been discretized using hexahedral brick elements. Fig. IV.6 depicts the geometry of the simulated domain.

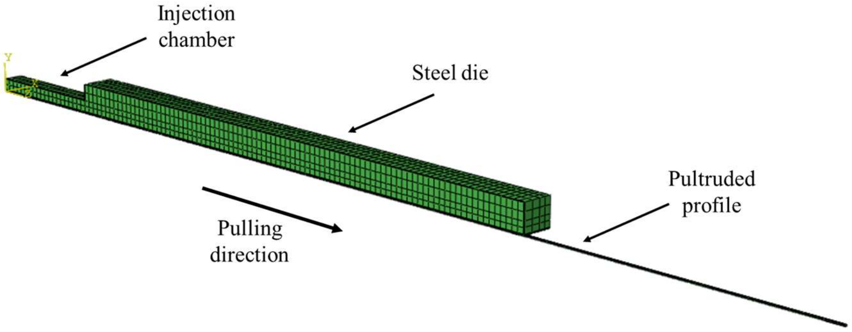

Figure IV.6 *Computational domain of the thermochemical problem.*

The pultrusion can be assumed as a stationary process. Therefore, the cure rate expression can be rewritten in an Eulerian frame of reference (Baran *et al.*, 2013). The cure kinetic function $R_m(\alpha,T)$, whose characterization is described in section (II.2), is assumed proportional to the heat flow rate (Monti *et al.*, 2011). Assuming that the modeled problem is stationary, the cure kinetic function $R_m(\alpha,T)$ is expressed as follows:

$$R_m(\alpha,T) = \frac{d\alpha}{dt} = \frac{\partial\alpha}{\partial t} + \frac{\partial\alpha}{\partial x_L}\frac{\partial x_L}{\partial t} = \frac{\partial\alpha}{\partial t} + V_L\frac{\partial\alpha}{\partial x_L}\,. \qquad \text{(IV.4)}$$

In Eq. (IV.4) V_L is the speed of the material in the longitudinal direction. The other components of speed are assumed null. This speed is equal to the pulling speed of the system. Eq. (IV.4) can be rewritten in the following form:

$$\frac{\partial \alpha}{\partial t} = R_m(\alpha, T) - V_L \frac{\partial \alpha}{\partial x_L}. \qquad \text{(IV.5)}$$

Involving the Eq. (IV.5) in the Eqs. (IV.1) and (IV.3), the heat flow problem is defined in the space domain, and, therefore, does not involve the time variable. The position and the numbering of the profile nodes is a critical issue to solve the problem. Indeed, the presence of the degree of cure gradients requires precise knowledge of the node position. Therefore, the discretization of the domain has been coded, in order to have a regular mesh. Considering one-quarter of the pultruded profile cross-section, it has been discretized in 20 quadrangles. The position of the 25 nodes is represented in fig. 4.7. The longitudinal space increment has been modeled equal to 5 mm.

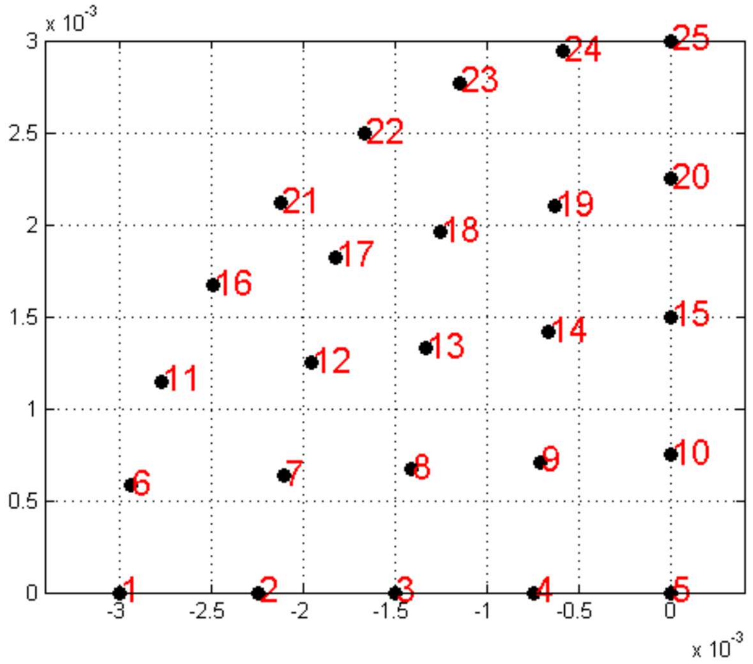

Figure IV.7 *Position and numbering of the nodes in the profile cross-section.*

The injection chamber and the steel die are unreactive (Eq. (IV.2)). Therefore, the discretization of those regions is made using coarser mesh.

Fig IV.8 shows a detailed view of the injection chamber and of the profile cross-section model.

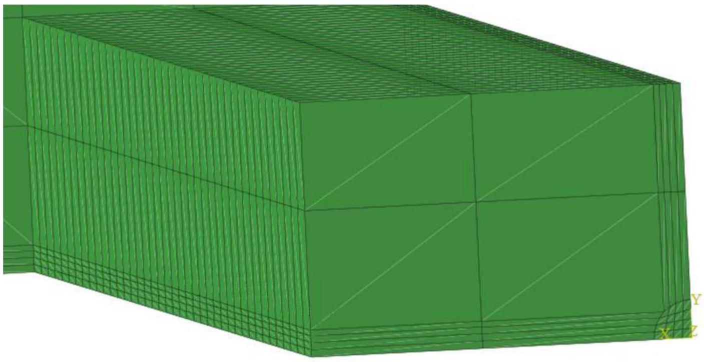

Figure IV.8 *Detailed view of the injection chamber and of the profile cross-section model.*

The discretized geometry has been implemented using the ABAQUS suite. The following boundary conditions have been defined to close the problem:

- Symmetry conditions on the symmetry surfaces. Considering x_{sym} the direction normal to the symmetry plane, they can be expressed as follows:

$$\frac{dT}{dx_1} = 0\,, \tag{IV.6}$$

$$\frac{d\alpha}{dx_2} = 0\,; \tag{IV.7}$$

- Imposed temperature at the platens surfaces, in agreement with the experimental measurement of Fig. IV.3;
- Degree of cure of the profile elements (Fig. IV.9) null at the injection chamber inlet and environmental temperature (25°C);
- Imposed temperature of 27°C at the cooling channel nodes (Fig. IV.10);
- Natural convection at all the externally exposed surfaces (Fig. IV.11), considering the environmental temperature equal to 25°C.

It is worth to mention that it was assumed continuity of the material in the entire domain. It means that in this simulation eventual detachment between die and profiles (Safonov and Konstantinov, 2015) has been neglected.

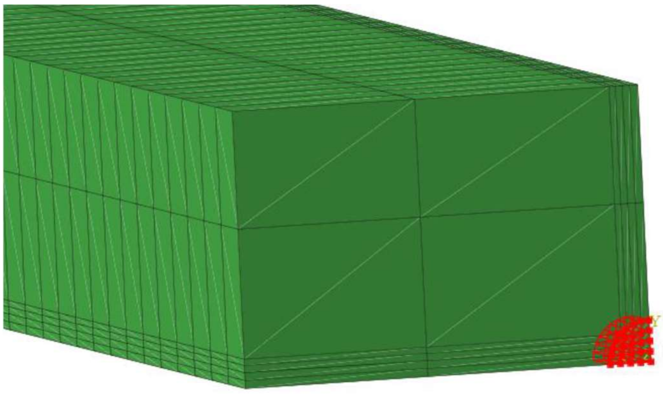

Figure IV.9 *Highlighted profile elements at the injection chamber inlet.*

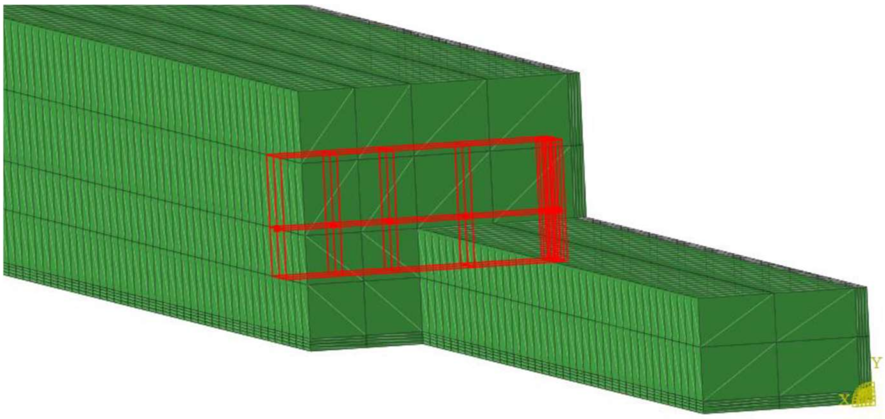

Figure IV.10 *Highlighted elements corresponding to the cooling channel.*

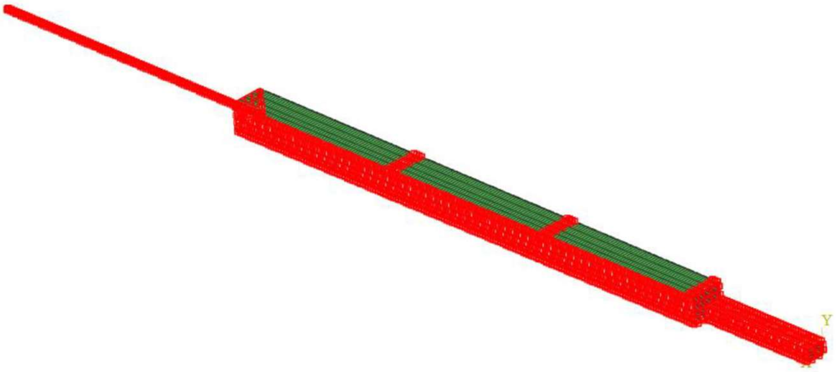

Figure IV.11 *Highlighted externally exposed surfaces.*

IV.4 Comparison between experimental and numerical results

Fig. IV.12 compares the experimentally measured temperature to the main numerical results, relatively to the pultrusion of a circular profile made of E-glass reinforced ortophtalic polyester.

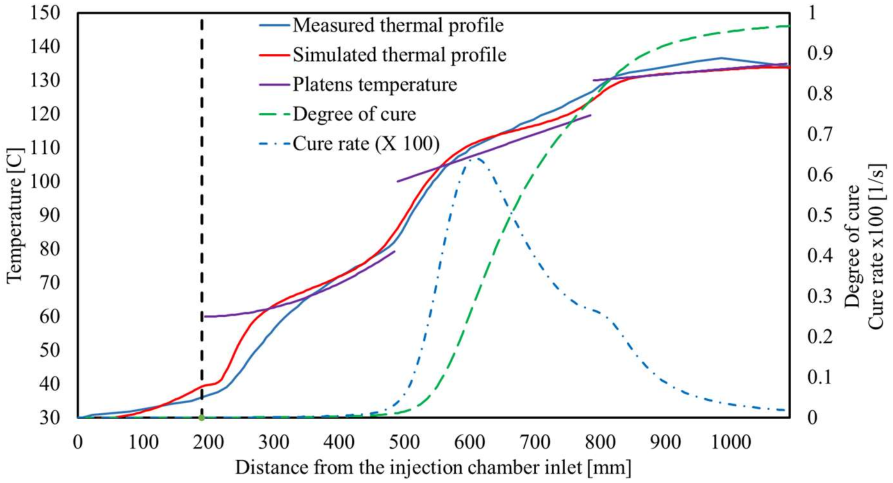

Figure IV.12 *Temperature and cure behaviors in pultrusion.*

The numerical profiles plotted in Fig. IV.12 refers to the barycenter of the pultruded cross-section (node 5 of Fig. IV.7). Upon the cooling channel (in the earliest 240 mm), the material exhibits a slight rise in temperature. Indeed, the cooling fluid absorbs the thermal energy and thwarts the heat diffusion towards the injection chamber. Downstream the cooling system, the profile temperature rises up to the platens temperature. At 450 mm the cure reaction starts: the cure rate curve sharply starts rising and shows a peak at 600 mm. At the same position, the temperature of the profile overcomes the platen temperature. Indeed, since the cure rate is proportional to the exothermal energy produced by the resin, at this coordinate the thermal field is modified by the heat source q of Eq. (IV.1). Downstream the peak, cure rate decreases and, therefore, the exothermal heat produce a lower amount of energy. At the last 300 mm of the die, the temperature difference between profile and platens is negligible. The predicted degree of cure at the end of the process is 96%. In Fig. IV.12, the good agreement between numerical and experimental profile can be appreciated.

The behaviors just described, can be better appreciated analyzing the temperature results acquired in during the pultrusion process of glass reinforced epoxy, reported in Fig. IV.13. Indeed, in this case, the cross-section was about 8 times larger, if compared to the pultrusion of polyester. Due to this difference, the exothermal energy, proportional to the amount of resin, produce a sharper temperature difference.

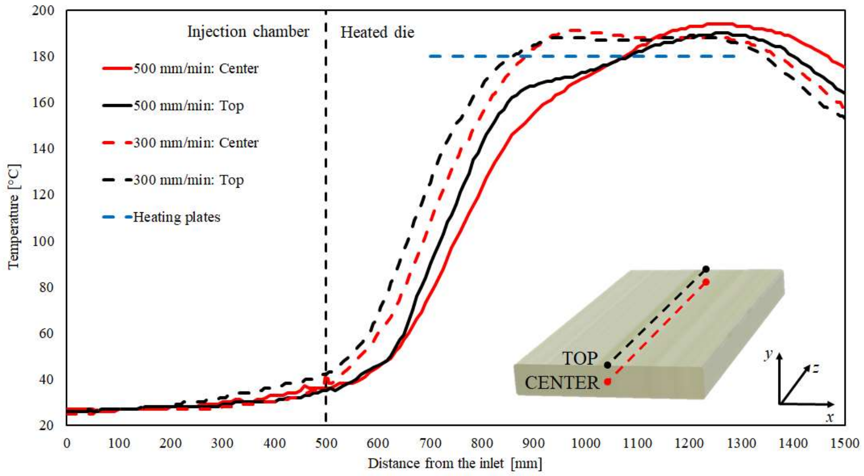

Figure IV.13 *Acquired temperature profiles along central and top paths.*

Also in this case, the cooling plates absorbed the heat flow, avoiding excessive heating of the earliest 600 mm. The temperature has been evaluated at the periphery and at the core. The temperature is initially higher at the external surface, if compared to the material core. Indeed, the heat flows from the platens to the core of the material. At the activation of the cure reaction, the flow direction is inverted, going from the barycenter of the section toward the periphery and the die.

The pulling speed directly influences the thermal cycle experienced by the resin. In this case, being a detailed characterization of the cure kinetics unavailable, it is not possible to analyze the data with the support of the predicted cure and cure rate. Nevertheless, the delay of rising ramps and of crossover in the faster case can be clearly detected in Fig. IV.13. The differences due to different pulling speed are discussed in more details in section (IV.5).

IV.5 Influence of the process parameters

The thermochemical model previously described has been applied to evaluate the cure evolution and the thermal profile in case of different process parameters. Five different pulling speeds, namely 80 mm/min, 120 mm/min, 160 mm/min, 200 mm/min and 240 mm/min, have been considered in these simulations, keeping the other boundary conditions unaltered. In Figs. IV.14 and IV.15, the predicted thermochemical behaviors in time and in space are reported.

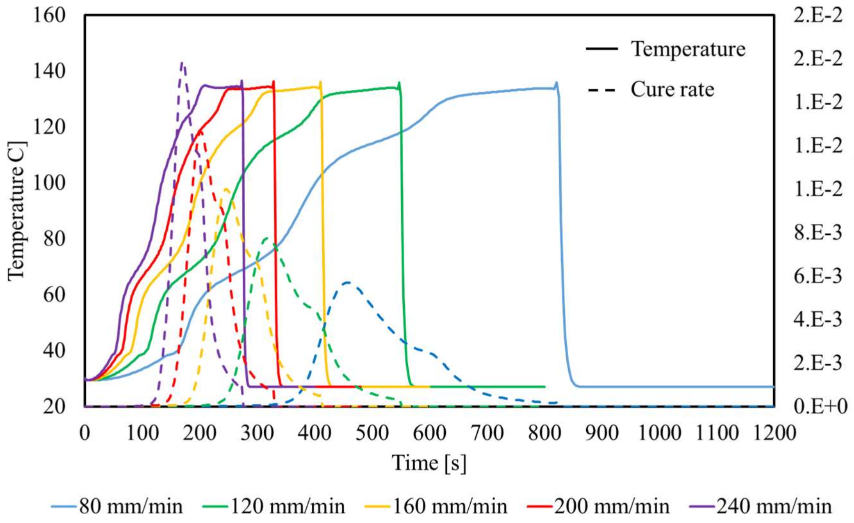

Figure IV.14 *Predicted thermochemical evolution with respect to the time.*

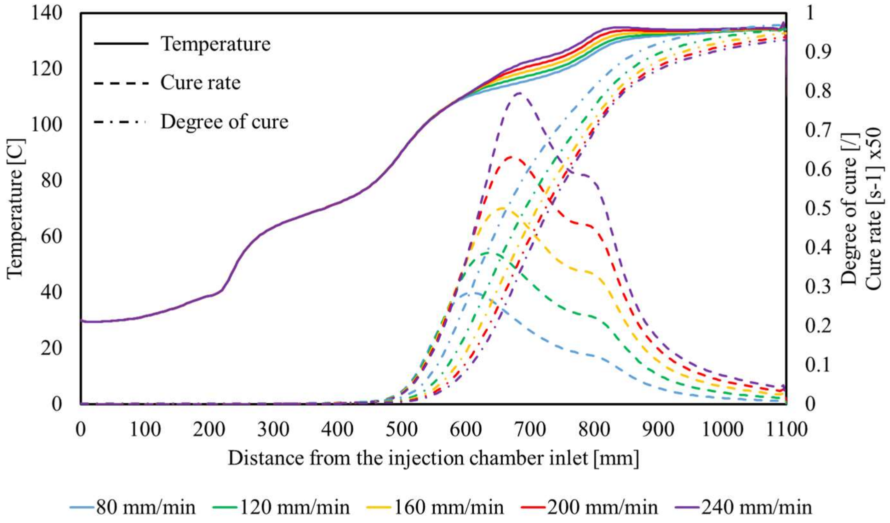

Figure IV.15 *Predicted thermochemical evolution with respect to the position.*

The heating-curing cycle is as fast as higher is the pulling speed. Therefore, as higher the pulling speed is, as thinner the cure rate peak in time results (Fig. IV.14). Nevertheless, due to the kinetic behavior described in section (II.2), faster heating ramps provoke higher exothermal flows. The heat flow produced due to the cure is proportional to the reaction rate. Due to this reason, the cure rate peak is decreases as the pulling speed is lower. The profiles reported in Fig. IV.15 allow one to punctually compare the performance of the process with different advancing speeds. In every cases, the polymerization of the resin is activated at 450 mm of distance from the chamber inlet. At the activation, the cure rate curves increase with the same slopes. As previously discussed, in the faster cases the cure rate reaches higher peaks. The peak of cure rate, being related to the exothermal flow, influence the temperature profile. Indeed, upon the resin activation the thermal curves overlie. The higher cure rate provokes a major increase of temperature. Therefore, the temperature profiles between the positions 600 mm and 1000 mm, presents higher values for faster pulling velocities.

It is worth to note that the degree of cure result closer to the unit (completion of the cure reaction) in the slowest case. Indeed, the cure is the integral in time of the cure rate. Analyzing Fig. IV.14, it is clear that the cure rate curve subtend a larger area, even if the peak is remarkably lower. Therefore, in the simulated process, the lower the pulling speed is, the better the degree of cure at the die outlet results.

In order to assess the influence of the thermal cycle on the performances of the process, the two alternative thermal cycles, depicted in Fig. IV.16, have been simulated. The pulling speed in this computation is set equal to 160 mm/min.

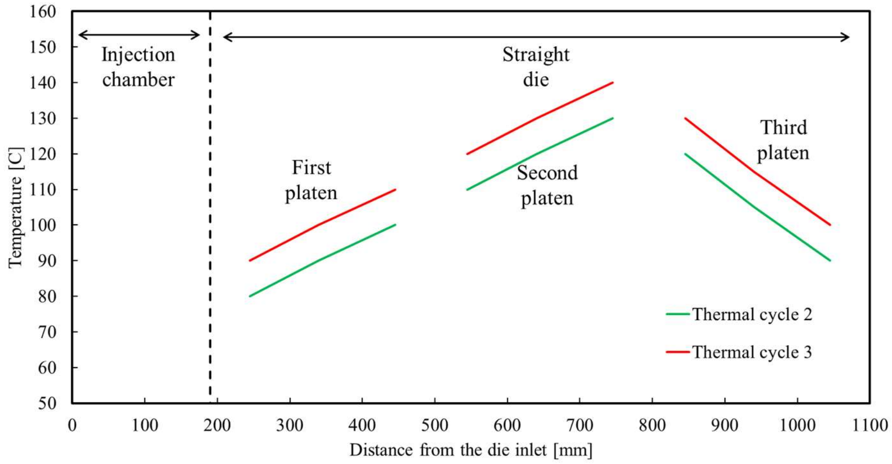

Figure IV.16 *Alternative thermal cycles simulated.*

In Fig. IV.17 the temperature, degree of cure and reaction rate profiles predicted in the two alternative thermal cycles are compared to the ones relative to the pultrusion simulation at 160 mm/min (Thermal cycle 1) discussed in section IV.4 (Fig. IV.3).

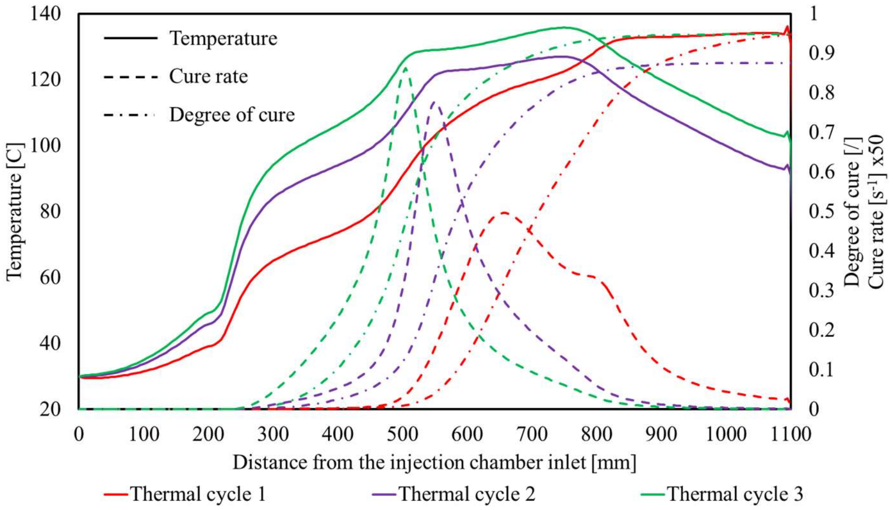

Figure IV.17 *Thermochemical behavior with alternative thermal cycles.*

The two alternative cycles, differently from the thermal cycle 1, present a decreasing imposed temperature in the last sector. Therefore, at the die outlet, the profiles experience a lower temperature drop, and, consequently, a slighter thermal stress. The two alternative cycles, initially provide higher thermal energy, compared to the experimental one. Indeed, their temperature profiles, in agreement with the thermal levels imposed, presents values remarkably higher in the first two sectors. Due to this reason, the cure rate curves present sharper and anticipated peaks. The peaks in the two alternative cases are thinner and higher. The final degree of cure in the thermal cycle 2 presents a remarkably low value (87%), evidencing that, in this case, the energy provided during the process is not enough to produce a satisfactory cure reaction. Differently, the thermal cycle 3 leads to a final degree of cure of the resin of the 95%: equal to the one achieved using the experimental thermal cycle. Moreover, in the cycle 3, the cure reaction is anticipated, reducing the portion of the die occupied by liquid resin. The advantages related to an anticipated reaction peak and to the lower thermal stress at the outlet regards the final mechanical properties of the profile, and are discussed in chapter V.

Chapter V
Mechanical model

V.1 Numerical modeling of stress-strain field in pultrusion

Stress-strain distribution in pultrusion is influenced by the mechanical properties, temperature gradients, chemical shrinkage and die-material interaction (Bogetti and Gillespie, 1992). In general, the vector of the total strain increment $\dot{\varepsilon}_{tot}$ is expressed considering the mechanical strain $\dot{\varepsilon}_{mech}$, the thermal strain $\dot{\varepsilon}_{th}$ and the chemical strain $\dot{\varepsilon}_{ch}$, as in Eq. (V.1) (Boisse, 2015):

$$\dot{\varepsilon}_{tot} = \dot{\varepsilon}_{mech} + \dot{\varepsilon}_{th} + \dot{\varepsilon}_{ch}\ , \tag{V.1}$$

Section II.1 discusses the evaluation of the mechanical properties of the composite material, based on volume fractions, reinforcement architecture and thermochemical history of the resin. Assuming a transversally isotropic profile, the stress increment vectors are related to the mechanical strain increments by the Jacobian matrix J, as described by Eqs. (V.2) and (V.3) (Boisse, 2015):

$$\dot{\sigma}_{mech} = \begin{bmatrix} \dot{\sigma}_L \\ \dot{\sigma}_{T1} \\ \dot{\sigma}_{T2} \\ \dot{\tau}_{LT} \end{bmatrix}_{mech} = J\ \dot{\varepsilon}_{mech} = J \begin{bmatrix} \dot{\varepsilon}_L \\ \dot{\varepsilon}_{T1} \\ \dot{\varepsilon}_{T2} \\ \dot{\gamma}_{LT} \end{bmatrix}_{mech} , \tag{V.2}$$

$$J = \begin{bmatrix} \frac{1-\nu_{TT}^2}{E_T^2\,\Delta} & \frac{\nu_{LT}(1+\nu_{TT})}{E_T^2\,\Delta} & \frac{\nu_{LT}(1+\nu_{TT})}{E_T^2\,\Delta} & 0 \\ \frac{\nu_{LT}(1+\nu_{TT})}{E_L\,E_T\,\Delta} & \frac{1-\nu_{LT}^2}{E_L\,E_T\,\Delta} & \frac{\nu_{TT}+\nu_{LT}^2}{E_L\,E_T\,\Delta} & 0 \\ \frac{\nu_{LT}(1+\nu_{TT})}{E_L\,E_T\,\Delta} & \frac{\nu_{TT}+\nu_{LT}^2}{E_L\,E_T\,\Delta} & \frac{1-\nu_{LT}^2}{E_L\,E_T\,\Delta} & 0 \\ 0 & 0 & 0 & 2\,G_{LT} \end{bmatrix} . \tag{V.3}$$

In the Jacobian matrix J, the parameters E_L, E_T, G_{LT}, ν_{LT} and ν_{TT} are defined in section II.1, while Δ is defined as reported in Eq. (V.4):

$$\Delta = \frac{1-2\,\nu_{LT}^2 - \nu_{TT}^2 - 2\,\nu_{LT}^2 \nu_{TT}}{E_L\, E_T^2}\ . \tag{V.4}$$

The thermal strain increment $\dot{\varepsilon}_{th}$ depends on the coefficient of thermal expansion CTE. Considering the j-th direction, the thermal strain is expressed as follows:

$$\dot{\varepsilon}_{th,j} = CTE_j\, \Delta T\ . \tag{V.5}$$

Considering composite layers reinforced by unidirectional rovings, the thermal expansion in longitudinal and transversal direction can be expressed by the following expressions (Bogetti and Gillespie, 1992):

$$\mathrm{CTE}_L = \frac{CTE_{L,f}\, E_{L,f}\, V_f + C \quad {}_m\, E_m\, V_m}{E_{L,f}\, V_f + E_{L,m}\, V_m}\ , \tag{V.6}$$

$$\mathrm{CTE}_T = \left(CTE_{T,f} + \nu_{LT,f} CTE_{L,f}\right)V_f + CTE_m(1 + \upsilon_m)V_m - \left(\nu_{LT,f}V_f + \nu_m V_m\right)CTE_L\ . \tag{V.7}$$

The subscripts m and f refers respectively to the resin matrix and the fiber phase. Considering a quasi-isotropic mat reinforced layer, the evaluation of the coefficient of thermal expansion is based on the properties (Eqs. (II.1) to (II.9), (V.6) and (V.7)) of a roving layer presenting the same fiber volume fraction (Akkerman, 2002):

$$\mathrm{CTE}_{IP} = \frac{(E_L + \nu_{LT} E_T) CTE_L + (1 + \nu_{LT}) E_T CTE_T}{E_1 + (1 + 2\,\nu_{LT})\, E_T}\ , \tag{V.8}$$

$$\mathrm{CTE}_{OP} = \frac{(\nu_{LT} E_T - \nu_{TT} E_L)\mathrm{CTE}_L + \left((1 + \nu_{TT}) E_L + (1 + \nu_{LT}) E_T\right) CTE_T}{E_1 + (1 + 2\,\nu_{LT})\, E_T}\ . \tag{V.9}$$

During the cure reaction, the thermoset polymers exhibit a contraction in volume, known as chemical shrinkage (Nawab *et al.*, 2013). The deformations related to this behavior are accounted by the chemical strain increment $\dot{\varepsilon}_{ch}$. The chemical shrinkage of the resin $\dot{\varepsilon}_{ch,m}$ is modelled accounting for the increments in volume shrinkage ΔV_{sh} as a function of the degree of cure increment $\Delta\alpha$, as described in Eq. (V.10) (Bogetti and Gillespie, 1992):

$$\dot{\varepsilon}_{ch,m} = \sqrt[3]{1 + \Delta\alpha\, \Delta V_{sh}} - 1\ . \tag{V.10}$$

The value of the volume shrinkage increment ΔV_{sh} is a characteristic of the resin system. According to the self-consistent field micromechanics (SCFM), the chemical shrinkage of a unidirectional roving reinforced composite in longitudinal and transversal directions is expressed by the following relations:

$$\dot{\varepsilon}_{ch,L} = \frac{\dot{\varepsilon}_{ch,m} E_m V_m}{E_{L,f} V_f + E_m V_m}\ , \tag{V.11}$$

$$\dot{\varepsilon}_{ch,T} = \dot{\varepsilon}_{ch,m} V_m (1 + \nu_m) - \dot{\varepsilon}_{ch,L}\left(\nu_f V_f + \nu_m V_m\right). \tag{V.12}$$

As in the evaluation of all the other properties of a quasi-isotropic mat reinforced composite element, the chemical strain increment is predicted accounting for the properties fictitious composite reinforced by unidirectional rovings, having the same volume fractions of the mat-reinforced element (Akkerman, 2002):

$$\dot{\varepsilon}_{ch,IP} = \frac{(E_L+\nu_{LT}E_T)\dot{\varepsilon}_{ch,L}+(1+\nu_{LT})E_T\dot{\varepsilon}_{ch,T}}{E_L+(1+2\,\nu_{LT})E_T} \ , \qquad \text{(V.13)}$$

$$\dot{\varepsilon}_{ch,OP} = \frac{(\nu_{LT}E_T-\nu_{TT}E_L)\dot{\varepsilon}_{ch,L}+\big((1+\nu_{TT})E_L+(1+\nu_{LT})E_T\big)\dot{\varepsilon}_{ch,T}}{E_L+(1+2\,\nu_{LT})E_T} \ . \qquad \text{(V.14)}$$

V.2 Pulling force analysis

The pulling systems typically used in pultrusion processes are controlled in speed. It means that the pulling force can increase or decrease to overcome the resistant loads arising along the pultrusion line. The resistance forces are typically classified in either collimation forces F_{coll}, bulk compaction F_{bulk}, viscous drag F_{vis} or friction forces F_{fric} (Batch and Macosko, 1990). The pulling force F_{pull} necessary to overcome the resistances opposed by the pultrusion system is the sum of the single contributes (Batch and Macosko, 1990):

$$F_{pull} = F_{coll} + F_{bulk} + F_{vis} + F_{fric} \ . \qquad \text{(V.15)}$$

The collimation forces arise upstream the curing forming die, due to the interaction between the dry fibers and the guiding plates. This resistant term depends mostly on the arrangement of the fiber in the creel rack and on the position and the geometry of the guiding plates. Nevertheless, this term typically is negligible (Price and Cupschalk, 1984).

The bulk compaction forces arise in the tapered injection chamber, due to the constraining of the impregnated reinforcement in a narrow space (Price and Cupschalk, 1984). In this region, the resin is still completely uncured, and, therefore, in the liquid state. Being an uncompressible medium forced in decreasing volume, the pressure remarkably rises, as described in section III.5. Considering the taper angle θ, the local pressure p and the contact area A_1, the bulk compaction force is expressed as follows (Batch and Macosko, 1987a):

$$F_{bulk} = \iint_{A_1} p \sin\theta \ dA_1 \ . \qquad \text{(V.16)}$$

The viscous drag occurs at the interface between the advancing wet reinforcement and the cavity wall. In particular, this behavior regards the zone in which the resin polymerization is not yet activated and the resin behaves as a viscous liquid medium. The viscous drag acts from the chamber inlet up to the cure activation point, where the resin viscosity sharply increases, as described in chapter III. The force related to this behavior can be evaluated considering the resin flow between fibers and die as a Couette flow (Kim *et* *al.*, 1997). Considering a resin layer having viscosity $\eta(\alpha, T)$, thickness λ_{th} and a contact area A_2, the value of F_{vis} is computed by the Eq. (V.17):

$$F_{vis} = \frac{V_L}{\lambda_{th}} \iint_{A_2} \eta(\alpha, T)\, dA_2 \ . \tag{V.17}$$

Many authors dealt with the estimation of the thickness λ_{th} (Bibbo and Gutowski, 1986; Åstroöm and Pipes, 1993). Taking into account the two possible fiber-packing configurations (Fig. III.2) and the possible direct contact between the fibers and the die, the layer thickness in quadratic arrangement (Eq. (V.18)) and in hexagonal arrangement (Eq. (V.19)) are evaluated as follows:

$$\lambda_{th} = R_f \left(\sqrt{\frac{\pi}{V_f}} - 2 \right) , \tag{V.18}$$

$$\lambda_{th} = R_f \left(1 - \frac{1}{2} \sqrt{\frac{\sqrt{3}\pi V_f}{2}} \right) . \tag{V.19}$$

In eqs. (V.18) and (V.19) R_f represents the fiber radius.

The friction force arise at the interface between the mostly cured profile and the walls of the die cavity (Carlone *et al.*, 2013b). This interaction is influenced by the thermal expansion, which increases the contact pressure between the advancing material and the die cavity, and by the chemical shrinkage, which promotes the decrease of the contact pressure P_{con}. Whereas the chemical shrinkage induces the detachment of the profile, no friction resistance opposes to the pull (Alexander A. Safonov, Carlone and Akhatov, 2018). Being μ the friction coefficient and A_3 the contact area, the friction force is defined as follows:

$$F_{fric} = \iint_{A_3} \mu\, P_{con}\, dA_3 \ . \tag{V.20}$$

V.3 Experimental evaluation of the pulling force in pultrusion

V.3.1 Measurement of the pulling force

The experimental tests were conducted using a laboratory scale injection pultrusion system. The pultrusion line used in the present experimental analysis is depicted in Fig. IV.1. The curing-forming tool is composed of a tapered injection chamber 190 mm long, bolted on the heating die, presenting a 900 mm long straight cavity. The employed resin system is based on the ortophtalic polyester system characterized in section II.2. The reinforcement is constituted by 18 rovings of E-glass (tex number 2400). According to the shape of the cavity, the nominal diameter of the pultruded profile is 6 mm. Taking into account the amount of reinforcement involved and the cross-section of the produced FRP, the fiber volume fraction is expected to be equal to 59%.

The injection system (Fig. V.1 (a)) drives the uncured liquid resin toward a tapered chamber (Fig. V.1 (b)), converging to the die geometry.

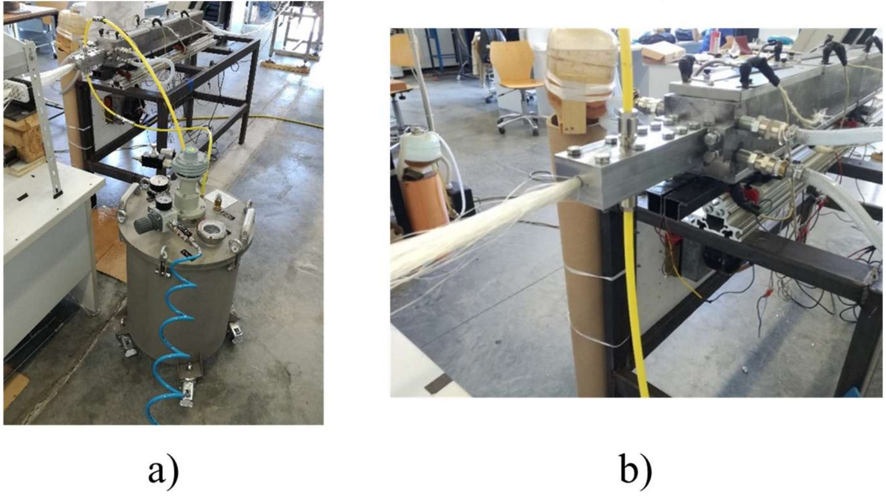
a) b)

Figure V.1 *a) Resin pressurized tank; b) injection chamber.*

Within the tapered cavity, the resin impregnates the advancing fibrous reinforcement. Three pairs of thermo-electric heating plates are mechanically fixed on the die top and bottom surfaces. Each couple of heaters is monitored and controlled in temperature using J-type thermocouples and a regulation system. The temperatures of the first, the second and the third couples of heating plates are respectively set equal to 80°C, 110°C and 130°C, in order to provide to the polymeric resin the thermal cycle necessary to achieve a satisfactory cure. Each of the thermal plates covers a rectangular surface 280 mm long and 90 mm wide. A cooling system prevents the increase of the temperature at the entrance of the die, and, therefore, of the advancing material in the earliest region of the straight cavity. The purpose of the cooling system is to avoid premature local polymerizations which can lead to defects or, in the worst case, to the stacking of the material in the die and, as a consequence, the interruption of the continue production. The advancing velocity was controlled by a caterpillar located at the end of the line. In the present work, two pulling speeds were investigated, namely 100 mm/min and 200 mm/min.

During the process, the temperature of the advancing material has been measured using a K-type travelling thermocouple, adhesively connected to the advancing fibers. The position of the bulb has been evaluated taking into account the velocity of the process. The cure kinetic and the rheological behavior of this resin system is described in chapter II.

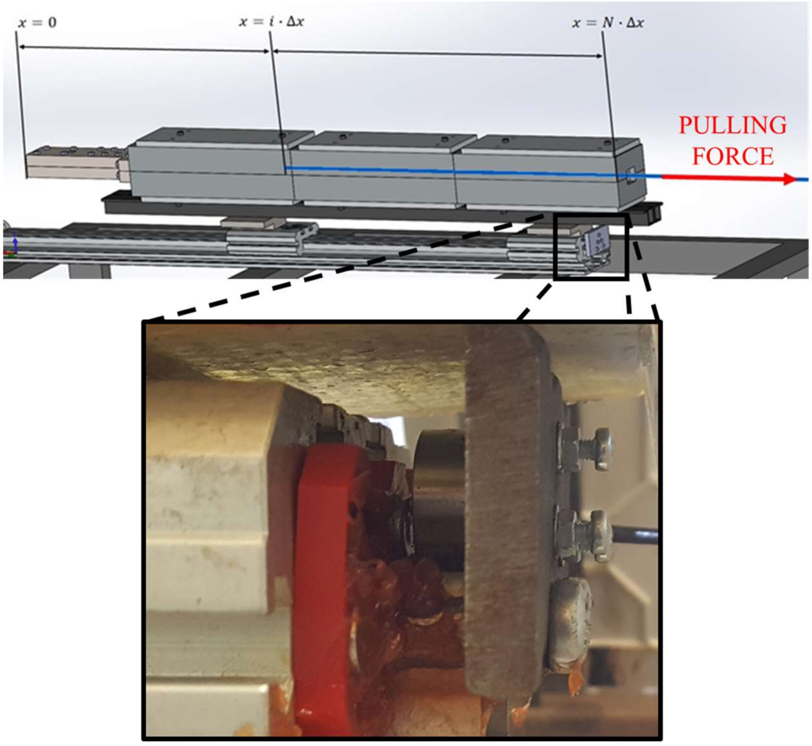

Figure V.2 *Pulling force measuring system.*

Fig. V.2 describes the system implemented to measure the force along the pulling direction and opposing the movement of the workpiece. The die, free to slide on a longitudinal guide impact on a load cell fixed on the limit of the guide. The load cell is a compressive button connected to a signal amplifier and an *ArduinoUno* board, connected to a computer and interrogated by a code implemented using the *LabView* suite.

The load cell has been calibrated before each performed tests, using blocks of known weight, connected to the die using an opportune system of wire and pulley.

Due to the system setting and disposition, during the stationary pultrusion process, the load cell acquires the resistant force produced by the contact between the advancing composite and the whole cavity. In order to measure the profile of the resistance to the pull $F(x)$ along the cavity, during a stationary stable pultrusion process, the advancing fiber were cut before entering in the inlet of the injection chamber. Using this technique, the load cell detects the value of the total resistance $Q_{force}(x)$, arising between the position of the advancing cut section $x_c(t)$ and the die outlet x_{out}, as described in Eq. (V.21) (Tucci *et al.*, 2019):

$$Q_{force}(x) = \int_{x_c(t)}^{x_{out}} F(x)\, dx \,. \tag{V.21}$$

Therefore, the local force $F(x)$ can be estimated as follows:

$$F(x) = -\frac{dQ_{force}(x)}{dx}. \tag{V.22}$$

The position of the cut section $x_c(t)$ is computed accounting for the pulling speed v_{pull} and for the time delay from the cutting instant t_c, as described in eq. (V.23):

$$x_c(t) = v_{pull}(t - t_c). \tag{V.23}$$

V.3.2 Evaluation of the strain by optical fiber Bragg gratings

The strain evolution during cure has been evaluated by optical sensors based on fiber Bragg gratings (FBG). This technology allows one to detect temperature variations and deformation at the same time. FBG sensor, when excited by an optical signal, absorbs part of the light specter depending on the values of temperature and deformation (Lee, 2003). The transmission of the signal occur by means of thin optical fibers, therefore the encumbrance of the sensors is negligible with respect to the dimension of the produced parts.

FBG sensors have been used to evaluate the strain evolution in the pultrusion system earlier described. Commercial optical FBG chain (DTG®-LBL-1550-F), composed of three sensitive parts, was modified to detect at the same time both temperature and deformation variations. This kind of sensors respond to a variation in temperature or in strain, with a displacement of the peak in the reflected wavelength specter (Aashia *et al.*, 2010). FBGs were modified in order to make independent the behavior of the characteristic equations. Therefore, a recalibration of each of them was necessary. The general characteristic equation of the sensor is the following:

$$\ln\left(\frac{\lambda}{\lambda_0}\right) = C_T\,\Delta T + C_\varepsilon\,\Delta\varepsilon\,. \tag{V.23}$$

The variation of the wavelength detected λ from the wavelength of reference λ_0 of the sensor depends from the the variations in thermal and mechanical fields taking moltiplicative calibration coefficient C_T and C_ε into account. While C_T is a real costant value, the coefficient C_ε has the following expression:

$$C_\varepsilon = a_\varepsilon\,ln(\Delta\mathrm{T}) + b_\varepsilon\,, \tag{V.23}$$

where a and b are two more calibration constant coefficient.

The optical fiber interacts with an optical sensor interrogator (NI PXIe-4844).

Its tasks is to excite the fiber with a complete specter signal, read the reflected signal and compute the specter absorbed by the three FBG.

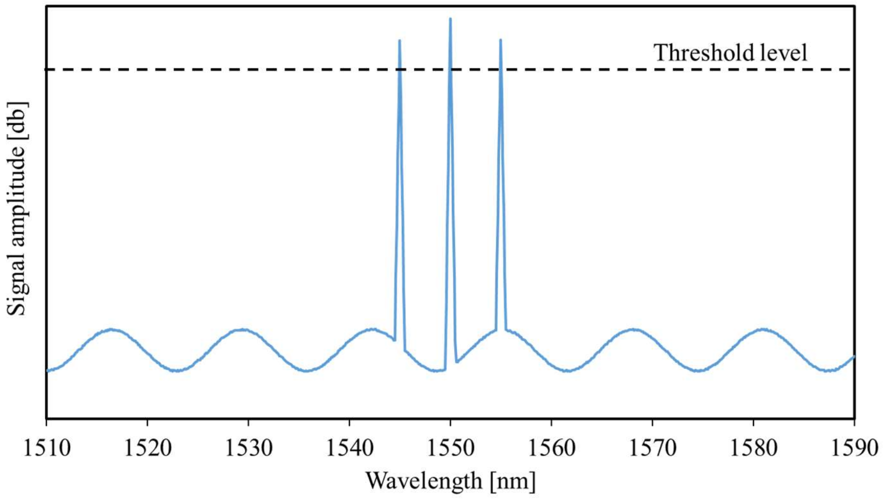

Figure V.3 *Absorbed specter by FBGs sensors.*

Fig. V.3 shows a thipical specter of the wavelength absorbed by the optical fiber. The specter presents three different peacks relative to the absorbtion of signal of each of the FBG sensor. The FBGs of the optical fiber employed in this work are set to absorbe respectively wavelength in the neighbourhood of 1545, 1550 and 1555 nm. Sensitive segments position along the optical fiber is shown in Fig. V.4.

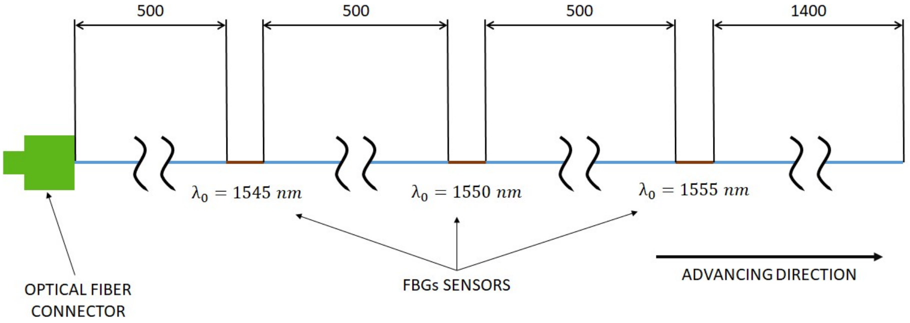

Figure V.4 *Positions of the FBGs sensors along the optical fiber (lengths in mm).*

The optical fiber free extremity was hooked to the advancing reinforcement, in such a way to be as close as possible to the barycentral line of the pultruded profile. The sensitive segments have a length of 30 mm. The position of the first FBG sensor (FBG1), too close to the connector to the interrogator, allow it to explore just a short portion of the die cavity. For this reason only the data provided by the second (FBG2) and the third (FBG3) sensitive gratings were taken into account. The second sensitive segments, relative to the wavelength of 1550, was englobed in a nickel capillary in order to tune the response to the external loads. This modification influenced the grating properties and therefore a the ricalibration was necessary in order to find the values of parameters C_T, a and b of eqs. (5.24) and (5.25) for each of the FBG sensors. This task was achieved imposing to the fiber thermal ramps or mechanical loads and evaluating the values of wavelength reflected. Tab. V.1 reports the values of the characteristic parameters of the FBG.

Table V.1 *Calibration parameters of the FBGs*

Symbol	FBG2	FBG3
λ_0	1550	1555
C_T	1.6391E-5	7.3839E-6
a_ε	1.8038E-9	3.0087E-8
b_ε	3.0021E-9	5.6203E-7

The fiber was used to measure temperature and deformation profile in a laboratory scale IP process producing glass fiber reinforced unsaturated polyester profiles of circular cross-section, having a radius of 3 mm. The injection chamber is a 190 mm long tapered cavity converging with a taper angle of about 2°, having two injection nozzles at 70 mm of distance from the entrance of the chamber disposed at the top and the bottom side of the cavity.

The imposed temperatures were chosen considering the polymerization reaction kinetics described in chapter II. Thermal level of the three couples of platens, of 80°C, 110°C and 130°C respectively, was ruled by a control system. The caterpillar pulling system imposed to the material the advancing speed of 100 mm/min.

V.4 Numerical modeling

This section presents a three-dimensional numerical mechanical model of the pultrusion of E-glass reinforced ortophtalic polyester, described in section V.3. The model accounts for the thermochemical evolution of the material, predicted in section IV.4. The model has been implemented in Abaqus computational suite. The profile has been discretized using hexahedral brick C3D8T elements. Using this typology of elements, it is possible to account at the same time for thermal and mechanical behaviors.

The material mechanical properties have been calibrated, taking the DMA characterization of the resin system (section II.4) into account. The Jacobian matrix J (eq. (V.3)) has been coded using a UMAT subroutine. In each computational point, the UMAT routine reads the data of temperature and degree of cure previously computed, imported by UEXTERNALDB and URDFIL subroutines, to compute the elements of the Jacobian matrix.

In the sake of reducing the computational effort, just one quarter of the profile has been modeled, using the necessary symmetry conditions (Fig. V.5)).

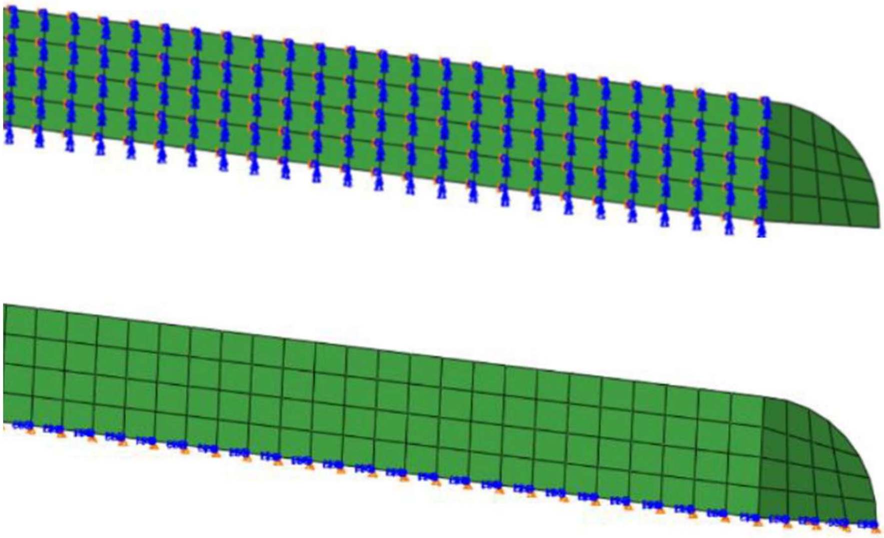

Figure V.5 *Symmetry boundary conditions.*

In order to achieve a stable system, all the displacements and rotations have been constrained on the nodes of the initial section of the profile (fig. V.6).

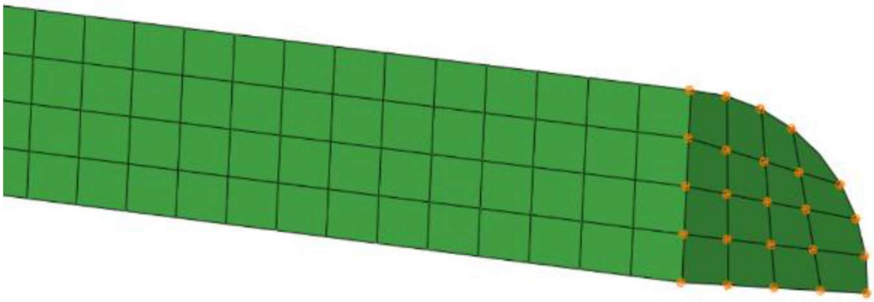

Figure V.6 *Mechanical constraint at the initial cross-section of the profile.*

The implemented constraints do not allow the profile to advance. Therefore, the viscous and the friction interactions between the die and the profile have been coded using UTRACLOAD user subroutine, in which the Eq. (V.15) is implemented. The rheology behavior of the resin has been characterized in section II.3. The thermal expansion and the chemical shrinkage are coded in a UEXPAN user subroutine.

The cavity wall has been modeled as an analytical rigid surface. Since in the present model the domain does not advance the interaction between the profile and the analytical rigid surface acts only in transversal direction. A hard contact (non-penetration) interaction was implemented between the profile surface and the cavity wall. The pulling force has been modelled as a load distributed on the extreme surface of the profile. The load of 1.77E+6 N m^{-2} was assumed taking into account the experimentally measured load total Q at pulling speed of 100 mm/min.

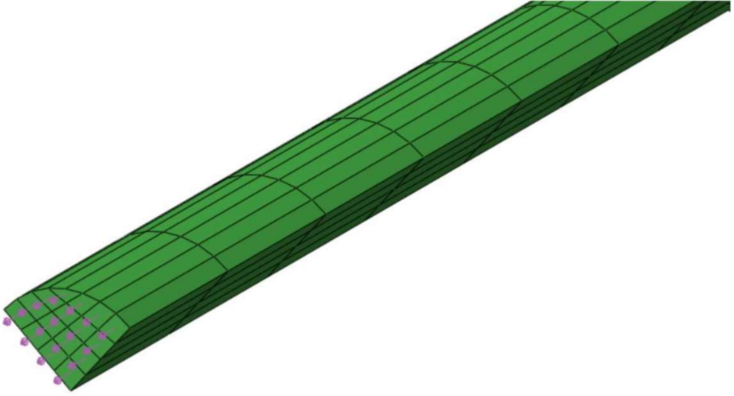

Figure V.7 *Pulling distributed load at the final cross-section.*

V.5 Experimental results

V.5.1 Experimental analysis of the pulling force

Fig V.8 shows the data collected during the pulling force measurements.

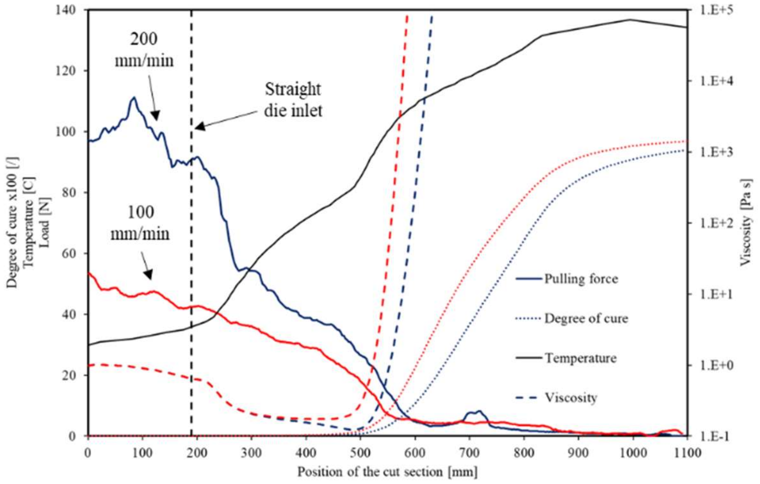

Figure V.8 *Measured pulling force compared to the thermochemical and rheological evolutions.*

The measured or computed data have been plotted against the position of the cut section along the chamber and die cavity. Blue lines refer to the process performed at 200 mm/min, while the red lines are relative to the process performed at 100 mm/min. The black dashed line separates the tapered injection chamber (the earliest 190 mm) from the straight die (last 900 mm). The solid thick lines are the resistant forces acquired by the load cell, the dashed lines represent the viscosity evolution and the pointed curves are the degree of cure profiles in the two cases. The differences in temperature result negligible.

Reinforcing fibers enter in the system at room temperature. Along the injection chamber, it can be noticed a slight thermal gradient. Indeed, upstream the cooling system, located at a distance of 240 mm from the chamber inlet, the heat flow is absorbed and dissipated by the cooling system. Downstream the cooling system, the material temperature increases due to the heating plates. At a distance of about 700 mm, the material temperature overcomes the temperature of heating plates. This phenomenon is due to the exothermal nature of cure reaction: the thermal energy produced by the resin is proportional to the cure rate (Tucci *et al.*, 2017). The polymerization of thermosetting resin is an irreversible reaction; therefore, the cure profile is always increasing.

The degree of cure is null in the injection chamber and in the first 300 mm of the straight die. At about 500 mm from the chamber inlet, the cure reaction is activated and the degree of cure starts increasing. The reaction is initially very fast and exhibit high cure rate. When the degree of cure approaches to the unit value, the cure gradient gradually decreases, until it reaches a *plateau*. Both the curves show the activation of the curing process approximately at the same position. After activation, the cure in the higher speed case (blue line) presents a delay, if compared to the lower speed case (red line). At the die outlet, the degree of cure is 97% in the slow case and 94% in the fast case. The dissimilarities between the two reactions are due to the different thermal cycles imposed to the resin. Indeed, in the fast case, the crossing time is the half of the short case. On the other hand, the faster the heating cycle is, the sharper the cure reaction is (Hardis *et al.*, 2013). Therefore, the cure rate in the fast case is remarkably higher than the one in the slow case.

The resin viscosity has a variation of several order of magnitude during the process. Therefore, in order to appreciate the rheological evolution of the resin, the viscosity curves are plotted on logarithm axis. Viscosity depends on cure and temperature, as described in section II.3. Unreacted resin at room temperature exhibits a viscosity of about 1 Pa s. Upstream the resin activation, only the temperature effects influence the resin. In the earliest 240 mm, the viscosity slightly decreases. Once overcome the cooling system the resin viscosity shows a marked decrease, up to about 0.1 Pa s.

At the cure activation, viscosity curves reach their minimum. During polymerization the liquid resin turn to the gel state and then to a glassy state.

These transformations imply a sharp rise in viscosity. The two viscosity curves, as well as the degree of cure curves, are not overlapping: in the fast case, the viscosity curve is delayed with respect to the slow case of about 30 mm. Moreover, in the fast case, viscosity reaches a lower value, due to the delay in cure reaction and to the effect of the thermal ramp velocity (Liang and Chandrashekhara, 2006).

To analyze the resistant load curves it should be noticed that higher decrease in the cumulative load curve means higher local load at that coordinate, accordingly to Eq. (V.21). The resistant load curves are expected to decrease along the entire die, since the contact area between the advancing material and the cavity wall decrease as the cut section advances. The resistant load arising within the die can be considered as the sum of three contributes: the bulk compaction force, the viscous drag and the solid friction (A.A. Safonov, Carlone and Akhatov, 2018). The bulk compaction force related to the compaction of the fibrous reinforcement within the die cavity. The viscous drag arises before gel transition whereas the resin presents a viscous liquid behavior. The solid friction is related to the contact between the wall and the advancing material after resin glass transition.

In the load curves depicted in Fig. V.8 the bulk compaction can be appreciated in the injection chamber zone, where the load is slightly decreasing. The tapered cavity transversally compress the advancing reinforcement. When the cut section crosses the first 100 mm of the injection chamber the width of the cavity, the reinforcement presents a low compaction. Due to this aspect and to the presence of the cut end, the fibers are free to move; therefore, the evaluation of the interaction between the wet fibers and the chamber cavity produces, in this short section, non-reliable measures. It can be appreciated that in the straight cavity, where the material is strongly constrained, the load curves do not present noise and unphysical oscillations.

In the injection chamber, the presence of the liquid resin implies also the action of viscous drag. At this stage, beside the low variation in viscosity, other factors, namely the geometrical narrowing of the cavity and the high mobility of the fiber reinforcement, influence the viscous resistance. The viscous drag can be observed between the straight cavity inlet and the activation of the cure reaction. At a distance of 240 mm from the chamber inlet, temperature sharply increase and viscosity remarkably drops. Due to this drop, the viscous drag gradually decreases. At the cure activation, the resin viscosity and the viscous drag sharply increases: a drop in the resistant load can be appreciated between 450 and 600 mm from the injection chamber inlet.

The glass transition is detected by the change in the slope of the load curves. In the last 500 mm of the die, the cumulate resistant load linearly decreases. In this final zone, the contact between advancing material and die has a solid frictional nature. It is worth to notice that in the fast case, the slope of the cumulative load curve in the “viscous zone” is twice higher than the slope in the slow case. Indeed, accordingly to Eq. (V.21), the slope is equal to the local interaction between the advancing material and the cavity wall. The viscous interaction linearly depends on the velocity, and, in the fast case, the pulling speed is exactly the double of the slow case one. The delay in cure activation implies a delay in the gel and glass transitions. Therefore, in the fast case, the load curve drop due to these transitions occurs about 30 mm downstream the slow case drop. Frictional resistance is almost negligible if compared to the viscous drag and the bulk compaction. This is mainly due to the chemical shrinkage of the resin, which decreases the contact pressure between the solid profile and the cavity wall.

V.5.2 Experimental evaluation of the strain field

The strain evolution of the advancing material during pultrusion has been evaluated using FBG optical sensors. The wavelengths from each sensor were acquired by the interrogator and transferred to a computer. Each of the measure was referred to its acquisition instant of time. Taking into account the position and the dimension of each FBG along the optical fiber and the advancing speed, the signals acquired were referred to the position along the heating die. In particular, since the sensitive segment has a length of 30 mm the signals acquired were referred to the middle point of the FBG. The length of the sensors, of course, affect also the measure, which is not punctual.

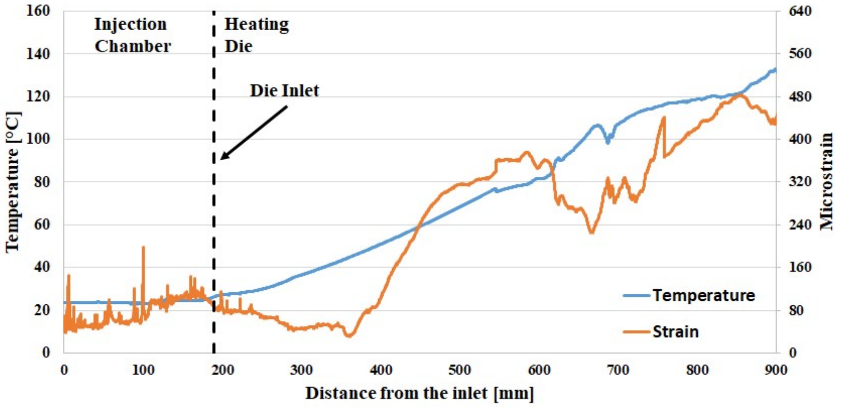

Figure V.9 *Strain and temperature profiles evaluated by FBGs.*

Fig. V.9 reports the temperature and the strain profiles evaluated using the signals provided by the FBG sensors. Temperature within the injection chamber presents a slight increase from the environmental temperature. Indeed, the heating load imposed on the die wall is thwarted by the refrigerating effect provided by the cooling system. The strain curve relative to the injection chamber presents a disturbed signal. This behavior is due to the wider free space available in which the FBG can oscillate. Whereas the tapered cavity converges to the final shape, the compressed advancing material does not allow the optical fiber to move and therefore the noise in the strain signal reduces. After the entrance in the die, temperature of the material increases, due to the thermal load imposed by the heating plates. Strain profile presents an initial decrease, until the distance of 360 mm from the chamber inlet, due to the decrease of viscosity related to the thermal increase described in section II.3. Afterward, along the successive 150 mm, the strain curve presents a sharp increase. In this zone, the activation of the cure reaction provokes the gelation of the resin and, as a consequence, a sharp increase in viscous resistance. At about 580 mm of distance from the die entrance, the strain profile relaxes for an interval of about 100 mm, in which it has a decrease related to the chemical shrinkage of the resin. Finally, the strain level keep growing until the polymerization occurs.

V.6 Numerical results

The mechanical model implemented, in order to predict the stress-strain fields, evaluate the material distortions during pultrusion process. In Figs. V.10 and V.11 the displacements in the two transversal directions are magnified, to evidence the material distortions along the die.

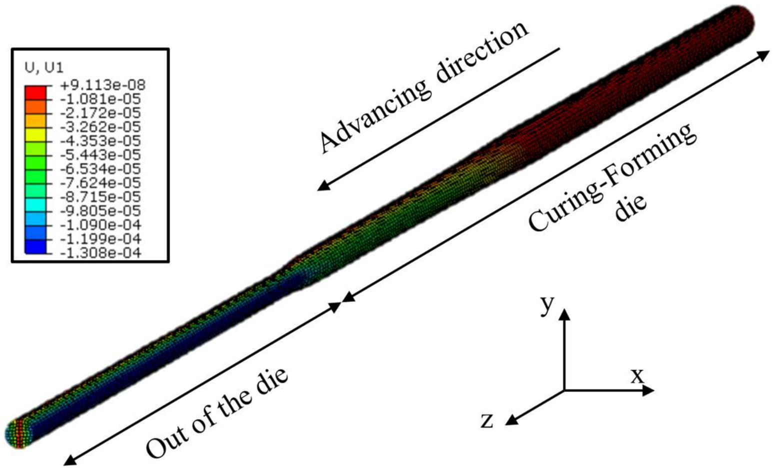

Figure V.10 *Nodal displacements in x direction.*

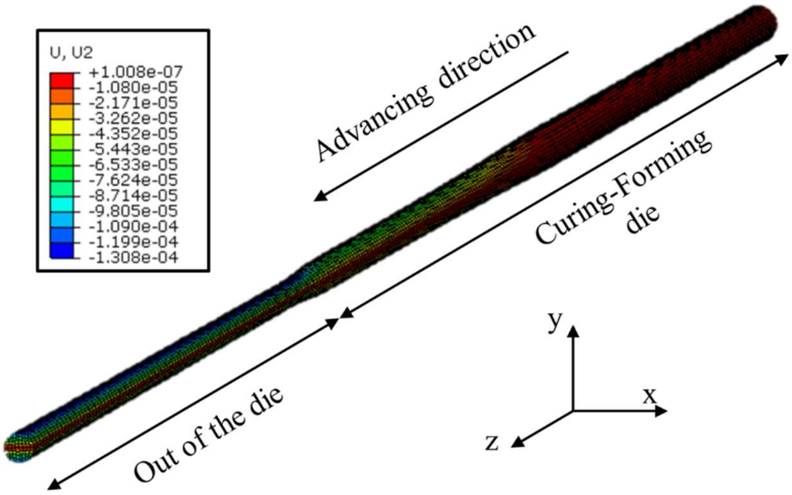

Figure V.11 *Nodal displacements in y direction.*

The results have been computed on a reduced profile representing one quarter of the profile, as described in section V.3. Nevertheless, for the sake of the clarity, the displacement results have been depicted on the entire profile using mirroring functions.

In the depicted contour plots, three zones, characterized by different behaviors, can be noted. Within the die, in the earliest zone, the advancing material shows null displacements in both the directions. The profile presents the same diameter of the cavity. In this zone, the cure reaction is not activated, and the thermal expansion of the material is constrained by the cavity walls. The second zone goes from the resin cure activation to the die outlet. Along this second region, the resin volume reduces due to the chemical shrinkage. In the last zone, downstream the die outlet, the profile experience a sharp thermal contraction, due to the fast cooling from the die temperature to the room temperature. It is worth to note that the displacements in the two transversal directions are not symmetric. Indeed, since the thermal loads act on the top and bottom surfaces (section IV.3), the cure reaction is first activated at the top point of the cross-section. Even if the cross-section implemented in the present model is quite narrow, the slight differences in thermal conditions provoke asymmetries in chemical evolutions and in the cross-section distortions.

Fig. V.12 depicts the distributions of the numerically computed stress components arising during the process along the curing-forming die. More specifically, the solid curves represent the internal stress computed at the barycenter point of the pultruding cross. Resin viscosity is included in the plot (black line) in the interest of completeness.

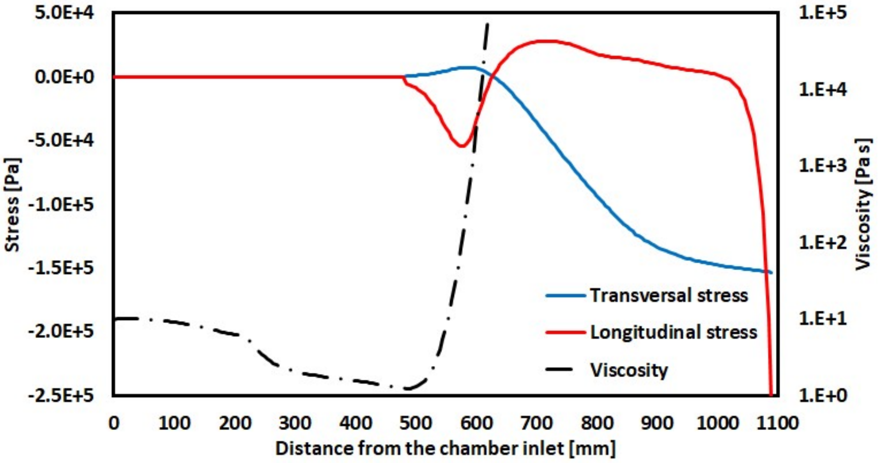

Figure V.12 *Stress profiles in transversal and longitudinal directions.*

Along the earliest 450 mm, the cure reaction is not activated and the resin behaves as a liquid. The resin viscosity decreases accordingly to the increase of temperature: In the first 190 mm, its value is close to the room temperature viscosity, since the presence of the refrigerant channels, located at 240 mm from the chamber inlet, thwarts the increase of temperature. Downstream the refrigerant channels, viscosity curve gradient sharply decreases. At 450 mm from the inlet, thermal energy absorbed by the resin along its path induces cure reaction, which produces a sharp increase of the viscosity. Downstream the reaction point, resin does not behave as a viscous medium anymore and it starts to cumulate process-induced stress. The transition from liquid to solid pass through a gel phase, located in a region of the cavity usually called gel zone. In the gel zone, the higher viscosity generates higher compression stress related to viscous drag. This behavior is visible in the longitudinal stress curve between 450 and 600 mm of distance from the inlet. Afterward, the interaction between advancing material and die walls has a solid frictional nature. This interaction depends on the contact pressure between the composite external surface and the die. The high temperature provokes the expansion of the advancing material and therefore a transversal stress, since it is constrained by the die. On the other hand, downstream the onset of the cure reaction, the resin shrinkage thwarts the thermal expansion. The sum of these two aspects determines the process induced transversal stress. In this regard, thermal effect prevails between 450 and 550 mm of distance from the inlet, where a slight increase of transversal stress is visible. Downstream, this position, the chemical shrinkage effect overcomes the thermal one and the material is compressed. This phenomenon produces the decrease of the transversal strain visible in the plot. Approaching to the outlet, the sharp variation from the die temperature to the room one provokes a thermal shock, which give place to local axial compression of the processed material.

The pulling force can be assessed by observing the reaction forces arising at the interface between the rigid surface of the cavity wall and the profile external surface. The local reaction forces is depicted in Fig. V.15 as a function of the distance from the injection chamber inlet.

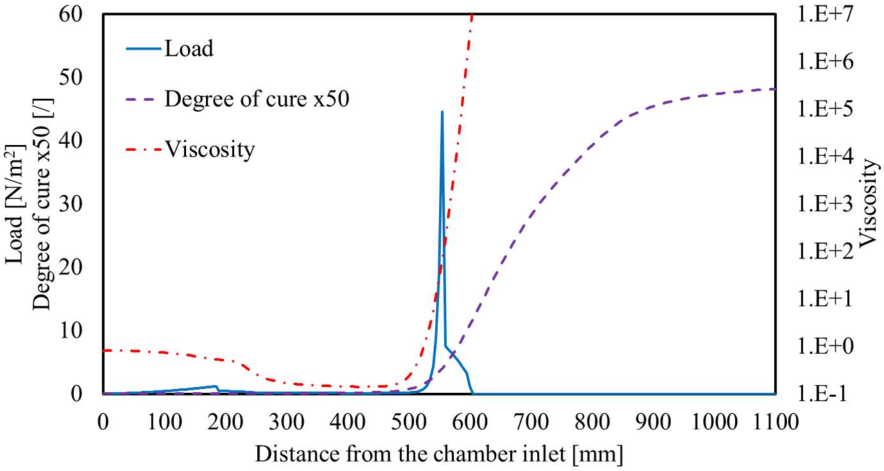

Figure V.13 *Profile of the resistance to the pulling force along the die.*

Along the initial 190 mm, the material is passing through the tapered injection chamber. The normal reaction arising due to the contact with the inclined walls produces a resistant force in pulling direction. The pressure increase described in chapter 3 produces an increase in the normal contact and, therefore, an increase in the resistant force. At the entrance in the straight die, the viscosity remarkably decreases due to the high temperature. In this phase, the viscous drag results negligible. At the cure reaction activation, the viscosity sharply increases. This behavior produces a peak in viscous drag, which give place to a peak of 50 N/m^2 in the resistant force. The resin between 500 mm and 600 mm of distance from the chamber inlet switch from a liquid state to a solid state. The frictional resistance to the pull results negligible if compared to the viscous drag peak.

Viscous drag results the most influencing behavior according to both the experimental measurements and numerical outcomes. In particular, using the described operative parameters, the peak arising during the cure reaction determines the 81% of the resistant load. It means that, the faster the cure reaction is, the lowest the viscous drag results. The viscous drag arising between the end of the tapered chamber (190 mm) and the onset of the peak (500 mm) represents the 7% of the total resistant load, while the frictional force is about the 0.4% of the total resistant load. Therefore, the earlier the reaction onset is located, the lower the necessary pulling force is, assuming a constant the force peak.

Conclusions

The present thesis provides a comprehensive approach to the numerical modeling of the injection pultrusion process. The models presented have been developed based on experimental evidence and literature outcomes, to investigate how the raw material properties and the processing conditions affect the quality of the final pultruded profile. The results and the discussion reported in this elaborate and in the scientific articles produced during these years represent, in the author's opinion, valid support to the study and the understanding of the process.

This study has been performed with the aim to move a further step toward the development and the implementation of an integrated model fully describing the injection pultrusion process. The next steps in this research field will face two main challenges: the complete linking of the different submodels to achieve a unique integrated model and the development of a tool supporting effectively the process design. In order to achieve these targets, the future research efforts should move toward the experimental validation of the numerical models, and, in parallel, should evolve the current numerical codes to achieve a low-computational-cost tool actively supporting the design and the production activities.

The main outcomes from this study follow:

- Resin characterization:
  The physical and mechanical properties of the resin systems employed in the flow, thermochemical and mechanical models have been assessed by experimental tests. The properties evolution have been modelled, to be included in the process simulations. The following remarks can be highlighted:
  - The cure kinetics of the orthophtalic polyester and of the EC114 epoxy have been modelled based on the experimental data collected by differential scanning calorimetry; the data shows that faster heating ramps determine higher peaks of cure rate, and, therefore, sharper reactions;
  - The models of the viscosity evolutions of the orthophtalic polyester and of the EC114 epoxy have been implemented using the data collected in rheology tests; the analysis of

    the data shows that the resin viscosity decreases at high temperature, until the cure reaction activation, which determines a sharp increase in viscous reaction of the resin; the decrease in viscosity is as marked as faster the heating ramp is;
  - The orthophtalic polyester system has been tested by dynamo-mechanic analysis to model its mechanical properties behavior at high temperature.
- Resin flow model:
  A multiphase model of the injection pultrusion process, with variable fluid viscosity and density, is presented and tested for validation against experimental data. The following remarks can be highlighted:
  - the implemented model is able to simulate the fluid flow through the reinforcing fibers in the injection chamber of an IP process;
  - numerical and experimental data indicate that higher pulling speed and injection pressure cause a significant increase in the fluid pressure in the injection chamber, affecting the amount of voids in the pultruded product. In particular, increasing the pulling speed of the 66% the maximum pressure computed results about 100% higher;
  - the reliability of the simulation results, with respect to pressure distribution and void content, is strongly dependent on the proper consideration of thermally induced properties variation: neglecting the thermal effects evolution leads to errors in prediction up to 120%.
- Thermochemical model:
  The study of the thermochemical evolution is the key aspect in pultrusion process analysis. In the present thesis, a numerical model simulating the heat exchange and the cure reaction in pultrusion has been implemented, leading to the following conclusions:
  - the exothermal nature of the cure reaction is evidenced by the experimental temperature profiles, which in all the cases, overcomes the platens temperature;
  - the higher pulling speed lead to a faster cure reaction and higher cure rate peak, compared to the slower case; nevertheless, in faster process, the final degree of cure of the resin results lower, due to the minor reaction time;
  - the pultrusion process can be improved in terms of reaction management and final degree of cure; the simulations performed using different platens temperatures demonstrate that a careful choice of the

    - process parameters lead to an higher degree of cure and to lower thermal shocks.
- Mechanical model:
  The stress-strain fields and the pulling force have been analyzed accounting for the thermochemical evolution of the resin and, therefore, for its variations in mechanical and physical properties. The discussion evidences the following conclusions:
    - The cure reaction drives the evolution of the stiffness moduli of the resin, as well as, its chemical contraction. At the same time, the thermal field implies the expansion of the advancing material. The combination of these behaviors determines the stress-strain of the material during pultrusion;
    - The heating temperatures and the pulling speed significantly affect the resistant loads;
    - Cure kinetic and viscosity evolution of the resin play a key role in the interaction between the advancing impregnated fibers and the cavity walls;
    - In the investigated process, the most of the resistance to the pulling force is related to the viscous drag, which results remarkably higher than the bulk compaction and the solid friction.

References

A grasshopper with fibre glass (2019). Available at: https://fiberline.com/grasshopper-fibre-glass (Accessed: August 28, 2019).

Aashia, R. *et al.* (2010) "Strain-temperature discrimination using a single fiber Bragg grating," *IEEE Photonics Technology Letters*, 22(11), pp. 778–780. doi: 10.1109/LPT.2010.2044657.

Akkerman, R. (2002) "On the properties of quasi-isotropic laminates," *Composites Part B:Engineering*, 33(2), pp. 133–140. doi: 10.1016/S1359-8368(02)00002-1.

Åstroöm, B. T. and Pipes, R. B. (1993) "A modeling approach to thermoplastic pultrusion. II: Verification of models," *Polymer Composites*, 14(3), pp. 184–194. doi: 10.1002/pc.750140303.

Bakis, C. E. *et al.* (2002) "Fibre Reinforced Polymer Composites for Construction - State-of-the-Art Review," *Journal of Composites for Construction*, 6(2), pp. 73–87. doi: 10.1061/(ASCE)1090-0268(2002)6:2(73).

Bank, L. C. (2006) *Composites for Construction*, *Composites for Construction*. doi: 10.1002/9780470121429.

Bank, L. C. (2007) *Composites for Construction: Structural Design with FRP Materials*, *Composites for Construction: Structural Design with FRP Materials*. doi: 10.1002/9780470121429.

Baran, I. *et al.* (2013) "Process induced residual stresses and distortions in pultrusion," *Composites Part B: Engineering*. Elsevier Ltd, 51, pp. 148–161. doi: 10.1016/j.compositesb.2013.03.031.

Baran, I. (2015) *Pultrusion : State-of-the-art Process Models*.

Baran, I. *et al.* (2018) "X-ray computed tomography characterization of manufacturing induced defects in a glass/polyester pultruded profile," *Composite Structures*, 195, pp. 74–82. doi: 10.1016/j.compstruct.2018.04.030.

Baran, Ismet, Akkerman, R. and Hattel, J. H. (2014) "Material characterization of a polyester resin system for the pultrusion process," *Composites Part B: Engineering*. Elsevier Ltd, 64, pp. 194–201. doi: 10.1016/j.compositesb.2014.04.030.

Baran, I, Akkerman, R. and Hattel, J. H. (2014) "Modelling the pultrusion process of an industrial L-shaped composite profile," *Composite Structures*. Elsevier Ltd, 118(1), pp. 37–48. doi: 10.1016/j.compstruct.2014.07.018.

Baran, I., Hattel, J. H. and Akkerman, R. (2015) "Investigation of process induced warpage for pultrusion of a rectangular hollow profile," *Composites Part B: Engineering*. Elsevier Ltd, 68, pp. 365–374. doi: 10.1016/j.compositesb.2014.07.032.

Baran, I., Hattel, J. H. and Tutum, C. C. (2013) "Thermo-chemical modelling strategies for the pultrusion process," *Applied Composite Materials*, 20(6), pp. 1247–1263. doi: 10.1007/s10443-013-9331-x.

Baran, I., Tutum, C. C. and Hattel, J. H. (2013) "The effect of thermal contact resistance on the thermosetting pultrusion process," *Composites Part B: Engineering*. Elsevier Ltd, 45(1), pp. 995–1000. doi: 10.1016/j.compositesb.2012.09.049.

Batch, G. L. and Macosko, C. W. (1987a) "A computer analysis of temperature and pressure distribution in a pultrusion die," in *Proceeding of the 42nd annual conference, society of the plastics industry. 2–6 February, 1987*.

Batch, G. L. and Macosko, C. W. (1987b) "Kinetics of crosslinking free radical polymerizationwith diffusion-limited propagation," in *Annual Technical Conference - Society of Plastics Engineers*, pp. 974–976.

Batch, G. L. and Macosko, C. W. (1990) "Analysis of pressure, pulling force, and sloughing in pultrusion," in *Fundamentals of Natural Convection; Seattle, WA, USA; 18 June 1990 through 20 June 1990.*

Belingardi, G. *et al.* (2017) *Lightweight solutions for vehicle frontal bumper: Crash design and manufacturing issues., Dynamic Response and Failure of Composite Materials and Structures*. doi: 10.1016/B978-0-08-100887-4.00012-3.

Bibbo, M. and Gutowski, T. G. (1986) "Analysis of the pulling force in pultrusion," in *Annual technical conference – society of plastics engineers*, p. 1430.

Bochmann, M. (2010) "The chemistry of catalyst activation: The case of group 4 polymerization catalysts," *Organometallics*, 29(21), pp. 4711–4740. doi: 10.1021/om1004447.

Bodaghi, M. *et al.* (2018) "A model for fibre washout during high injection pressure resin transfer moulding." doi: 10.1177/0731684418765968.

Bogetti, T. A. and Gillespie, J. W. (1992) "Process-Induced Stress and Deformation in Thick-Section Thermoset Composite Laminates," *Journal of Composite Materials*, 26(5), pp. 626–660. doi: 10.1177/002199839202600502.

Boisse, P. (2015) *Advances in composites manufacturing and process design*, *Advances in Composites Manufacturing and Process Design*. doi: 10.1016/C2014-0-02644-5.

Boller, A., Jin, Y. and Wunderlich, B. (1994) "Heat capacity measurement by modulated DSC at constant temperature," *Journal of Thermal Analysis*, 42(2–3), pp. 307–330. doi: 10.1007/BF02548519.

Boyd, S. W., Dulieu-Barton, J. M. and Rumsey, L. (2006) "Stress analysis of finger joints in pultruded GRP materials," *International Journal of Adhesion and Adhesives*, 26(7), pp. 498–510. doi: 10.1016/j.ijadhadh.2005.07.003.

Brown, M. E. (2004) *Introduction to Thermal Analysis. Techniques and Applications*, *Thermal Properties of Green Polymers*. Dordrecht: Kluwer Academic Publishers. Available at: http://ebooks.springerlink.com.

Bruni, G. *et al.* (2011) "Determination of the nateglinide polymorphic purity through DSC," *Journal of Pharmaceutical and Biomedical Analysis*. Elsevier B.V., 54(5), pp. 1196–1199. doi: 10.1016/j.jpba.2010.12.003.

Carlone, P. *et al.* (2013a) "Computational approaches for modeling the multiphysics in pultrusion process," *Advances in Mechanical Engineering*, 2013. doi: 10.1155/2013/301875.

Carlone, P. *et al.* (2013b) "Computational approaches for modeling the multiphysics in pultrusion process," *Advances in Mechanical Engineering*, 2013. doi: 10.1155/2013/301875.

Carlone, P., Palazzo, G. S. and Pasquino, R. (2006) "Pultrusion manufacturing process development by computational modelling and methods," *Mathematical and Computer Modelling*, 44(7–8), pp. 701–709. doi: 10.1016/j.mcm.2006.02.006.

Carman, P. C. (1997) "Fluid flow through granular beds," *Process Safety and Environmental Protection: Transactions of the Institution of Chemical Engineers, Part B*. Institution of Chemical Engineers, 75(Suppl), pp. S32–S48. doi: 10.1016/s0263-8762(97)80003-2.

CIRIA (2018) *Fibre-reinforced polymer bridges - Guidance for designers*.

Colombo, C. and Vergani, L. (2010) "Experimental and numerical analysis of a bus component in composite material," *Composite Structures*, 92(7), pp. 1706–1715. doi: 10.1016/j.compstruct.2009.12.012.

Correia, J. R. (2013) *Pultrusion of advanced fibre-reinforced polymer (FRP) composites*, *Advanced Fibre-Reinforced Polymer (FRP) Composites for Structural Applications*. doi: 10.1533/9780857098641.2.207.

Ding, Z. *et al.* (2000) "Numerical and experimental analysis of resin flow and cure in resin injection pultrusion (RIP)," *Polymer Composites*, 21(5), pp. 762–778. doi: 10.1002/pc.10231.

Drebushchak, V. A. (2004) "Calibration coefficient of a heat-flow DSC part 1. Relation to the sensitivity of a thermocouple," *Journal of Thermal Analysis and Calorimetry*, 76(3), pp. 941–947. doi: 10.1023/B:JTAN.0000032279.21790.f6.

Engineered for the automotive industry (2019). Available at: http://cqfd-composites.com/ultimate-mechanics (Accessed: August 28, 2019).

European Pultrusion Technology Association (2019) *An expanded role for pultruded composites in 5G cities*. Available at: https://pultruders.org/news-details.php?id=31 (Accessed: February 11, 2020).

Fairuz, A. M. *et al.* (2014) "Polymer composite manufacturing using a pultrusion process: A review," *American Journal of Applied Sciences*, 11(10), pp. 1798–1810. doi: 10.3844/ajassp.2014.1798.1810.

Fedulov, B. N. *et al.* (2016) “Strength Analysis and Process Simulation of Subway Contact Rail Support Bracket of Composite Materials,” *Applied Composite Materials*, 23(5), pp. 999–1013. doi: 10.1007/s10443-016-9495-2.

Ferreira, A. J. M. *et al.* (2001) “Modelling of concrete beams reinforced with FRP re-bars,” *Composite Structures*, 53(1), pp. 107–116. doi: 10.1016/S0263-8223(00)00182-3.

Flexible and durable pool bottom for Danish waterpark (2019). Available at: https://fiberline.com/other-structures/flexible-and-durable-pool-bottom-danish-waterpark (Accessed: August 28, 2019).

Frauendorfer, E., Wolf, A. and Hergeth, W. D. (2010) “Polymerization online monitoring,” *Chemical Engineering and Technology*, 33(11), pp. 1767–1778. doi: 10.1002/ceat.201000265.

Friedrich, J. (2011) “Mechanisms of plasma polymerization - Reviewed from a chemical point of view,” *Plasma Processes and Polymers*, 8(9), pp. 783–802. doi: 10.1002/ppap.201100038.

Gadam, S. U. K. *et al.* (2000) “The impact of pultrusion processing parameters on resin pressure rise inside a tapered cylindrical die for glass-fibre/epoxy composites,” *Composites Science and Technology*, 60(6), pp. 945–958. doi: 10.1016/S0266-3538(99)00181-5.

Gascón, L. *et al.* (2016) “A two-phase flow model to simulate mold filling and saturation in Resin Transfer Molding,” pp. 229–239. doi: 10.1007/s12289-015-1225-z.

Gebart, B. R. (1992) “Permeability of Unidirectional Reinforcements for RTM,” *Journal of Composite Materials*, 26(8), pp. 1100–1133. doi: 10.1177/002199839202600802.

Ghadimi, B., Russo, S. and Rosano, M. (2017) “Predicted mechanical performance of pultruded FRP material under severe temperature duress,” *Composite Structures*. Elsevier Ltd, 176, pp. 673–683. doi: 10.1016/j.compstruct.2017.05.061.

Goertzen, W. K. and Kessler, M. R. (2007) “Dynamic mechanical analysis of carbon/epoxy composites for structural pipeline repair,” *Composites Part B: Engineering*, 38(1), pp. 1–9. doi: 10.1016/j.compositesb.2006.06.002.

Goetschel, D. B. and Radford, D. W. (1997) “Analytical development of through-thickness properties of composite laminates,” *Journal of Advanced Materials*, 28(4), pp. 37–46.

Gorthala, R. *et al.* (1994) “Comparison of processing parameters for pultruded graphite/epoxy and fiberglass/epoxy: a heat transfer and curing model,” *Journal of Reinforced Plastics and Composites*, 13(4), pp. 288–300. doi: 10.1177/073168449401300401.

Gorthala, R., Roux, J. A. and Vaughan, J. G. (1994) “Resin Flow, Cure and Heat Transfer Analysis for Pultrusion Process,” *Journal of Composite Materials*, 28(6), pp. 486–506. doi: 10.1177/002199839402800601.

Gorthala, R, Roux, J. and Vaughan, J. (1994) “Resin flow, cure and heat transfer analysis for pultrusion process," *Journal of composite …*, 28(6), p. 486. doi: 10.1177/002199839402800601.

Green, A. K. and Shikhmanter, L. (1999) "Coupon development for fatigue testing of bonded assemblies of pultruded rods," *Composites Part A: Applied Science and Manufacturing*, 30(5), pp. 611–613. doi: 10.1016/S1359-835X(98)00180-8.

GRP bridge across UK M6 motorway (2019). Available at: https://fiberline.com/grp-bridge-across-uk-m6-motorway (Accessed: August 28, 2019).

Gutowski, T. G., Morigaki, T. and Cai, Z. (1987) "The Consolidation of Laminate Composites," *Journal of Composite Materials*, 21(2), pp. 172–188. doi: 10.1177/002199838702100207.

Hardesty, E. E. (2017) "ADVANCED COMPOSITES, THE ON-GOING TRANSITION FROM HANDMADE PROTOTYPES TO MACHINE-FABRICATED COMPONENTS."

Hardis, R. *et al.* (2013) "Cure kinetics characterization and monitoring of an epoxy resin using DSC, Raman spectroscopy, and DEA," *Composites Part A: Applied Science and Manufacturing*. Elsevier Ltd, 49, pp. 100–108. doi: 10.1016/j.compositesa.2013.01.021.

Höhne, G. W. H. and Schawe, J. E. K. (1993) "Dynamic behaviour of power compensated differential scanning calorimeters. Part 1. DSC as a linear system," *Thermochimica Acta*, 229(C), pp. 37–52. doi: 10.1016/0040-6031(93)80313-Y.

Jeswani, A. L. and Roux, J. A. (2006) "Numerical modelling of design parameters for manufacturing polyester/glass composites by resin injection pultrusion," *Polymers and Polymer Composites*, 14(7), pp. 651–669. doi: 10.1177/096739110601400701.

Jeswani, A. L. and Roux, J. A. (2007a) "Impact of processing parameters and tapering of injection chamber walls in resin injection pultrusion," *Polymers and Polymer Composites*, 15(7), pp. 507–519. doi: 10.1177/096739110701500701.

Jeswani, A. L. and Roux, J. A. (2007b) "Manufacturing modeling of three-dimensional resin injection pultrusion process control parameters for polyester/glass rovings composites," *Journal of Manufacturing Science and Engineering, Transactions of the ASME*, 129(1), pp. 143–156. doi: 10.1115/1.2383148.

Jeswani, A. L. and Roux, J. A. (2008) "Modeling of processing for slot and discrete port tapered resin injection pultrusion," *Journal of Thermophysics and Heat Transfer*, 22(4), pp. 749–757. doi: 10.2514/1.33209.

Johnston, A., Vaziri, R. and Poursartip, A. (2001) "A plane strain model for process-induced deformation of laminated composite structures," *Journal of Composite Materials*, 35(16), pp. 1435–1469. doi: 10.1106/YXEA-5MH9-76J5-BACK.

Kim, D.-H. *et al.* (1997) "A model for thermosetting composite pultrusion process," *J Compos Mater*, 31(20), pp. 2105–2122.

Lau, S. T. W., Said, M. R. and Yaakob, M. Y. (2012) "On the effect of geometrical designs and failure modes in composite axial crushing: A literature review," *Composite Structures*. Elsevier Ltd, 94(3), pp. 803–812. doi: 10.1016/j.compstruct.2011.09.013.

Lee, B. (2003) "Review of the present status of optical fiber sensors," *Optical Fiber Technology*, 9(2), pp. 57–79. doi: 10.1016/S1068-5200(02)00527-8.

Liang, G. and Chandrashekhara, K. (2006) "Cure kinetics and rheology characterization of soy-based epoxy resin system," *Journal of Applied Polymer Science*, 102(4), pp. 3168–3180. doi: 10.1002/app.24369.

Lin Liu, X., Crouch, I. G. and Lam, Y. C. (2000) "Simulation of heat transfer and cure in pultrusion with a general-purpose finite element package," *Composites Science and Technology*, 60(6), pp. 857–864. doi: 10.1016/S0266-3538(99)00189-X.

Liu, X. L. (2003) "A finite element/nodal volume technique for flow simulation of injection pultrusion," *Composites Part A: Applied Science and Manufacturing*, 34(7), pp. 649–661. doi: 10.1016/S1359-835X(03)00085-X.

Mahroug, M. E. M., Ashour, A. F. and Lam, D. (2014) "Experimental response and code modelling of continuous concrete slabs reinforced with BFRP bars," *Composite Structures*. Elsevier Ltd, 107, pp. 664–674. doi: 10.1016/j.compstruct.2013.08.029.

Mao, X. *et al.* (2009) "Rheological characterization of a gelcasting system based on epoxy resin," *Ceramics International*, 35(1), pp. 415–420. doi: 10.1016/j.ceramint.2007.12.005.

Marin, E. *et al.* (2012) "Liquid Resin Infusion process monitoring with superimposed Fibre Bragg Grating sensor," *Polymer Testing*. Elsevier Ltd, 31(8), pp. 1045–1052. doi: 10.1016/j.polymertesting.2012.07.018.

Marley 400 - 800MD - Unilite (2019). Available at: https://spxcooling.com/products/detail/counterflow-field-erected-cooling-tower (Accessed: August 28, 2019).

Masuram, N. B., Roux, J. A. and Jeswani, A. L. (2016) "Fiber Volume Fraction Influence on Fiber Compaction in Tapered Resin Injection Pultrusion Manufacturing," pp. 421–442. doi: 10.1007/s10443-015-9466-z.

Masuram, N. B., Roux, J. A. and Jeswani, A. L. (2017) "Resin viscosity influence on fiber compaction in tapered resin injection pultrusion manufacturing," *Applied Composite Materials*. Applied Composite Materials, 25(3), pp. 485–506. doi: 10.1007/s10443-017-9631-7.

Menard, K. (2006) *Dynamic Mechanical Analysis-A pratical introduction.*, *CRC Press- Taylor and Francis Group*. CRC Press- Taylor and Francis Group.

Menczel, J. and Prime, B. (2009) *Thermal analysis of polymers - Fundamentals and Applications*. Hoboken, New Jersey: Jhon Wiley & Sons, Inc.

Meyer, R. W. (1985) “FRP Raw Materials,” in *Handbook of Pultrusion Technology*.

Monti, M. *et al.* (2011) “Effect of carbon nanofibers on the cure kinetics of unsaturated polyester resin: Thermal and chemorheological modelling,” *Composites Science and Technology*. Elsevier Ltd, 71(12), pp. 1507–1516. doi: 10.1016/j.compscitech.2011.06.010.

Mraw, S. C. (1982) “Mathematical treatment of heat flow in differential scanning calorimetry and differential thermal analysis instruments,” *Review of Scientific Instruments*, 53(2), pp. 228–231. doi: 10.1063/1.1136933.

Nawab, Y. *et al.* (2013) “Chemical shrinkage characterization techniques for thermoset resins and associated composites,” *Journal of Materials Science*, 48(16), pp. 5387–5409. doi: 10.1007/s10853-013-7333-6.

Olivier, P. A. (2006) “A note upon the development of residual curing strains in carbon/epoxy laminates. Study by thermomechanical analysis,” *Composites Part A: Applied Science and Manufacturing*, 37(4), pp. 602–616. doi: 10.1016/j.compositesa.2005.05.006.

Palikhel, D. R., Roux, J. A. and Jeswani, A. L. (2013) “Die-Attached Versus Die-Detached Resin Injection Chamber for Pultrusion,” pp. 55–72. doi: 10.1007/s10443-012-9251-1.

Papon, A. *et al.* (2012) “Glass-transition temperature gradient in nanocomposites: Evidence from nuclear magnetic resonance and differential scanning calorimetry,” *Physical Review Letters*, 108(6), pp. 1–5. doi: 10.1103/PhysRevLett.108.065702.

Park, J. Y. and Zureick, A.-H. (2005) “Effect of filler and void content on mechanical properties of pultruded composite materials under shear loading,” *Polymer Composites*, 26(2), pp. 181–192. doi: 10.1002/pc.20079.

Park, S.-J. (2018) *Carbon Fibers*. doi: 10.1007/978-981-13-0538-2.

Paulsen, U. S. *et al.* (2013) “Design optimization of a 5 MW floating offshore vertical-axis wind turbine,” in *Energy Procedia*, pp. 22–32. doi: 10.1016/j.egypro.2013.07.155.

Paulsen, U. S. *et al.* (2014) “The 5 MW DeepWind floating offshore vertical wind turbine concept design - Status and perspective,” in *European Wind Energy Association Conference and Exhibition 2014, EWEA 2014*.

Performance 700 Times Better Than Aluminum (2019). Available at: https://www.deceuninckna.com/windows-and-doors/innergy/feature-and-benefits (Accessed: August 28, 2019).

Price, H. L. and Cupschalk, S. G. (1984) “Pulling Force and Its Variation in Composite Materials Pultrusion,” *Advances in Chemistry Series*, pp. 301–322. doi: 10.1021/ba-1984-0206.ch018.

Rahatekar, S. S. and Roux, J. A. (2003) “Numerical Simulation of Pressure Variation and Resin Flow in Injection Pultrusion,” 37(12). doi: 10.1177/002199803033454.

Ranga, B. K. *et al.* (2011) “Effect of injection chamber length and pull speed of tapered resin injection pultrusion,” *Journal of Reinforced Plastics and*

Composites, 30(16), pp. 1373–1387. doi: 10.1177/0731684411422415.

Ranjit, S., Roux, J. A. and Jeswani, A. L. (2013) "Impact of Injection Slot Width and Final Composite Thickness for Attached-Die and Detached-Die Tapered Resin Injection Pultrusion," pp. 431–448. doi: 10.1007/s10443-012-9280-9.

Saboohi, S. *et al.* (2019) "The Physics of Plasma Ion Chemistry: A Case Study of Plasma Polymerization of Ethyl Acetate," *Journal of Physical Chemistry Letters*. American Chemical Society, 10, pp. 7306–7310. doi: 10.1021/acs.jpclett.9b02855.

Saenz-Dominguez, I. *et al.* (2019) "Design and characterisation of cellular composite structures for automotive crash-boxes manufactured by out of die ultraviolet cured pultrusion," *Composites Part B: Engineering*. Elsevier, 160(September 2018), pp. 217–224. doi: 10.1016/j.compositesb.2018.10.046.

Safonov, A.A., Carlone, P. and Akhatov, I. (2018) "Mathematical simulation of pultrusion processes: A review," *Composite Structures*, 184. doi: 10.1016/j.compstruct.2017.09.093.

Safonov, Alexander A., Carlone, P. and Akhatov, I. (2018) "Mathematical simulation of pultrusion processes: A review," *Composite Structures*, 184(July 2017), pp. 153–177. doi: 10.1016/j.compstruct.2017.09.093.

Safonov, A. A. and Konstantinov, A. Y. (2015) "Numerical evaluation of residual manufacturing deformations in complex pultruded composite profiles," *ICCM International Conferences on Composite Materials*, 2015-July(July), pp. 19–24.

Sakr, M., El Naggar, M. H. and Nehdi, M. (2005) "Interface Characteristics and Laboratory Constructability Tests of Novel Fiber-Reinforced Polymer/Concrete Piles," *Journal of Composites for Construction*, 9(3), pp. 274–283. doi: 10.1061/(ASCE)1090-0268(2005)9:3(274).

Schick, C. (2009) "Differential scanning calorimetry (DSC) of semicrystalline polymers," *Analytical and Bioanalytical Chemistry*, 395(6), pp. 1589–1611. doi: 10.1007/s00216-009-3169-y.

Šesták, J. and Berggren, G. (1971) "Study of the kinetics of the mechanism of solid-state reactions at increasing temperatures," *Thermochimica Acta*, 3(1), pp. 1–12. doi: 10.1016/0040-6031(71)85051-7.

Shakya, N., Roux, J. A. and Jeswani, A. L. (2013) "Effect of resin viscosity in fiber reinforcement compaction in resin injection pultrusion process," *Applied Composite Materials*, 20(6), pp. 1173–1193. doi: 10.1007/s10443-013-9320-0.

Shanku, R., Vaughan, J. G. and Roux, J. A. (1997) "Rheological Characteristics and Cure Kinetics of EPON 862 / W Epoxy Used in Pultrusion MEASUREMENTS," 16(4), pp. 297–311.

Sharma, D. *et al.* (1998) "Investigation of Dynamic Pressure Behavior in a Pultrusion Die," *Journal of Composite Materials*, 32(10), pp. 929–950. doi: 10.1177/002199839803201002.

Shaw-Stewart, D. and Sumerak, J. E. (2000) “The pultrusion process,” in *Pultrusion for Engineers*. doi: 10.1533/9781855738881.19.

Sourour, S. and Kamal, M. R. (1976) “Differential scanning calorimetry of epoxy cure: isothermal cure kinetics,” *Thermochimica Acta*, 14(1–2), pp. 41–59. doi: 10.1016/0040-6031(76)80056-1.

Spangenberg, J. *et al.* (2017) “The effect of saturation on resin flow in injection pultrusion: A preliminary numerical study,” in *ICCM International Conferences on Composite Materials*.

Starr, T. F. (2000) *Pultrusion for engineers*, *Woodhead Publishing Limited*. Abington Hall, Abington Cambridge CB1 6AH, England. doi: 10.1533/9781855738881.97.

Strauß, S., Senz, A. and Ellinger, J. (2019) “Comparison of the Processing of Epoxy Resins in Pultrusion with Open Bath Impregnation and Closed-Injection Pultrusion,” *Journal of Composites Science*, 3(3), p. 87. doi: 10.3390/jcs3030087.

Tonatto, M. L. P. *et al.* (2016) “Progressive damage modeling of spiral and ring composite structures for offloading hoses,” *Materials and Design*, 108(August), pp. 374–382. doi: 10.1016/j.matdes.2016.06.124.

Tsai, S. and Hahn, T. (2000) *Introduction to Composite Materials Science*, *The Journal of Adhesion*. doi: 10.1080/00218460008029292.

Tucci, F. *et al.* (2017) “Modelling and simulation of cure in pultrusion processes,” in *AIP Conference Proceedings*. doi: 10.1063/1.5008078.

Tucci, F. *et al.* (2019) “Integrated modeling of injection pultrusion,” *AIP Conference Proceedings*, 2113. doi: 10.1063/1.5112601.

Tucci, F. *et al.* (2020) “Multiphase flow simulation in injection pultrusion with variable properties,” *Materials and Manufacturing Processes*. Taylor & Francis, 00(00), pp. 1–11. doi: 10.1080/10426914.2020.1711928.

Turvey, G. J. (2016) “CFRP stiffened GFRP continuous beams – A simple closed-form analysis and its experimental verification for serviceability limit deformations,” *Composite Structures*. Elsevier Ltd, 153, pp. 952–960. doi: 10.1016/j.compstruct.2016.06.011.

Verhaeghe, J. (2001) “Composite trailer: From prototype to industrialisation,” in *International SAMPE Symposium and Exhibition (Proceedings)*, pp. 1612–1620.

Voorakaranam, S., Joseph, B. and Kardos, J. L. (1999) “Modelling and Control of an Injection Pultrusion Process,” *J. Compos. Mater.*, 33, pp. 1173–1204. doi: 10.1177/002199839903301302.

Vyazovkin, S. *et al.* (2011) “Thermochimica Acta ICTAC Kinetics Committee recommendations for performing kinetic computations on thermal analysis data,” *Thermochimica Acta*. Elsevier B.V., 520(1–2), pp. 1–19. doi: 10.1016/j.tca.2011.03.034.

Witten, E. and Mathes, V. (2019) *The Market for Glass Fibre Reinforced Plastics (GRP) in 2019*. Available at: https://www.avk-tv.de/files/20190911_avk_market_report_e_2019_final.pdf.

Wu, C. S. *et al.* (2002) “Thermal stability of epoxy resins containing flame retardant components: An evaluation with thermogravimetric analysis,” *Polymer Degradation and Stability*, 78(1), pp. 41–48. doi: 10.1016/S0141-3910(02)00117-9.

Yousefi, A., Lafleur, P. G. and Gauvin, R. (1997) “Kinetic studies of thermoset cure reactions: A review,” *Polymer Composites*, 18(2), pp. 157–168. doi: 10.1002/pc.10270.

Yuksel, O. *et al.* (2019) “Investigation of transverse residual stresses in a thick pultruded composite using digital image correlation with hole drilling,” *Composite Structures*. Elsevier Ltd, 223. doi: 10.1016/j.compstruct.2019.110954.

Zanqui, A. B. *et al.* (2015) “Subcritical extraction of flaxseed oil with n-propane: Composition and purity,” *Food Chemistry*. Elsevier Ltd, 188, pp. 452–458. doi: 10.1016/j.foodchem.2015.05.033.

Zhang, D. *et al.* (2014) “Flexural properties of a lightweight hybrid FRP-aluminum modular space truss bridge system,” *Composite Structures*, 108(1). doi: 10.1016/j.compstruct.2013.09.058.

Zyka, K. and Mohajerani, A. (2016) “Composite piles: A review,” *Construction and Building Materials*, 107, pp. 394–410. doi: 10.1016/j.conbuildmat.2016.01.013.

Table of the symbols

t	Time
T	Temperature
α	Degree of cure
x	Length coordinate
f	Referring to the fibers (as a subscript)
m	Referring to the fibers (as a subscript)
L	Referring to the longitudinal direction (as a subscript)
T	Referring to the transversal direction (as a subscript)
E	Stiffness modulus
G	Shear modulus
ν	Poisson ratio
V	Volume fraction
C	Bulk modulus
IP	Referring to the in-plane direction (as a subscript)
OP	Referring to the out-of-plane direction (as a subscript)
A_e	Characteristic parameters of the CHILE model
B_e	Characteristic parameters of the CHILE model
T_C	Critical temperature
T_g	Glass transition temperature
T^*	Difference between T_g and the actual temperature
${T_g}^0$	Glass transition temperature of the fully uncured resin
α_{Tg}	Variation coefficient of the glass transition temperature
A_0	Frequency factor of the resin kinetic
E_a	Activation energy of the resin kinetic
m	Resin kinetic parameter
n	Resin kinetic parameter
H	Heat generated during cure
Q	Generated heat flow
η	Resin viscosity
A_η	Characteristic parameters of the reaction
B_η	Characteristic parameters of the reaction
C_η	Characteristic parameters of the reaction

D_η	Characteristic parameters of the reaction
E'	Storage modulus
E''	Loss modulus
δ	Phase delay
ρ	Density
v	Fluid velocity
φ	Porosity
V	Fiber velocity
K	Permeability
P	Pressure
D	Velocity contribution given by the viscous drag
CTE	Coefficient of thermal expansion
R_f	Fiber radius
k'	Empirical permeability parameter
$V_a{}'$	Empirical permeability parameter
c	Gebart calibration parameter
C_1	Gebart calibration parameter
L	Length of the cavity
θ	Taper angle
h_0	Height of the straight cavity
γ	Inclination angle in the tapered injection chamber
c_p	Specific heat
k	Thermal conductivity
q	Exothermal heat generation rate
d	Referring to the die (as a subscript)
H_T	Total heat generated
R_m	Rate of cure
$\dot{\sigma}$	Stress increment
$\dot{\varepsilon}$	Strain increment
J	Jacobian matrix
th	Referring to the thermal behavior (as a subscript)
ch	Referring to the chemical behavior (as a subscript)
ΔV_{sh}	Volume shrinkage
F_{pull}	Pulling force
F_{coll}	Collimation force
F_{vis}	Viscous drag
F_{fric}	Friction force
λ_{th}	Fluid layer thickness
μ	Friction coefficient
Q_{force}	Cumulate resistance to the pulling force
x_c	Cut section position

x_{out}	Die outlet
t_c	Fiber cutting instant
λ	Wavelength
λ_0	Reference wavelength
C_T	FBG calibration constant coefficient
C_ε	FBG calibration constant coefficient
a_ε	FBG calibration constant coefficient
b_ε	FBG calibration constant coefficient